



HAL
open science

Electronic structure and transport in the graphene/MoS heterostructure for the conception of a field effect transistor

Daniela Di Felice

► **To cite this version:**

Daniela Di Felice. Electronic structure and transport in the graphene/MoS heterostructure for the conception of a field effect transistor. Materials Science [cond-mat.mtrl-sci]. Université Paris Saclay (COmUE), 2018. English. NNT: 2018SACLS267 . tel-01898306

HAL Id: tel-01898306

<https://theses.hal.science/tel-01898306>

Submitted on 18 Oct 2018

HAL is a multi-disciplinary open access archive for the deposit and dissemination of scientific research documents, whether they are published or not. The documents may come from teaching and research institutions in France or abroad, or from public or private research centers.

L'archive ouverte pluridisciplinaire **HAL**, est destinée au dépôt et à la diffusion de documents scientifiques de niveau recherche, publiés ou non, émanant des établissements d'enseignement et de recherche français ou étrangers, des laboratoires publics ou privés.

Electronic structure and transport in the graphene/MoS₂ heterostructure for the conception of a field effect transistor

Thèse de doctorat de l'Université Paris-Saclay
préparée à l'Université Paris-Sud

École doctorale n° 572: Ondes et Matière (EDOM)
Spécialité de doctorat: physique de la matière condensée

Thèse présentée et soutenue à Saint-Aubin, le 25 septembre 2018, par

Daniela Di Felice

Composition du Jury :

| | |
|--|--------------------|
| Andrew Mayne Directeur de Recherche CNRS Institut des Sciences Moléculaires d'Orsay | Président |
| Philippe Sonnet Professeur, Université de Haute Alsace, Institut de Sciences des Matériaux de Mulhouse | Rapporteur |
| Evelyne Martin-Lampin Chargée de Recherche CNRS Institut d'Electronique de Microrélectronique et Nanotechnologie | Rapporteur |
| Céline Fiorini Directrice de Recherche CEA Service de Physique de l'Etat Condensé, CEA Saclay | Examineur |
| Pascal Pochet Directeur de Recherche CEA Laboratoire de Simulation Atomistique INAC, CEA Grenoble | Examineur |
| Yannick Dappe Chargé de Recherche CNRS Service de Physique de l'Etat Condensé, CEA Saclay | Directeur de thèse |

Contents

| | | |
|----------|--|-----------|
| 1 | Introduction: van der Waals heterostructures and their applications | 5 |
| 2 | Theory and methods | 11 |
| 2.1 | Density Functional Theory | 11 |
| 2.1.1 | Approximations for exchange and correlation functional | 14 |
| 2.1.2 | Pseudo-potential approximation | 16 |
| 2.2 | Density Functional Theory in Fireball | 17 |
| 2.2.1 | Fireball orbitals | 19 |
| 2.2.2 | Charge density in Fireball | 19 |
| 2.2.3 | Total energy minimization | 20 |
| 2.3 | Scissor operator | 23 |
| 2.4 | Including weak and van der Waals interactions: the LCAO-S ² +vdW formalism | 24 |
| 2.5 | Transport calculations | 29 |
| 2.5.1 | Keldysh-Green formalism | 30 |
| 2.5.2 | Application of the Keldysh-Green formalism | 33 |
| 2.6 | Summary | 37 |
| 3 | Graphene/TMDC heterostructure | 39 |
| 3.1 | Graphene: the first 2D material | 39 |
| 3.2 | MoS ₂ monolayer: a 2D direct gap semiconductor | 43 |
| 3.3 | Graphene/MoS ₂ : different properties for different orientations? | 48 |
| 3.3.1 | Lattice mismatch problem: building the supercells | 48 |
| 3.3.2 | Four orientations: structural optimization | 50 |
| 3.3.3 | Global electronic properties | 52 |
| 3.3.4 | Local electronic properties: STM calculations | 55 |
| 3.4 | Oriented MoS ₂ on graphene: experimental results | 60 |
| 3.5 | MoSe ₂ /graphene: beyond van der Waals interaction | 62 |
| 4 | Graphene and MoS₂ for a new Field Effect Transistor generation | 69 |
| 4.1 | Graphene-MoS ₂ interface for a FET modelization | 73 |
| 4.1.1 | Band alignment in graphene/MoS ₂ heterostructure | 75 |
| 4.1.2 | Graphene/MoS ₂ electronic transport properties | 76 |
| 4.1.3 | Adding graphene layer: graphene/MoS ₂ /graphene | 78 |

| | | |
|----------|--|------------|
| 4.1.4 | MoS ₂ /graphene/MoS ₂ | 81 |
| 4.1.5 | MoS ₂ /graphene/MoS ₂ /graphene | 82 |
| 4.2 | hBN/graphene, the charge transfer depends on the DOS | 84 |
| 4.3 | Summary | 85 |
| 5 | Defects on MoS₂: detection by graphene tip | 89 |
| 5.1 | Introduction to defects on MoS ₂ and their characterization | 89 |
| 5.1.1 | State of art | 90 |
| 5.1.2 | Calculation parameters | 91 |
| 5.2 | STM images simulated with the graphene tip | 93 |
| 5.3 | Tip approach pristine and defected MoS ₂ monolayer | 95 |
| 5.3.1 | Pristine monolayer | 95 |
| 5.3.2 | S and Mo vacancy | 97 |
| 5.3.3 | Mo substitutional atoms | 100 |
| 5.4 | Summary | 103 |
| | Bibliography | 106 |

Résumé

L'isolement du graphène, une monocouche de graphite composée d'un plan d'atomes de carbone, a démontré qu'il est possible de séparer un seul plan d'épaisseur atomique, que l'on appelle matériau bidimensionnelle (2D), à partir des solides de Van de Waals (vdW). Grâce à leur stabilité, différents matériaux 2D peuvent être empilés pour former les hétérostructures de vdW. L'interaction vdW à l'interface étant suffisamment faible, les propriétés spécifiques de chaque matériau demeurent globalement inchangées dans l'empilement. En utilisant une démarche théorique et computationnelle basée sur la théorie de la fonctionnelle de la densité (DFT) et le formalisme de Keldysh-Green, nous avons étudié l'hétérostructure graphène/MoS₂. Le principal intérêt des propriétés spécifiques du graphène et du MoS₂ pour la conception d'un transistor à effet de champ réside dans la mobilité du graphène, à la base d'un transistor haute performance et dans le gap électronique du MoS₂, à la base de la commutation du dispositif. Tout d'abord, nous avons étudié les effets de la rotation entre les deux couches sur les propriétés électroniques à l'interface, en démontrant que les propriétés électroniques globales ne sont pas affectées par l'orientation. En revanche, les images STM (microscope à effet tunnel) sont différentes pour chaque orientation, en raison d'un changement de densité de charge locale. Dans un deuxième temps, nous avons utilisé l'interface graphène/MoS₂ en tant que modèle très simple de Transistor à Effet de Champ. Nous avons analysé le rôle des hétérostructures de vdW sur la performance du transistor, en ajoutant des couches alternées de graphène et MoS₂ sur l'interface graphène/MoS₂. Il a ainsi été démontré que la forme de la DOS au bord du gap est le paramètre le plus important pour la vitesse de commutation du transistor, alors que si l'on ajoute des couches, il n'y aura pas d'amélioration du comportement du transistor, en raison de l'indépendance des interfaces dans les hétérostructures de vdW. Cependant, cela démontre que, dans le cadre de la DFT, on peut étudier les propriétés de transport des hétérostructures de vdW plus complexes en séparant chaque interface et en réduisant le temps de calcul. Les matériaux 2D sont également étudiés ici en tant que pointe pour STM et AFM (microscope à force atomique) : une pointe de graphène testée sur MoS₂ avec défauts a été comparée aux résultats correspondants pour une pointe en cuivre. La résolution atomique a été obtenue et grâce à l'interaction de vdW entre la pointe et l'échantillon, il est possible d'éviter les effets de contact responsables du transfert d'atomes entre la pointe et l'échantillon. En outre, l'analyse des défauts est très utile du fait de la présence de nouveaux pics dans le gap du MoS₂ : ils peuvent ainsi être utilisés pour récupérer un pic de courant et donner des perspectives pour améliorer la performance des transistors.

Chapter 1

Introduction: van der Waals heterostructures and their applications

In 2004 Novoselov and Geim have isolated for the first time a *graphene* monolayer, a plane of carbon atoms representing the in-plane building block of graphite [1].

Graphene properties have already been theoretically studied in three previous papers, in 1947 by P.R. Wallace [2], in 1956 by J.W. McClure [3] and in 1984 by G.W. Semenoff [4]. However, the possibility to isolate a monolayer from graphite and perform electrical measurement on it was not believed to be possible because of thermal instability. Surprisingly, in October 2004, Novoselov, Geim and their collaborators were able to show the first graphene layer isolated from graphite and then transferred to a silicon substrate by means of a simple mechanical exfoliation using scotch tape.

Hence, for their success in the isolation, identification and characterization of graphene sheet, the two scientists were honored by Nobel Prize in Physics 2010. This work represents a decisive contribution to the development of a new branch of solid state physics: the study of bidimensional (2D) materials.

Furthermore, graphene is even more than the first 2D material isolated ever. The honeycomb disposition of carbon atoms (see Fig.1.1 left panel) characterized by *sp*² hybridization and the atomic thickness of 0.345 nm enable graphene to break many records in terms of strength, electricity and heat conduction. The main important property of graphene related to this work of thesis is given by its electronic structure, characterized by very special linear dispersion in the six corner of the Brillouin zone (see Fig.1.1 right panel), forming the well known Dirac cones. This dispersion is the reason why graphene shows very high electronic mobility with an upper limit of 200 000 cm²V⁻¹s⁻¹ [5]. Graphene can also be doped with electrons or holes to increase the electronic conductivity, normally reduced by the zero density of states at the Dirac points, being potentially better at conducting electricity than copper at room temperature.

The discovery of Novoselov and Geim regarding the isolation of a single plane of graphite demonstrates the possibility to separate a stable single layer from a class of layered ma-

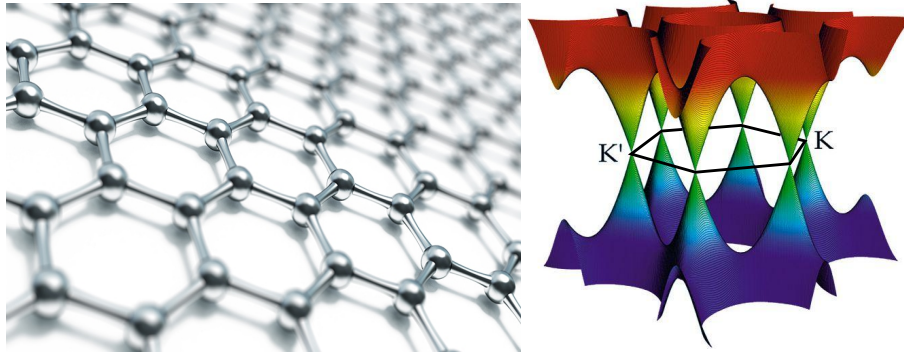


Figure 1.1: Atomic honeycomb configuration (left panel) and three dimensional band structure (right panel) of graphene characterized by six Dirac cones located at each corner of the graphene Brillouin zone.

materials called van der Waals (vdW) solids. The exfoliation of layered materials is possible thanks to the weak vdW attraction between the planes, as well as the stability of the single layer and the absence of any chemical electronic bond at the interfaces. In fact, the vdW attraction is not the result of a chemical bond, but is a quantum mechanical effect coming from the temporal fluctuation of electronic charges which induces dipoles at the interface. Despite their weak character, vdW interactions play a central role in many physical and chemical phenomena, and is of fundamental importance in this work of thesis, as we will see later.

In principle, one can imagine the existence of hundreds of layered materials that can be produced in monolayer as graphene. However, in isolating 2D crystals, one has to bear in mind that not the totality of them are stable under ambient conditions.

For example, a graphene monolayer is more reactive than even graphene bilayers and in general, many 2D crystals imaginable in theory are unlikely to exist in reality because they would corrode, decompose, segregate and so forth. So far, we count hundreds of 2D materials, classified in graphene family, 2D chalcogenides and 2D oxides as reported in Fig.1.2, even though not all of them are stable under ambient condition.

Since 2004, a large part of the scientific community in condensed matter physics have been involved in the study of graphene and all the possible 2D materials [6] beyond it. The enormous interest in this topic has to be found in the fascinating fundamental physics related to the bi-dimensional phase - the dimensionality being one of the most defining material parameters - and the specific properties coming from different 2D crystals. Moreover, both the common and the specific properties of 2D materials give them an important role for applications in nanoelectronics.

It is also interesting to notice that a wide range of physical properties can be designed in vdW materials, like insulator, metals, ferroelectrics, magnetics and superconductor. However, from 3D to 2D phase, these properties can be modified due to quantum confinement effects and the reduction of symmetry. Hence, in the low dimensional limit, one system may show different behaviours with respect to the corresponding bulk phase. Neverthe-

| Graphene family | Graphene | hBN 'white graphene' | BCN | Fluorographene | Graphene oxide |
|------------------|---|--|--|---|----------------|
| 2D chalcogenides | MoS ₂ , WS ₂ , MoSe ₂ , WSe ₂ | | Semiconducting dichalcogenides: MoTe ₂ , WTe ₂ , ZrS ₂ , ZrSe ₂ , and so on | Metallic dichalcogenides: NbSe ₂ , NbS ₂ , TaS ₂ , TiS ₂ , NiSe ₂ and so on | |
| | | | | Layered semiconductors: GaSe, GaTe, InSe, Bi ₂ Se ₃ and so on | |
| 2D oxides | Micas, BSCCO | MoO ₃ , WO ₃ | Perovskite-type: LaNb ₂ O ₇ , (Ca,Sr) ₂ Nb ₃ O ₁₀ , Bi ₄ Ti ₃ O ₁₂ , Ca ₂ Ta ₂ TiO ₁₀ and so on | Hydroxides: Ni(OH) ₂ , Eu(OH) ₂ and so on | |
| | Layered Cu oxides | TiO ₂ , MnO ₂ , V ₂ O ₅ , TaO ₃ , RuO ₂ and so on | | Others | |

Figure 1.2: Table of stable 2D materials in the blue section, the probably stable in the green and those unstable in air but may be stable in inert atmosphere in pink [8].

less, 2D crystals can exhibit unique physical properties that makes them one of the most extensively studied class of materials.

As well as graphene, one of the most studied category of the layered materials is constituted by Transition Metal Dichalcogenides (TMDC), in particular MoS₂ [7], characterized by a band gap around 2 eV. The direct gap in monolayer MoS₂ represents an important feature for optics and nanoelectronic applications, nevertheless it reduces and becomes indirect from bilayer to bulk phase. The semiconducting properties of TMDC have been largely used in nanoelectronics thanks to the intrinsic band gap, making possible one of the fundamental operation of electronic devices: the on/off switch of the signal. On the other hand, the well known problem of using graphene in electronics is related to the lack of electronic gap, resulting in the impossibility to switch off the devices, and consequently, to use it in logic circuits. However graphene, thanks to its mobility, is acclaimed as the perfect material for ultrafast high-performance transistor.

So, how can one combine graphene mobility with the TMDCs band gap and, in general, is it possible to use 2D crystals to create new materials without modifying the electronic characteristics of each 2D component?

In order to reply we cite here an expression used by Geim in Ref.[8]: “if one considers 2D crystals to be analogous to *Lego blocks*, the construction of a huge variety of layered structures becomes possible”.

In fact, according to the weak interaction keeping together the planes in a vdW solid, it is possible to make a further step imagining a vdW solid composed by different 2D crystals, namely the vdW heterostructure. The result is an artificial material assembled in a chosen sequence with one-atomic-plane precision. One example is provided by MoS₂/graphene interface. However, the great number of 2D crystals can provide a lot of combinations, increased by the possibility to combine them in a planar way, as well as in a vertical stacking. So far, many different heterostructures can be synthesized as graphene n-doped germanium [9–11], or on hexagonal boron nitride (hBN, a graphene like 2D material with

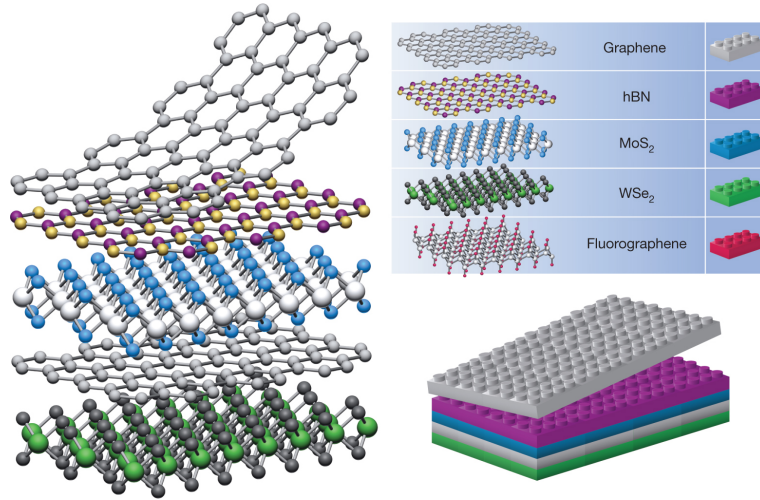


Figure 1.3: 2D crystals stacking as lego blocks [8].

alternate boron and nitrogen atoms) [12, 13], and in general TMDCs on graphene and so on [14]. Coming back to our question, the main interest in producing heterostructures lies in the possibility to keep the electronic properties of each layer as if they were isolated, thanks to the weakness of vdW interaction at the interface. In graphene/MoS₂ interface, for instance, one can still find the linear dispersion of graphene and the electronic gap provided by MoS₂.

However, this aspect represents one of the important opened question in the field of vdW heterostructures, since in some experimental and theoretical results the presence of a different layer on top or even the orientation between the layers is supposed to tune the electronic feature. It seems that, in some specific cases we will treat in this work of thesis, the interaction between graphene and MoS₂ is able to modify the structural and electronic properties of both materials according to some specific orientation angle between the lattice parameter of graphene and MoS₂ (like opening of a gap of some meV in graphene [16] or modification of the MoS₂ thickness [17]).

A very important aspect of the 2D materials and vdW heterostructures concerns their applications in nanoelectronics. The miniaturization of the electronic components requires structure at the nanometer scale, in which surface effects cannot be disregarded. But on the contrary, they are predominant and represent an increasingly way to build sophisticated devices.

One of the most important applications in nanoelectronics is the Field Effect Transistor (FET), an electronic device representing the basic building block of modern technology based on semiconductor electronics. It consists in a component of circuit able to amplify or switch the current, composed by a semiconductor channel connected with two metallic contacts, where the flowing current can be tuned by applying an electric field. Generally speaking, the progress of information and communication technology comes from the effort in improving the performances of this electronic component [18].

Traditionally, FETs are based on bulk or 3D semiconductor channels composed of silicon

and gallium arsenide (GaAs) semiconductors. Following the Moore's law, which in 1965 predicted that the density of transistors in a chip will double every two years [19–22], 3D materials have been scaled down to nanoscale dimension over the past five decades. Of course, there is a limit in the size reduction of 3D Field Effect Transistors (FET) related to short-channel [23, 24] and surface effects, due to the dangling bonds, causing the deterioration of transistor performance. The 2D materials, for instance, are characterized generally by the absence of dangling bonds at the interface, and in principle, the transfer of 2D crystal on top of the other leave the interfaces pristine. Hence, after the discovery of graphene, many other graphene-like materials like germanene, silicene and transition metal dichalcogenides (TMDC), started to be included in electronic devices to overcome some of the previously cited undesired effects. Many 2D FETs, mostly based on graphene due to its extraordinary properties, have been built or theoretically modeled in the last years.

In a FET architecture, the 2D materials can play the role of in-plane channel [25, 26] or electrodes and barrier as in the vertical tunneling transistor [27–30]. However, recently, a FET fully composed of 2D materials was built with graphene contacts, hBN dielectric and MoS₂ channel, exhibiting good performances [31]. As well as field effect transistor, even logic transistors, photovoltaic and memory devices are built using TMDC/graphene [28, 29, 32–37]. Furthermore, with the graphene/TMDC interface, the main problem related with the metal contacts like Fermi-level pinning, a finite Schottky barrier and large excessive contact resistance, are minimized. Moreover, the van der Waals coupling at the interface depends on different parameters like distance, twist angle, and stacking order of disparate 2D materials [38, 39]. For this reason, the interface interactions in vdW heterostructure is very important for their future high-performance device applications [40–43].

So far, we have illustrated the framework of this work of thesis. From this review about 2D materials, in particular, from the open question regarding the vdW interaction, the electronic and transport properties related to the 2D crystals and their possible applications, it is evident that the interest in this topic is very important. In fact, the effect of the vdW interaction is still under debate, the theoretical basis regarding the transport characteristics at the interface and, consequently, the inclusion of 2D materials in nanoelectronics need to be deeply investigated in order to know the future of 2D materials in nanodevices. These are the interest points that move this work of thesis devoted to 2D materials and vdW heterostructures.

In the following, a guideline of the manuscript is presented.

In the next chapter we present the general theoretical frame: Density Functional Theory approach is treated and the Fireball code we have used for structural, electronic and transport characterization is illustrated. Specific implementations in the code, as the inclusion of the vdW forces, the Keldysh-Green formalism for the transport calculation and the scissor operator for the band alignment, are presented as well.

In chapter 3, after a presentation of the most important characteristics of graphene and two different TMDC (namely MoS₂ and MoSe₂), we focus our attention on the rotation effect on the electronic and structural properties of graphene/MoS₂ heterostructures, as a way to answer to the open question on the possibility to tune the electronic properties by

the simple rotation. This problem was fully discussed by considering different supercells composed by graphene and MoS₂ rotated by different angles: the structural and electronic properties are deeply investigated and the effect of the orientation is fully described. The computational limit in approaching the study of supercells composed by crystals presenting an important lattice mismatch is also considered by previously studying the strain effects on the structure and electronic properties of each isolated component layer.

With the analysis of the strain effect on MoS₂ we also explain an experimental observation: changing the rotation angle between MoS₂ and graphene, the luminescence modification of MoS₂ was detected, sign of the direct to indirect evolution of the gap. The existence of a side effect related to the symmetry breaking due to an induced electric field is also considered in a system composed by SiC substrate on which a few-layer graphene and MoSe₂ are deposited.

In the fourth chapter, we focus on the transport properties at the MoS₂-graphene interface: the transverse current is calculated by applying a bias voltage between graphene and MoS₂. Moreover, different electronic band alignments between the layers, representing the effects of an external electric gating, are considered in terms of electric current modulation. The MoS₂/graphene heterostructure is treated as a very simple system to model a Field Effect Transistor.

Then, taking into account the limit regarding the size of the supercells, we considered the effects of the vertical stacking of alternate graphene and MoS₂ layer on the original graphene-MoS₂ interface. The aim is to investigate the role of the additional layer on the transport properties at the interface and to give a theoretical foundation to chose the best heterostructures for electronic applications, in particular Field Effect Transistor (FET). The charge transfer as a function of the gate voltage was analyzed and compared with the main parameters describing the FET performance.

In the last chapter, we provide an interesting application of the vdW interaction: a graphene tip for simultaneous Scanning Tunneling Microscope-Atomic Force Microscope (STM-AFM) measurement is used to theoretically characterize defected MoS₂ sample. A comparison between the copper metal tip, largely used in microscopy, and less reactive graphene tip, is provided. The vdW interaction is fully exploited in the field of microscopy application. Moreover, due to the huge impact that defects hold on the performance of the devices, the study of the MoS₂ structure and electronics considering some possible defects given by substitutional or missing atoms, is suitable in terms of the lost of performance.

In this work of thesis we aim to reply to the open questions regarding the vdW interaction and, in particular, we fully describe the role of the rotation on the electronic properties in vdW heterostructure, considering graphene/MoS₂ system. Furthermore, with the study of the transport at graphene-MoS₂ interface under different conditions, we aim to provide a new contribution for a further knowledge on the possible use of 2D crystals in electronic devices.

Chapter 2

Theory and methods

In this chapter we present the theoretical framework we have used along this thesis work, based on the Density Functional Theory (DFT). We detail the main features of the DFT Fireball numerical code we used to obtain the results of this work.

In the following parts we present some useful Fireball code tools beyond Density Functional Theory, like van der Waals interaction implementation, electronic transport, STM images calculations and scissor operator.

2.1 Density Functional Theory

The Density Functional Theory (DFT) is based on two initial works reported in publications coming almost 40 years after E. Schrödinger published his first epoch-making paper, marking the beginning of wave mechanics: the first on 1964 by P. Hohenberg and W. Kohn and the next by W. Kohn and Lu J. Sham on 1965. DFT is a mean-field approximation where all the electron-electron interactions are substituted by a mean-field potential acting on each individual electron. Therefore, the many-body (multi-electronic) Schrödinger equation can be rewritten as an average potential of all the electrons. The main variable here is the spatial electronic density $\rho(\mathbf{r})$. In addition, DFT is a theory of the fundamental state, since electronic excitation are not treated in this formalism.

The enormous progress in finding approximate solutions of Schrödinger's wave equation using this formalism, for systems with several electrons, was decisively aided by modern electronic computers.

DFT represents the state of the art in *ab initio* theories allowing the prediction of the electronic and structural properties of the system ground state, through the solution of the quantum mechanical model of the many-body system.

The Hohenberg and Kohn theorems

The foundation of the theory of electronic structure of matter is the nonrelativistic Schrödinger equation for the many-electron wave function Φ , whose Hamiltonian can be written as:

$$\hat{H} = -\frac{\hbar^2}{2m_e} \sum_i \nabla_i^2 + \sum_i V_{ext}(\mathbf{r}_i) + \frac{1}{2} \sum_{i \neq j} \frac{e^2}{|\mathbf{r}_i - \mathbf{r}_j|} \quad (2.1)$$

Here, the Born-Oppenheimer (or adiabatic) approximation allows us to decouple the electronic degrees of freedom from the nuclear ones: due to the large difference in the mass of electrons and nucleons, the electrons follow adiabatically the ions assuming at any given time their ground state configuration. In this Hamiltonian, we have the electron kinetic energy, the external potential depending on the position including also the nucleus-nucleus and the nucleus-ion interactions, and the Coulomb interaction between each pair of electrons in the positions \mathbf{r}_i and \mathbf{r}_j . Even if the adiabatic approximation brings to a simplified problem, the equation is still not easy to solve: we need another strategy to facilitate the calculations as that provide by DFT.

The Density Functional Theory is based on two theorems developed by P. Hohenberg and W. Kohn in 1964 [44, 45]:

- **Theorem I:** For any systems of interacting particles in an external potential $V_{ext}(\mathbf{r})$, the potential $V_{ext}(\mathbf{r})$ is determined *uniquely*, except for a constant, by the ground state particle density $\rho_0(\mathbf{r})$.

Corollary I: Since the external potential $V_{ext}(\mathbf{r})$ is fully determined, also the Hamiltonian \hat{H} is thus completely determined, except for a constant shift of the energy. It follows that the many-body wave-functions (*wfc*) for all states (ground and excited) are determined. Therefore all properties of the system are completely determined given only the ground state density $\rho_0(\mathbf{r})$.

- **Theorem II:** *Universal functional* for the energy in terms of the density can be defined: $E[\rho]$. For any $V_{ext}(\mathbf{r})$, the exact ground state energy of the system is the global minimum value of this functional $E[\rho]$ and the density $\rho(\mathbf{r})$ that minimizes the functional is the exact ground state density $\rho_0(\mathbf{r})$.

Corollary II: The functional $E[\rho]$ alone is sufficient to determine the exact ground state energy and density.

Thus, it is possible to write the functional $E[\rho]$ as

$$E[\rho] = F_{LL}[\rho] + \int V_{ext}(\mathbf{r})\rho(\mathbf{r})d\mathbf{r} \quad (2.2)$$

where $F_{LL}[\rho]$ is *universal* functional, meaning that it does not depend on the system in exam, except for the number of electrons, and also on V_{ext} . $E[\rho]$ minimum value is represented by the correct ground-state energy associated with $V_{ext}(\mathbf{r})$.

More details and the proof of the theorems can be found in Ref.[45].

The Kohn-Sham approach

The Hohenberg and Kohn (HK) theorem ensures the existence of a ground state charge density minimizing the total energy of the system. However, it does not provide any tool to succeed in calculating, that can be nothing but trivial. Kohn and Sham provide a new approach to carry out explicitly the variational procedure, based on the substitution of the original problem with an auxiliary one composed by independent particles that returns the same charge density of the original system [45].

We start by considering non interacting electrons subject to a *local potential* $V_S(\mathbf{r})$ determined by imposing that its charge density is the same as the interacting problem described with 2.1. It is possible to factorize the new Hamiltonian related to the auxiliary problem in terms of the one electron Hamiltonian:

$$H = -\frac{1}{2}\nabla^2 + V_S(\mathbf{r}). \quad (2.3)$$

The charge density can be written as

$$\rho = \sum_i^{occ.} |\psi_i|^2 \quad (2.4)$$

where ψ_i are the wave functions solution of (2.3).

Following the HK theorem, the energy functional can be written as

$$E_S = T_S[\rho] + \int V_S(\mathbf{r})d\mathbf{r}. \quad (2.5)$$

Since the HK theorem applies to any electron system, with or without interaction, we can say that the kinetic term T_S is the analogous of $F_{LL}[\rho]$ in (2.2) for the non interacting particles.

We then obtain the Kohn-Sham equation, solution of the (2.3):

$$\left(-\frac{\hbar^2}{2m}\nabla^2 + V_S(\mathbf{r})\right) \psi_i(\mathbf{r}) = \epsilon_i \psi_i(\mathbf{r}). \quad (2.6)$$

The new energy functional for interacting electrons in term of non interacting ones is given by

$$E[\rho] = F_{LL}[\rho] + \int V_{ext}(\mathbf{r})\rho(\mathbf{r})d\mathbf{r} = T_S[\rho] + \frac{1}{2} \int d\mathbf{r}d\mathbf{r}' \frac{\rho(\mathbf{r})\rho(\mathbf{r}')}{|\mathbf{r} - \mathbf{r}'|} + \int V_{ext}(\mathbf{r})d\mathbf{r} + E_{XC}[\rho] \quad (2.7)$$

where:

- $E_H[\rho] = (1/2) \int d\mathbf{r}d\mathbf{r}' \rho(\mathbf{r})\rho(\mathbf{r}')/|\mathbf{r} - \mathbf{r}'|$ is the *Hartree* term describing classical Coulomb interactions;

- $E_{XC}[\rho]$ is the *exchange-correlation* term which contains the many-body contributions. In $E_{XC}[\rho]$ are enclosed all terms not included in $T_S[\rho]$ and $E_H[\rho]$ that we rewrite in terms of Hohenberg-Kohn's functionals:

$$E_{XC}[\rho] = F_{LL}[\rho] - (T_S[\rho] + E_H[\rho]) \quad (2.8)$$

from which we can see that also $E_{XC}[\rho]$ is a universal functional.

Now, we can minimize 2.7:

$$E[\rho + \delta\rho] - E[\rho] = \delta T_S + \int \delta\rho \left[V_{ext}(\mathbf{r}) + \int \frac{\rho(\mathbf{r}')}{|\mathbf{r} - \mathbf{r}'|} d\mathbf{r}' + V_{XC}([\rho_0], \mathbf{r}) \right] = 0 \quad (2.9)$$

where $V_{XC}([\rho_0], \mathbf{r}) = \delta E_{XC} / \delta\rho(\mathbf{r})|_{\rho_0}$ represents the *exchange-correlation potential*. This term has a key feature: it is *local*, depending only on the position in which we evaluate its contribution, unlike E_{XC} which may have much more complicated functional form.

Repeating this procedure also for the non interacting particles functional in (2.5) we have that

$$\delta T_S + \int \delta\rho V_S(\mathbf{r}) = 0 \quad (2.10)$$

with

$$V_S(\mathbf{r}) = V_{ext}(\mathbf{r}) + \int \frac{\rho(\mathbf{r}')}{|\mathbf{r} - \mathbf{r}'|} d\mathbf{r}' + V_{XC}([\rho_0], \mathbf{r}). \quad (2.11)$$

We have to remark that no approximation was adopted at this point. The Kohn-Sham equation must be solved in a self-consistent way to calculate ρ , as shown in the scheme in Fig.2.1. At the end of each self consistent loop we get the minimum energy state, namely the ground state, related to a specific electron density ρ_{SC} . Due to the relation between the electron density and the potential, the obtained electron density is used to calculate the potential of the new loop. In particular, a mix between the new and the old density is used for the next iteration. The self consistency is reached when both the last potentials or densities are equal (with a chosen accuracy) to the previous one.

2.1.1 Approximations for exchange and correlation functional

As we said in the previous section, DFT is an exact theory, however the exchange and correlation term is very difficult to determine. For that reason, it is necessary to use an approximation. In 1965 Kohn and Sham introduced the *Local Density Approximation* (LDA) for the exchange-correlation term [46]. This approximation is largely used in the calculations of the total energy because it gives good results even though it can be classified as the simplest approximation. In this picture the exchange-correlation functional $E_{XC}[\rho(\mathbf{r})]$ and the related potential are written in the following form:

$$E_{XC}^{LDA}[\rho(\mathbf{r})] = \int \epsilon_{xc}(\rho(\mathbf{r}))\rho(\mathbf{r})d\mathbf{r} \quad (2.12)$$

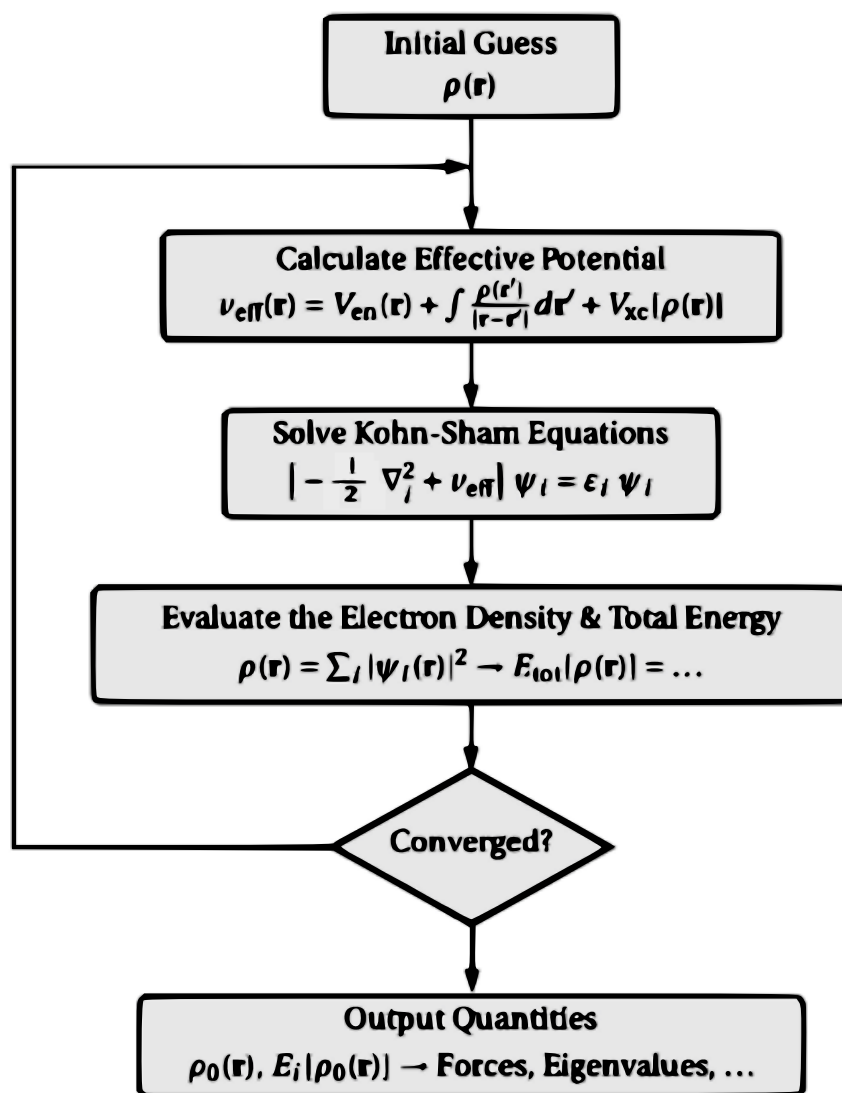


Figure 2.1: Scheme of self-consistent loop for the charge density optimization.

$$V_{XC}^{LDA}(\mathbf{r}) = \frac{\delta E_{XC}^{LDA}}{\delta \rho(\mathbf{r})} = \epsilon_{xc}(\rho(\mathbf{r})) + \rho(\mathbf{r}) \frac{d\epsilon_{xc}(\rho(\mathbf{r}))}{d\rho(\mathbf{r})} \quad (2.13)$$

where $\epsilon_{xc}(\rho(\mathbf{r}))$ is the exchange-correlation density per electron evaluated for a uniform electron gas at the same density $\rho(\mathbf{r})$ of the considered system [47].

There exist different parametrizations of the exchange-correlation term (xc) for the homogeneous electron gas. For example, different interpolations of the exact calculated results for extreme cases, namely very high or very low homogeneous electron gas density, are used.

The LDA approximation has a local character: the xc term in the position \mathbf{r} does not take into account the inhomogeneity of the electron density in the proximity. One improved approximation, *Generalized Gradient Approximation* (GGA), takes into account also the gradient of the charge density [48]:

$$E_{XC}^{GGA}[\rho(\mathbf{r})] = \int \epsilon_{xc}[\rho(\mathbf{r}), \nabla \rho(\mathbf{r})] \rho(\mathbf{r}) d\mathbf{r}, \quad (2.14)$$

where the gradient corrections constitute a semi-local approach which, in some way, capture non-local effects at longer ranges.

LDA gives really good results in many investigated systems despite its simplicity. However it reveals, together with GGA, documented failure in the description of strongly correlated system like, for instance, Mott insulator.

In our work we will use the LDA approximation, since it represents a very good approximation for the studied materials.

2.1.2 Pseudo-potential approximation

The concept of pseudo-potential is based on the separation between the core and valence electrons: the idea is to include the core electrons together with the atomic nuclei in the effective potential affecting the valence electrons. The pseudo-potentials are constructed with the requirement that the valence wave functions calculated by using them are equivalent to the all electron ones beyond a cut-off radius. This approximation is reasonable since the physical properties of materials mostly depend on the valence electrons.

In general, both empirical or *ab initio* methods can be used to calculate pseudo-potentials. The big advantage to use pseudo-potentials is to drastically reduce the calculation time, since the size of the wavefunction basis set and, consequently, the number of interactions is reduced.

In order to get the pseudo-potential, the Kohn-Sham equation for a single atoms including all the atoms has to be solved. It is required that the pseudo-eigenfunctions ϕ_α are equal to the original eigenfunction for a distance larger than a specific radius, r_{core} , and smooth functions for smaller distance.

There are different ways to build the pseudo-potentials. Once we consider one method [49–53], the value of the parameters are chosen and then the pseudo-eigenfunctions and pseudo-eigenvalues of the pseudo-potential are found following a self-consistent process.

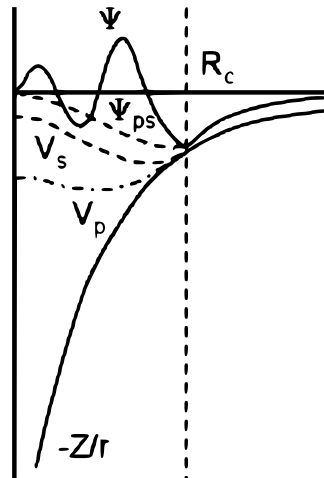


Figure 2.2: Representation of all electron potential and wave function (pseudo-potential and pseudo-eigenfunction) in continuous (dashed) lines. R_C is the core radius r_{core} .

The self consistency is reached when the eigenvalues (and eigenfunctions) of the all electron calculation and the pseudo-eigenvalues (pseudo-eigenfunction) are equal beyond the core radius.

The obtained pseudo-eigenvalues and pseudo-eigenfunctions, represented in Fig.2.2, satisfy different conditions like the independence on the n quantum number (related to the smoothness of pseudo-eigenfunctions): for $r = r_{core}$, the radial part of the pseudo-eigenfunction for each quantum number l has to be equal to the eigenfunction coming from all-electrons calculations. Furthermore the charge inside r_{core} calculated from pseudo-eigenfunctions and from eigenfunctions have to be the same and, of course, the eigenvalues for the valence state in both cases have to be the same, as well. These conditions allow us to define a pseudo-potential as norm-conserving pseudo-potential [50, 54]. Outside r_{core} , the potential is proportional to Z_{ion}/r following the Coulomb law, while inside r_{core} the potential is repulsive and depends on angular momentum. A further approximation of Kleinman and Bylander [55] is used to reduce the computational time.

2.2 Density Functional Theory in Fireball

In the previous sections we have presented the basic functional of the energy given by Kohn-Sham. However many different expressions of the energy functional can be used in terms of electronic density. One example is given by the Fireball method: a tight-binding formalism based on the selfconsistent Harris-Foulkes functional [56]. In order to solve the one-electron Schrödinger equation (see Eq.2.1), we use a set of numerical atomic-like orbitals based on a pseudo-potential formalism. The construction of the pseudopotentials starts by solving the self-consistent Kohn-Sham equations for all electrons of the free atom,

by using various parametrizations as LDA or GGA, previously described. Once the single particle equation for all electrons of the free atom is solved, the pseudopotential and pseudo-atomic wavefunctions are generated.

The Fireball localized pseudo-atomic orbitals are expressed as $\phi_{\text{Fireball}}^{\text{atomic}}(r) = f(r)Y_{lm}(\theta, \psi)$, where $f(r)$ is the radial component and $Y_{lm}(\theta, \psi)$ is the angular component which are the spherical harmonic functions. The Fireball orbitals are slightly excited due to the boundary conditions that they vanish at some radius r_c , like a particle in the box, having the effect of raising the electronic energy levels. The r_c 's are chosen to preserve the chemical trends of the atoms, *i.e.*, the relative ionization energies and relative atomic sizes.

Moreover, the fireball orbitals are advantageous from a computational point of view since beyond the cutoff radius ($r_{ci} + r_{cj}$), where i and j define two atomic orbitals, the matrix elements H_{ij} and S_{ij} become zero, and a range over which the integrals are evaluated is defined.

A multi-center approach is used so that all interactions up to three-centers integrals are computed exactly. In Fireball, the integrals are pre-calculated, their values stored in a directory and then interpolated when the specific values are needed. This represents an advantageous point of this code, since the integrals depend only on the atom type, their r_c values, and the type of DFT exchange-correlation functional used. Therefore, it is possible to generate the integral tables only once for a given number of atomic species, rather than each step during the simulations.

At the basis of Fireball method there is the replacement of the Kohn-Sham energy functional by the Harris-Foulkes one given by [57–59]

$$E_{\text{tot}}^{\text{Harris}} = \sum_{i=1}^N \epsilon_n + \{U^{\text{ion-ion}} - U^{\text{ee}}[\rho(\mathbf{r})]\} + \{U^{\text{xc}}\rho(\mathbf{r}) - V^{\text{xc}}\rho(\mathbf{r})\}. \quad (2.15)$$

where ϵ_n are the eigenvalues of the one-electron Schrödinger equation, whereas the second term is the difference between the repulsive interaction of the pseudocores and of the valence-electron densities (the electron-electron repulsion corrects for the double counting in the sum of eigenvalues); the last term is the correction of the exchange-correlation, given by $\int \rho\{\epsilon_{\text{xc}}[\rho(\mathbf{r})] - \mu_{\text{xc}}[\rho(\mathbf{r})]\}$.

The important difference with the Kohn-Sham functional is that KS is an equation in terms of the charge density $\rho(\mathbf{r})$, whereas here we define the functional in terms of occupation number n_i from which the charge density is evaluated:

$$\rho_{\text{in}}(\mathbf{r}) = \sum_i n_i |\phi_i(\mathbf{r} - \mathbf{R}_i)|^2. \quad (2.16)$$

The orbitals $\phi_i(\mathbf{r} - \mathbf{R}_i)$ corresponds to the slightly excited Fireball pseudo-atomic wavefunctions, used as basis functions to solve the one-electron Schrödinger equation. The occupation number n_i , defining the number of electrons occupying each spherically confined atomic-like densities, is given by $n_i = n_i^o + \delta n_i$ and it is calculated self-consistently.

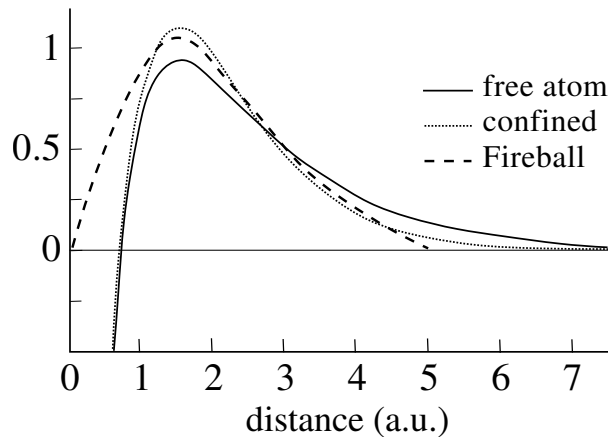


Figure 2.3: An example of the 3p orbital of Si calculated with Fireball, free and confined cutoff radius.

In this scheme, the total energy has an error that is calculated to be only of the second order in the errors of the input density.

2.2.1 Fireball orbitals

As it was said previously, the Fireball basis orbitals are the atomic like orbitals $\{\phi_\mu(\mathbf{r})\}$ with the characteristic to be zero for $\mathbf{r} > \mathbf{r}_{cutoff}$ (see Fig.2.3). The cutoff radius for each orbitals (of each element involved in the studied system) are the parameters we need to adjust in order to get a good basis set. The choice of the good cutoff radius needs the comparison of some properties with experimental results or with results obtained from planewave DFT calculations. Some checking can be done for example by comparing the lattice parameters, bulk modulus, or electronic band structures.

The advantage of the Fireball orbitals, being zero starting from the cutoff radius, has a double effect: first, it gives a finite number of interactions, since a maximum distance of interaction is introduced, and then it avoids the problems related to the interaction with many atoms.

2.2.2 Charge density in Fireball

We have already written the equation for the electronic density, however we report it here for convenience:

$$\rho_{in}(\mathbf{r}) = \sum_i n_i |\phi_i(\mathbf{r} - \mathbf{R}_i)|^2 \quad (2.17)$$

where i runs over all the orbitals. As we said in the previous section, the occupation numbers n_i are calculated within a self-consistent loop, providing an evolution of n_i from

the neutral value (example: $n_s = 2$ and $n_p = 2$ for carbon) to the final value n^{out} where a non-neutral contribution is included. We can define

$$n_i^{out} = \sum_n |\langle \psi_n | \varphi_i \rangle|^2 \quad (2.18)$$

where ψ_n are the wave functions of the occupied state and φ_i are the orthogonal orbitals obtained from the atomical orbitals ϕ_i thanks to a Löwdin transformation [60], as explicated here:

$$\varphi_i = \sum_j (S^{\frac{1}{2}})_{ij} \phi_j \quad (2.19a)$$

$$(S)_{ij} = \langle \phi_i | \phi_j \rangle \quad (2.19b)$$

If the atomic charge can vary, the charge distribution will be different from the one of the neutral atom, meaning that long range interactions occur. For this reason we can write the occupation number as we previously shown

$$n_i = n_i^0 + \delta n_i \quad (2.20)$$

where n_i^0 is the occupation number for a neutral atom, whereas δn_i describes the charge transfer between the different atoms of the system. The input electron density in eq.2.17 induces a one electron potential which has both long-range (due to δn_i) and short-range contributions to the single-particle Hamiltonian matrix element:

$$h_{ij} = \langle \phi_i(\mathbf{r} - \mathbf{R}_i) | (-\frac{1}{2}\nabla^2 + V[\rho]) | \phi_j(\mathbf{r} - \mathbf{R}_j) \rangle = h_{ij}^{SR} + h_{ij}^{LR} \quad (2.21)$$

where h_{ij}^{SR} includes the contribution of the kinetic energy, atomic pseudo-potential, xc energy and the neutral contribution of the Hartree term (for further detail see [61]). The LR term includes the Hartree contribution of the non-neutral part (see.[59]).

2.2.3 Total energy minimization

So far we have illustrated the minimization of the electronic part of the system. Once the optimized electronic structure is reached after the self consistency, the forces acting on the atoms are calculated and the ions are moved. The total energy is a function of the ions coordinate $\{\mathbf{R}_i\}$ defined as x in the following, and the direction of the ion motion is determined from the gradient of the energy

$$\mathbf{g}^1 = -\frac{\delta E}{\delta \mathbf{x}} \Big|_{x=x^1} = -G\mathbf{x}^1 \quad (2.22)$$

where E is the total energy function and the superscript 1 refers to the first selfconsistent loop. In order to minimize the energy function, the ions have to move to the new position given by

$$\mathbf{x}^2 = \mathbf{x}^1 + b^1 \mathbf{g}^1, \quad (2.23)$$

where b is found to minimize $E[\mathbf{x}^1 + b^1 \mathbf{g}^1]$. In a range of values of E calculated on the $\mathbf{x}^1 + b^1 \mathbf{g}^1$ direction, b^1 is the value that corresponds to the minimum of E where that direction is perpendicular to the gradient of the function given by $G(\mathbf{x}^1 + b^1 \mathbf{g}^1)$. In this way, it is possible that a big number of iterations is necessary, since we are constraining the vector \mathbf{x}^m , being orthogonal to the previous \mathbf{x}^{m-1} .

Hence, the best algorithm to minimize the total energy is the following, called conjugated gradients:

$$\mathbf{d}^m = \mathbf{g}^m + \gamma^m \mathbf{d}^{m-1} \quad (2.24)$$

$$\gamma^m = \frac{\mathbf{g}^m \dot{\mathbf{g}}^m}{\mathbf{g}^{m-1} \dot{\mathbf{g}}^{m-1}} \quad (2.25)$$

$$\mathbf{g}^m = -\left. \frac{\delta E}{\delta \mathbf{x}} \right|_{x=x^m}. \quad (2.26)$$

In this way, the first displacement is given by the gradient of E with opposite sign, the second direction is the linear combination of the new gradient and the first one and so on. This method is fast and not expensive in time and memory.

The total energy minimization represents a bigger loop that contains the charge self-consistency: for each ionic configuration, the charge selfconsistency is calculated until a convergence is reached; then the ions move following this algorithm and a new charge selfconsistency loop starts (see scheme in Fig.2.4). This procedure ends when the energy functional is minimized and the charge selfconsistency is reached.

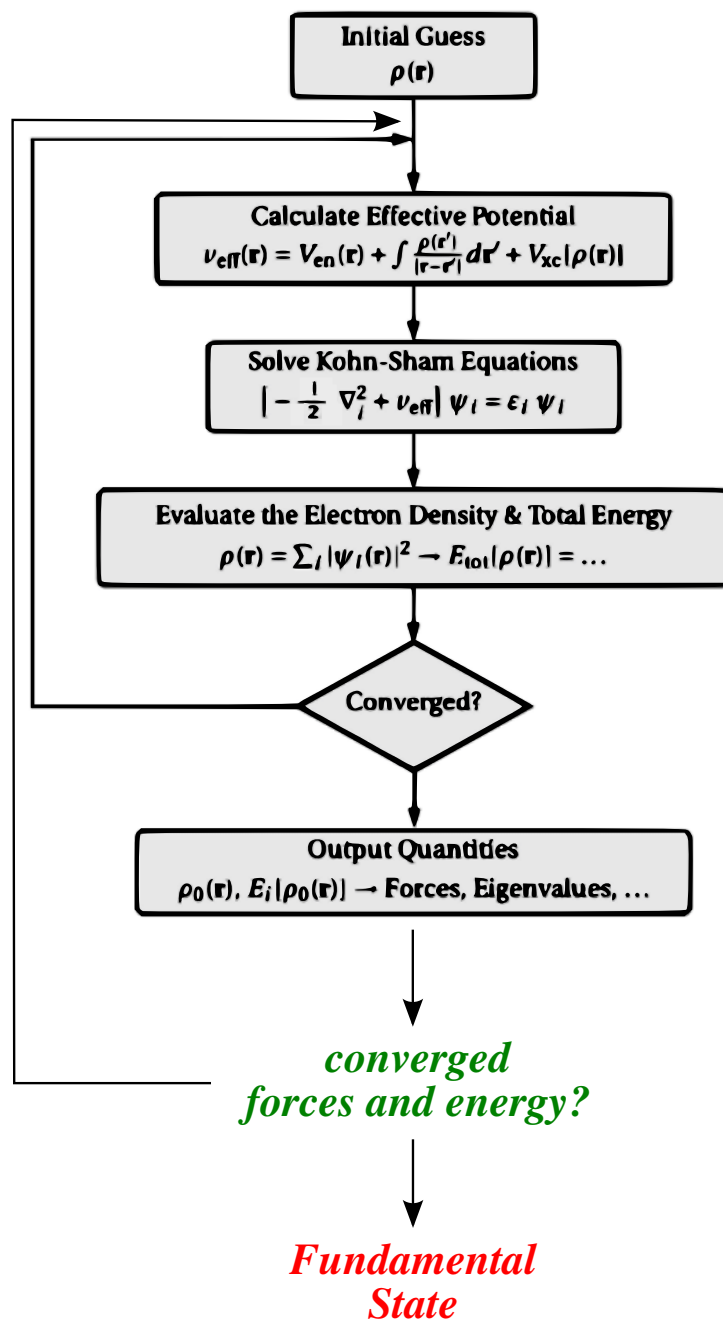


Figure 2.4: Scheme of the self-consistent loop included in a bigger loop involving the energy minimization.

2.3 Scissor operator

The scissor operator is a tool present in the Fireball code that allows us to move the eigenvalue of each orbital of a given value. This operator can be used to reach the good band alignment between different parts of the systems or to simulate the application of a voltage on a part of it.

We will only give a short description in this paragraph, for more details refer to [62, 63]. In general, the scissor operator is able to move each band $\varepsilon_\alpha(\mathbf{k})$ a value $\Delta_\alpha(\mathbf{k})$. Taking advantage of the properties of projectors, it can be written as:

$$O^S = \sum_{\alpha, \mathbf{k}} \Delta_\alpha(\mathbf{k}) |\alpha(\mathbf{k})\rangle \langle \alpha(\mathbf{k})| \quad (2.27)$$

where $|\alpha(\mathbf{k})\rangle$ is the eigenorbital with energy $\varepsilon_\alpha(\mathbf{k})$. We will calculate the matrix elements of the scissor operator in the Fireball basis set for periodic systems:

$$|B_{\mu,i}(\mathbf{k})\rangle = \frac{1}{\sqrt{N}} \sum_{\mathbf{R}} e^{i\mathbf{k}(\mathbf{R}+\mathbf{r}_i)} |\phi_{\mu,i}\rangle \quad (2.28)$$

where $|\phi_{\mu,i}\rangle$ is the numeric atomic orbital of the orbital μ of atom i (at \mathbf{r}_i). If we expand $|\alpha(\mathbf{k})\rangle$ in this basis set:

$$|\alpha(\mathbf{k})\rangle = \sum_{\lambda,l} b_{\lambda,l}^\alpha(\mathbf{R}) |B_{\lambda,l}(\mathbf{k})\rangle \quad (2.29)$$

we get that the scissor operator matrix element $\langle B_{\mu,i}(\mathbf{k}) | O^S | B_{\nu,j}(\mathbf{k}) \rangle$ takes the form:

$$\langle B_{\mu,i}(\mathbf{k}) | O^S | B_{\nu,j}(\mathbf{k}) \rangle = \sum_{\alpha} \Delta_\alpha(\mathbf{k}) \langle B_{\mu,i}(\mathbf{k}) | \left(\sum_{\lambda,l} b_{\lambda,l}^\alpha(\mathbf{R}) |B_{\lambda,l}(\mathbf{k})\rangle \right) \times \quad (2.30)$$

$$\times \left(\sum_{\sigma,m} b_{\sigma,m}^{\alpha,*}(\mathbf{R}) \langle B_{\sigma,m}(\mathbf{k}) | \right) | B_{\nu,j}(\mathbf{k}) \rangle = \quad (2.31)$$

$$\sum_{\alpha, l, m, \lambda, \sigma} \Delta_\alpha(\mathbf{k}) b_{\lambda,l}^\alpha(\mathbf{R}) b_{\sigma,m}^{\alpha,*}(\mathbf{R}) \underbrace{\langle B_{\mu,i}(\mathbf{k}) | B_{\lambda,l}(\mathbf{k}) \rangle}_{S_{\mu,i;\lambda,l}(\mathbf{k})} \underbrace{\langle B_{\sigma,m}(\mathbf{k}) | B_{\nu,j}(\mathbf{k}) \rangle}_{S_{\sigma,m;\nu,j}(\mathbf{k})} \quad (2.32)$$

where $S_{\mu,i;\lambda,l}(\mathbf{k})$ is the overlap matrix element between the orbital μ of atom i and the orbital λ of atom l .

In this work, the scissor operator is used to find the good alignment between graphene and MoS₂ in graphene/MoS₂ van der Waals heterostructure, as well as to simulate the application of a gate voltage in some specific layer in the Field Effect Transistor modelization.

2.4 Including weak and van der Waals interactions: the LCAO-S²+vdW formalism

The van der Waals (vdW) interaction comes from a quantum mechanical effect: the normal charge fluctuation occurring in the atoms and molecules, provide oscillating dipoles whose average value in time is zero. However, these dipoles interact leading to the van der Waals interactions among others. Due to its central importance for many physical, chemical and biological phenomena, it was important to include it in DFT formalism. However, this is not a simple task. In fact, the standard approximations used in DFT to model the exchange-correlation term completely miss the long distance interaction like the vdW ones. One way to include the vdW interaction is to add to DFT a value coming from a semiempirical approach: $V_{vdW} = -f_d(R)C_6/R^6$, where R is the distance between a pair of atoms, $f_d(R)$ is a damping function going to zero for short distances and the coefficient C_6 that depends on the type of atoms. A second way is to add a new functional in DFT that includes the vdW interaction. However, in complex systems it could be very expensive. A third method is implemented in Fireball: once the separated single layers are calculated in DFT, the vdW interaction treated in perturbation theory is included. In the method we are going to present, the linear combination of atomic orbitals-orbital occupancy (LCAO-OO), where the energy and potential are expressed in terms of the orbital occupancies, is used since it gives a connection between the local orbital DFT of Fireball approach and intermolecular perturbation theory in second quantization formalism [64].

In LCAO-OO method, the eigenfunction are written as the linear combination of atomic orbitals $\psi_n(\mathbf{r}) = \sum_{i\alpha}^{(n)} c_{i\alpha}^{(n)} \varphi(\mathbf{r} - \mathbf{R}_i)$ where i and α run over the atoms and their orbitals, respectively and $\varphi_{i\alpha}$ are given by Eq.2.19.

First of all, we write the general Hamiltonian in second quantization formalism, separating the one-electron term from the many body part:

$$\hat{H} = \sum_{v,\sigma} (\epsilon_v + V_{vv,\sigma}^{ps}) \hat{n}_{v,\sigma} + \sum_{\mu \neq v,\sigma} (t_{\mu v} + V_{v\mu,\sigma}^{ps}) \hat{c}_{\mu\omega}^\dagger \hat{c}_{v\sigma} + \frac{1}{2} \sum_{\nu\omega\sigma\mu\lambda\sigma'} O_{\omega\lambda}^{v\mu} \hat{c}_{v\sigma}^\dagger \hat{c}_{\mu\sigma'}^\dagger \hat{c}_{\lambda\sigma'} \hat{c}_{\omega\sigma} \quad (2.33)$$

where V^{ps} is the pseudopotential, and

$$\begin{aligned} \epsilon_v &= \int \varphi_v(\mathbf{r}) \left(-\frac{1}{2} \nabla^2 + \sum_j \frac{Z_j}{|\mathbf{r} - \mathbf{R}_j|} \right) \varphi_v(\mathbf{r}) d\mathbf{r}, \\ t_{\mu v} &= \int \varphi_\mu(\mathbf{r}) \left(-\frac{1}{2} \nabla^2 + \sum_j \frac{Z_j}{|\mathbf{r} - \mathbf{R}_j|} \right) \varphi_v(\mathbf{r}) d\mathbf{r}, \\ O_{\omega\lambda}^{v\mu} &= \int \varphi_v(\mathbf{r}) \varphi_\omega(\mathbf{r}) \frac{1}{\mathbf{r} - \mathbf{r}'} \varphi_\mu(\mathbf{r}') \varphi_v(\mathbf{r}') d\mathbf{r} d\mathbf{r}' = (v\omega|\mu\lambda). \end{aligned} \quad (2.34)$$

The many body contribution can be written as:

$$\begin{aligned}
 \sum_{v\omega\sigma\mu\lambda\sigma'} O_{\omega\lambda}^{v\mu} \hat{c}_{v\sigma}^\dagger \hat{c}_{\mu\sigma'}^\dagger \hat{c}_{\lambda\sigma'} \hat{c}_{\omega\sigma} &= \sum_v U_v \hat{n}_{v\uparrow} \hat{n}_{v\downarrow} + \frac{1}{2} \sum_{\mu \neq v, \sigma\sigma'} I_{v\mu} n_{v\sigma} \hat{n}_{v\sigma'} \\
 &+ \frac{1}{2} \sum_{\mu \neq v, \lambda, \sigma\sigma'} h_{\lambda, \mu v} \hat{n}_{\lambda\sigma'} \hat{c}_{v\sigma}^\dagger \hat{c}_{v\sigma} - \sum_{v \neq v, \lambda, \sigma} h_{\lambda, \mu v}^x \lambda \sigma \hat{c}_{v\sigma}^\dagger \hat{c}_{v\sigma} \\
 &+ \frac{1}{2} \sum_{N.N.} O_{\omega\lambda}^{\mu\nu} (\hat{c}_{\mu\sigma}^\dagger \hat{c}_{\omega\sigma}) (\hat{c}_{v\sigma'}^\dagger \hat{c}_{\lambda\sigma'}),
 \end{aligned} \tag{2.35}$$

where the terms U_μ , $J_{\mu\nu}$, $h_{\lambda, \mu\nu}$, and $h_{\lambda, \mu\nu}^x$ are defined by

$$h_{\lambda, \mu\nu} = \int \varphi_\lambda^2(\mathbf{r}) \frac{1}{|\mathbf{r} - \mathbf{r}'|} \varphi_\mu(\mathbf{r}') \varphi_\nu(\mathbf{r}') d\mathbf{r} d\mathbf{r}', \tag{2.36}$$

$$h_{\lambda, \mu\nu}^x = \int \varphi_\lambda(\mathbf{r}) \varphi_\nu(\mathbf{r}) \frac{1}{|\mathbf{r} - \mathbf{r}'|} \varphi_\lambda(\mathbf{r}') \varphi_\mu(\mathbf{r}') d\mathbf{r} d\mathbf{r}', \tag{2.37}$$

$$U_\mu = \int \varphi_\nu^2(\mathbf{r}) \frac{1}{|\mathbf{r} - \mathbf{r}'|} \varphi_\nu^2(\mathbf{r}') d\mathbf{r} d\mathbf{r}', \tag{2.38}$$

$$J_{\mu\nu} = \int \varphi_\nu^2(\mathbf{r}) \frac{1}{|\mathbf{r} - \mathbf{r}'|} \varphi_\mu^2(\mathbf{r}') d\mathbf{r} d\mathbf{r}'. \tag{2.39}$$

A Löwdin orthonormal basis set φ_μ (see eq.2.19) is used to define the creation and annihilation operators, \hat{c}^\dagger and \hat{c} respectively, with $\hat{n} = c^\dagger c$.

The Hamiltonian equation is divided in two main parts composed by the first two terms ($\epsilon_v + V_{vv, \sigma}^{ps}$ and $t_{\mu\nu, \sigma} + V_{v\mu, \sigma}^{ps}$) related with the one-electron contribution and the last term defining the electron-electron ones. In the LCAO-OO formalism, the Hamiltonian 2.33 can be divided in two parts given by

$$\hat{H}_0 + \delta\hat{H}$$

where \hat{H}_0 is composed by one-electron + intratomic + interatomic interaction terms, whereas the vdW interaction is included in $\delta\hat{H}$, which contains all the four-electrons terms. \hat{H}_0 can be written in this form:

$$\begin{aligned}
 \hat{H}_0 &= \sum_{v\sigma} (\epsilon_v + V_{vv, \sigma}^{ps}) \hat{n}_{v\sigma} + \sum_{v \neq \mu, \sigma} \hat{T}_{v\mu, \sigma} \hat{c}_{v\sigma}^\dagger \hat{c}_{\mu\sigma} + \sum_v U_v \hat{n}_{v\uparrow} \hat{n}_{v\downarrow} \\
 &+ \frac{1}{2} \sum_{v, \mu \neq v, \sigma} [J_{v\mu} \hat{n}_{v\sigma} \hat{n}_{\mu\bar{\sigma}} + (J_{v\mu} - J_{v\mu}^x) \hat{n}_{v\sigma} \hat{n}_{\mu\bar{\sigma}}],
 \end{aligned} \tag{2.40}$$

where

$$\hat{T}_{v\mu, \sigma} = (t_{v\mu} + V_{v\mu, \sigma}^{ps} + \sum_{\lambda, \sigma'} h_{\lambda, v\mu} \hat{n}_{\lambda, \sigma'} - \sum_{\lambda} h_{\lambda, v\mu}^x \hat{n}_{\lambda\sigma}),$$

$U_v = (vv|vv)$, $J_{v\mu} = (vv|\mu\mu)$, $J_{v\mu}^x = (v\mu|v\mu)$, $h_{\lambda,v\mu} = (\lambda\lambda|v\mu)$ and $h_{\lambda,v\mu}^x = (\lambda v|\lambda\mu)$ as in eq.2.34.

The first step is to find the DFT solution for each layer independently. For this purpose, we can use the DFT Fireball code, since it is based on orbital occupancy instead of electron density, and it is compatible with the LCAO-OO approach.

From this calculation we obtain the following eigenstates:

$$\varphi_n(\mathbf{k}) = \sum_i c_{ni}(\mathbf{k})\psi_i^0 = \sum_i a_{ni}(\mathbf{k})\phi_i, \quad (2.41)$$

where the eigenvalues $\epsilon_n(\mathbf{k})$ and the occupation numbers $\{n_{i,\sigma}\}$ are also obtained from the DFT calculations for independent layers. A useful definition of the symbol is necessary: \mathbf{k} is the momentum parallel to the planes, n is the band index and ψ_i^0 are the orthonormal basis orbitals within each layer obtained from the Löwdin expansion.

The second step concerns the analysis of the intermolecular interaction contributions, starting from the one-electron contributions: it arises from orthogonalisation, namely the overlaps $S_{\mu\nu} = \langle\phi_\mu|\phi_\nu\rangle$, and from the hopping matrix elements T between atomiclike orbitals in different layers (the eigenfunctions of each layer are orthonormalized). However, the overlap is small and its effects on the energy can be described by a (S^2) expansion [65–67] that induces a shift in the occupied eigenvalues of each layer. The energy shift for one layer is written in terms of overlap $S_{nm}(\mathbf{k})$ and hopping $T_{mn}(\mathbf{k})$ integrals as following:

$$\delta^S \epsilon_n(\mathbf{k}) = - \sum_m \frac{1}{2} [S_{nm}(\mathbf{k})T_{mn}(\mathbf{k}) + T_{nm}(\mathbf{k})S_{mn}(\mathbf{k})] + \frac{1}{4} \sum_m |S_{mn}(\mathbf{k})|^2 [\epsilon_n(\mathbf{k}) - \epsilon_m(\mathbf{k})] \quad (2.42)$$

where n and m define the eigenvectors of both layers. In the other layer, the same expression for the shift energy $\delta^S \epsilon_m(\mathbf{k})$ can be obtained from the previous one by inverting n and m . On the other hand, we have the shift due to the hopping, in molecular perturbation theory, given by

$$\delta^T \epsilon_n(\mathbf{k}) = \sum_m \frac{|T_{mn}(\mathbf{k})|^2}{\epsilon_n(\mathbf{k}) - \epsilon_m(\mathbf{k})} \quad (2.43)$$

where $T_{mn}(\mathbf{k})$ is the orthogonal hopping terms given by

$$T_{mn}(\mathbf{k}) = T_{mn}^0(\mathbf{k}) - \frac{1}{2} S_{mn}(\mathbf{k}) [\epsilon_m(\mathbf{k}) - \epsilon_n(\mathbf{k})]. \quad (2.44)$$

Here T^0 is the non orthogonal hopping term and the second term on the right is a correction due to the small overlap S_{nm} between eigenstates in different layers.

The main important terms on the one-electron energy shift are given by the first repulsive terms on the right in eq.2.42 and the attractive δ^T , whereas the S^2 term is almost negligible. An illustration of the behaviour of this terms as a function of the interlayer distance is shown in Fig.2.5, taken from [64] and calculated between two graphene layers.

Finally, summing the two effects, the one-electron contribution has the following expression:

$$E_{one-el} = 2 \sum_{n=occ} (\delta^S \epsilon_n + \delta^T \epsilon_n) + \sum_{m=occ} (\delta^S \epsilon_m + \delta^T \epsilon_m). \quad (2.45)$$

The last part of H_0 Hamiltonian we are going to discuss is the main many-body contributions, except vdW interaction that, as we said, is included in δH . For this term the overlap (S^2) expansion is used again: once we get the orthogonalisation within each layer (yielding $\{\psi_i^0\}$ for the layer 1 and $\{\psi_\alpha^0\}$ for the layer 2) the overlap between different layers is calculated ($S_{i\alpha} = \langle \psi_i^0 | \psi_\alpha^0 \rangle$) by means of eq.2.19, and then the S^2 expansion is performed.

The Hamiltonian related with the many-body contributions includes the interaction between the layers and is composed by many terms. Avoiding the three-center interlayer contribution, the Hamiltonian can be written as following

$$\hat{H}_{int} = H_{one-el} + H_{el-el} + H_{el-ion}. \quad (2.46)$$

The first term is the one electron contribution explained before, written in $\{\psi\}$ orthonormal basis set within the same layer, given by

$$\hat{H}_{one-el} = \sum_{i,\sigma} \hat{n}_{i,\sigma} \delta^S \epsilon_\alpha(\mathbf{k}) + \sum_{\alpha,\sigma} \hat{n}_{\alpha,\sigma} \delta^S \epsilon_i(\mathbf{k}) + \sum (T_{i\alpha} \hat{c}_{i\sigma}^\dagger \hat{c}_{\alpha\sigma} + T_{\alpha i} \hat{c}_{\alpha\sigma}^\dagger \hat{c}_{i\sigma})$$

where i (α) runs through the orbitals of the first (second) layer and the energies ϵ in δ^S (see eq.2.42) and in $T_{i\alpha}$ are approximately the DFT levels for independent layer corrected by the electrostatic potential of the other layer (see [66] for details).

The last term, namely the electron-ion interaction, is composed by the sum of two terms. The first term is

$$\sum_{i,\sigma} \hat{n}_{i,\sigma} V_{ii,\sigma}^{ps,(0)}(2) = \sum_{\gamma} I_{ii,\gamma}^0 = \sum_{\gamma} \langle \psi_i^0 | \frac{-Z_\gamma}{\mathbf{r} - \mathbf{R}_\gamma} | \psi_i^0 \rangle$$

where Z_γ is the pseudonuclear charge in atom γ of the first layer and the sum is extended to all the atoms in the second layer. The second term is the symmetric one, where the pseudopotential Z_k of the second layer appears and the sum runs over the atoms of the first layer.

Finally, the terms in the middle collect all the electron-electron interactions:

$$\hat{H}_{el-el} = \sum_{i,\alpha,\sigma} [J_{i,\alpha}^{(0)} \hat{n}_{i,\sigma} \hat{n}_{i,\bar{\sigma}} + (J_{i,\alpha}^{(0)} - J_{i,\alpha}^{x,(0)} + J_{i,\alpha}^{(0)} S_{i,\alpha}^2) \hat{n}_{i,\sigma} \hat{n}_{i,\sigma}]$$

where $J_{i,\alpha}^{(0)} = (ii|\alpha\alpha)$ and $J_{i,\alpha}^{x,(0)} = (i\alpha|i\alpha)$. The first term on the right gives the Hartree energy, whereas the second and third terms in the parenthesis give the exchange energy coming from exchange integral $J_{i,\alpha}^{x,(0)}$. In the parenthesis we also find the first two terms giving the exchange energy associated with the interaction between charges $n_{\mu,\sigma}$ and their exchange holes $(1 - n_{\mu,\sigma})$. The assumption in this formalism is that this term only depends on the intralayer interactions, being negligible the modification due to S^2 .

To have an idea of the contribution of each term in the interaction energy between the two layers, we report a plot taken from [64] obtained for two graphene layers (see Fig.2.5).

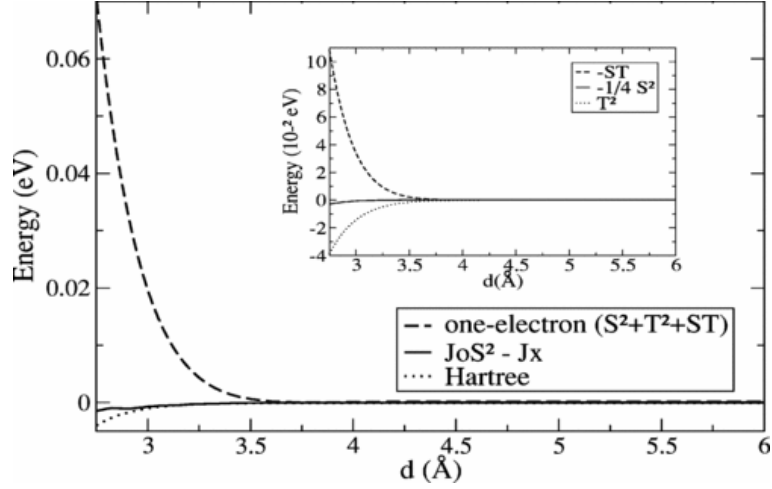


Figure 2.5: One electron, exchange-integral and Hartree contribution to the interaction energy as a function of graphene layers distance. Contribution to the one-electron term are shown in the inset [64].

Finally, we move to the vdW term included in δH . The vdW Hamiltonian is written as following:

$$\hat{H}^{vdW} = \sum_{i,j,\alpha,\beta,\sigma_1,\sigma_2} J_{i,j;\alpha,\beta}^{vdW} \hat{c}_{i,\sigma_1}^\dagger \hat{c}_{j,\sigma_1} \hat{c}_{\alpha,\sigma_2}^\dagger \hat{c}_{\beta,\sigma_2} \quad (2.47)$$

where $J_{i,j;\alpha,\beta}^{vdW} = (ij|\alpha\beta)$, as in eq.2.34. The i, j (α, β) index refers to different orbitals (also $i \neq j$ and $\alpha \neq \beta$) of the first (second) layer. In this picture the atom-atom vdW approximation is used, requiring that the orbitals i and j (α and β) do belong to the same atom within the corresponding layer.

For $J_{i,j;\alpha,\beta}^{vdW}$ calculation, the local atomiclike orbitals $\{\phi\}$ are used and, due to the small overlap between the orbitals of different layers, the classical dipole-dipole approximation is applied. In this picture it is possible to write $J_{i,j;\alpha,\beta}^{vdW}$ as

$$J_{i,j;\alpha,\beta}^{vdW} = \frac{1}{R^3} (\langle i|x|j\rangle \langle \alpha|x'|\beta\rangle + \langle i|y|j\rangle \langle \alpha|y'|\beta\rangle - 2\langle i|z|j\rangle \langle \alpha|z'|\beta\rangle) \quad (2.48)$$

where R is the distance between atoms along the z direction.

The final vdW energy, with the approximation to not take into account the interactions among different sites in the same layer, can be written as

$$E^{vdW} = 4 \sum_{i,j;\alpha,\beta} (J_{i,j;\alpha,\beta}^{vdW})^2 \int \frac{\rho_i(\epsilon_1)\rho_j(\epsilon_2)\rho_\alpha(\epsilon_3)\rho_\beta(\epsilon_4)}{\epsilon_1 - \epsilon_2 + \epsilon_3 - \epsilon_4} d\epsilon_1 d\epsilon_2 d\epsilon_3 d\epsilon_4 \quad (2.49)$$

where $\rho(\epsilon)$ are the local density of states per spin on each orbital, and the integrals in ϵ_1 and ϵ_3 (ϵ_2 and ϵ_4) run through the occupied (unoccupied) states.

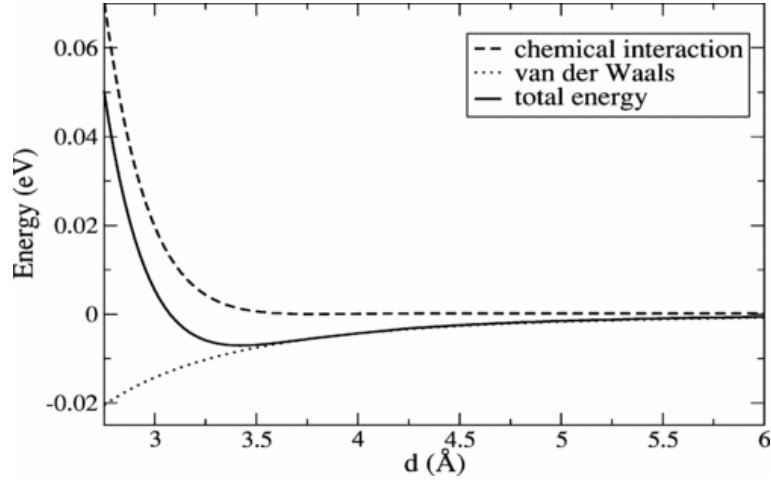


Figure 2.6: Total energy of the system and its main contribution given by the repulsive chemical interaction and the attractive vdW force.

A further simplification of the vdW energy gives the following expression:

$$E^{vdW} = 4 \sum_{i,j;\alpha,\beta} (J_{i,j;\alpha,\beta}^{vdW})^2 \frac{n_i(1-n_j)n_\alpha(1-n_\beta)}{e_i - e_j + e_\alpha - e_\beta} \quad (2.50)$$

where $n_i = \int_{occ} \rho_i(\epsilon) d\epsilon$ are the orbital occupation number, $e_i = \int_{occ} \epsilon \rho_i(\epsilon) d\epsilon$ and $e_j = \int_{unocc} \epsilon \rho_j(\epsilon) d\epsilon$ are the average occupied and unoccupied levels.

It has been found that a minimal basis set, generally used in first-principle calculations for large systems, is not enough to describe properly the vdW interactions because it does not well represent the spectrum of excited states (empty state) that are involved in the vdW calculations. For example it has been found that for graphene the dipole transitions involving $3s$, $3p$ and $3d$ excited atomic orbitals are required for a good description of this interaction [64].

In Fig.2.6 we can find the binding energy between two graphene layers, divided in two main contributions: the repulsive chemical interaction and the vdW attractive energies. Consequently, more than half of the vdW interaction involves virtual transitions, namely transitions with highly excited states (involving d-orbitals for carbon for example). This feature reinforces the fact that DFT cannot intrinsically take into account vdW interactions.

2.5 Transport calculations

In this work we have performed two kinds of transport calculations. One concerns the simulation of the Scanning Tunneling Microscope (STM) images, used to characterize the surfaces of our sample. The other one used in chapter 4 to calculate the tunneling current between the 2D crystals, in particular at the graphene-MoS₂ interface, in order to model a

Field Effect Transistor composed by van der Waals heterostructures. The latter transport calculations concern the detection of defects on MoS₂ monolayer by means of graphene tip STM characterization. All the cited systems are characterized by the non equilibrium state, since a small tension is applied between the two parts involved in the transport calculation.

The theoretical background is in common for all the applications of the electronic transport calculations and is based on the Keldysh-Green formalism, described in the following section.

2.5.1 Keldysh-Green formalism

The nonequilibrium Green's function formalism developed by Keldysh [68] starts from the description of the three parts characterizing the system: the tip, the sample and the interactions between them (see Fig.2.7). In this picture the Hamiltonian can be written as a sum of three terms, one is the Hamiltonian describing the tip, one the sample and H_I is the Hamiltonian of the interaction:

$$\hat{H} = \hat{H}_T + \hat{H}_S + \hat{H}_I. \quad (2.51)$$

The interactions between the two parts (H_I), namely the interaction between the tip (T) and the sample (S) for STM images simulation, or two separated layers in the transport calculation for Field Effect Transistor characterization, is described via hopping process. In particular, the Hamiltonian H_I can be written as the coupling between the orbitals belonging to the two different parts:

$$\hat{H}_I = \sum_{\alpha j} [\hat{T}_{TS}(\alpha j) \hat{c}_T^\dagger(\alpha) \hat{c}_S(j) + \hat{T}_{ST}(j\alpha) \hat{c}_S^\dagger(j) \hat{c}_T(\alpha)] \quad (2.52)$$

where \hat{T}_{TS} and \hat{T}_{ST} are the hopping matrices and $(\hat{c}_T^\dagger, \hat{c}_T, \hat{c}_S^\dagger, \hat{c}_S)$ are creation and annihilation operators associated, where the orbitals α and j are all the orbitals of the tip and the sample, respectively.

The other two terms of the Hamiltonian can be written as $\hat{H}_S = \sum_{\alpha} \epsilon_{\alpha} \hat{n}_{\alpha} + \sum_{\alpha\beta} T_{\alpha\beta} \hat{c}_{\alpha}^{\dagger} \hat{c}_{\beta}$ and $\hat{H}_T = \sum_j \epsilon_j \hat{n}_j + \sum_{ji} T_{ji} \hat{c}_j^{\dagger} \hat{c}_i$.

Now we can write the total current between the two parts as following [69]

$$J = \frac{ie}{\hbar} \sum_{\alpha j} [\hat{T}_{TS}(\alpha j) \langle \hat{c}_T^\dagger(\alpha) \hat{c}_S(j) \rangle - \hat{T}_{ST}(j\alpha) \langle \hat{c}_S^\dagger(j) \hat{c}_T(\alpha) \rangle]. \quad (2.53)$$

We can now substitute the averaged quantities in terms of nonequilibrium Green functions \hat{G}^{+-} , then using the Fourier transformation we can write

$$\langle \hat{c}_T^\dagger(\alpha) \hat{c}_S(j) \rangle = \frac{1}{i} \hat{G}_{T\alpha, S_j}^{+-}(t, t + 0^+) = \frac{q}{2\pi i} \int_{-\infty}^{+\infty} \hat{G}_{T\alpha, S_j}^{+-}(\omega) d\omega, \quad (2.54)$$

the same for $\langle \hat{c}_S^\dagger(j) \hat{c}_T(\alpha) \rangle$ with obvious change of index.

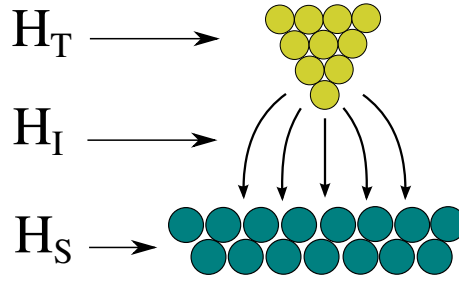


Figure 2.7: Graphic representation of the three parts forming the total hamiltonian given by the tip (H_T), the sample (H_S) and interaction (H_I) interaction.

Using these last expressions, it is possible to write the total current J as a function of the nonequilibrium Green functions as

$$J = \frac{e}{\pi\hbar} \sum_{\alpha j} \int_{-\infty}^{\infty} [\hat{T}_{TS}(\alpha, j) \hat{G}_{Sj, T\alpha}^{+-}(\omega) - \hat{T}_{ST}(j, \alpha) \hat{G}_{T\alpha, Sj}^{+-}(\omega)] d\omega \quad (2.55)$$

and following the trace properties, it becomes

$$J = \frac{e}{\pi\hbar} \int_{-\infty}^{\infty} Tr[\hat{T}_{TS} \hat{G}_{ST}^{+-}(\omega) - \hat{T}_{ST} \hat{G}_{TS}^{+-}(\omega)] d\omega. \quad (2.56)$$

Now we define some quantities we need to write the nonequilibrium Green functions G^{+-} in terms of the retarded and advanced Green functions of the interacting system, G^R and G^A : $\hat{\Sigma}$ is the interaction between the two parts, (in particular $\hat{\Sigma}_{TS} = \hat{T}_{TS}$, $\hat{\Sigma}_{ST} = \hat{T}_{ST}$ and $\hat{\Sigma}_{SS} = \hat{\Sigma}_{TT} = 0$), and \hat{g}^{+-} as the Green's function of the noninteracting case, namely when $\hat{\Sigma} = 0$. We can write the nonequilibrium Green functions as

$$\hat{G}^{+-}(\omega) = [\hat{I} + \hat{G}^R(\omega) \hat{\Sigma}] \hat{g}^{+-}(\omega) [\hat{I} + \hat{\Sigma} \hat{G}^A(\omega)]. \quad (2.57)$$

Moreover, the relation between the Green function of the noninteracting case and the Density of State $\rho_{TT,SS}$ can be written as

$$\hat{g}_{TT}^{+-}(\omega) = 2\pi i \hat{\rho}_{TT}(\omega) f_T(\omega),$$

$$\hat{g}_{SS}^{+-}(\omega) = 2\pi i \hat{\rho}_{SS}(\omega) f_S(\omega),$$

$$\hat{g}_{TS}^{+-}(\omega) = \hat{g}_{ST}^{+-}(\omega) = 0$$

where $f_{T,S}(\omega)$ are the Fermi-Dirac distributions for the two parts. From them we can write the retarded and advanced Green functions for the interacting system:

$$\hat{G}^R = \hat{g}^R + \hat{g}^R \hat{\Sigma} \hat{G}^R, \quad \hat{G}^A = \hat{g}^A + \hat{g}^A \hat{\Sigma} \hat{G}^A.$$

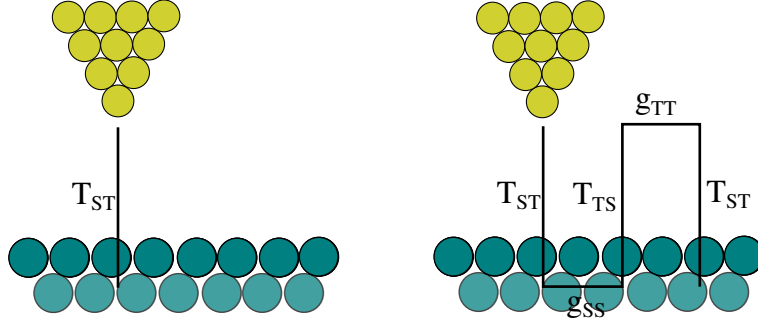


Figure 2.8: Graphic representation of the first term (on the left) and successive terms (on the right) of the hopping describing the multiple scattering effects.

We can now write the total current as a function of the Green function for the uncoupled parts and the hopping matrix that couples both parts of the systems:

$$J = \frac{4\pi e}{\hbar} \int_{-\infty}^{\infty} Tr[\hat{T}_{TS}\hat{\rho}_{SS}(\omega)\hat{D}_{SS}^R(\omega)\hat{T}_{ST}\hat{\rho}_{TT}(\omega)\hat{D}_{TT}^A(\omega)][f_T(\omega) - f_S(\omega)]d\omega \quad (2.58)$$

where

$$\begin{aligned} \hat{D}_{SS}^R(\omega) &= [\hat{I} - \hat{T}_{ST}\hat{g}_{TT}^R(\omega)\hat{T}_{TS}\hat{g}_{SS}^R(\omega)]^{-1} \\ \hat{D}_{TT}^A(\omega) &= [\hat{I} - \hat{T}_{TS}\hat{g}_{SS}^A(\omega)\hat{T}_{ST}\hat{g}_{TT}^A(\omega)]^{-1}. \end{aligned}$$

These two quantities take into account the multiple scattering effects via the summation up to infinity order of an expansion on the scattering matrices given by $\hat{X}^A = \hat{T}_{TS}\hat{g}_{SS}^A(\omega)\hat{T}_{ST}\hat{g}_{TT}^A(\omega)$ and $\hat{X}^R = \hat{T}_{ST}\hat{g}_{TT}^R(\omega)\hat{T}_{TS}\hat{g}_{SS}^R(\omega)$, responsible for the saturation of the tunneling current when the distance between the two parts becomes small [70], see Fig.2.8.

The equation 2.58 includes temperature effect via the Fermi-Dirac function. The trace of a multiplication of several matrices in the eq.2.58 can be physically interpreted as a coherent superposition of different channels. Moreover, in the Tersoff-Hamann limit, namely for large distances between the two parts, the terms $\hat{D}_{TT}^A(\omega)$ and $\hat{D}_{SS}^R(\omega)$ can be approximated with the identity matrix and the current can be written as

$$J \sim \frac{4\pi e}{\hbar} \int_{-\infty}^{\infty} Tr[\hat{T}_{TS}\hat{\rho}_{SS}(\omega)\hat{T}_{ST}\hat{\rho}_{TT}(\omega)[f_T(\omega) - f_S(\omega)]]d\omega$$

. This approximation is valid when \hat{T}_{TS} is small compared with the hopping interaction in the sample. Finally, when the voltage is low enough, namely in the linear response regime and at $T = 0K$, another simplification can be done and the Tersoff-Hamann expression is recovered:

$$J \sim \frac{4\pi e^2 V}{\hbar} Tr[\hat{T}_{TS}\hat{\rho}_{SS}(E_F)\hat{T}_{ST}\hat{\rho}_{TT}(E_F + eV)] \quad (2.59)$$

where V is the applied voltage and E_F is the Fermi level of the sample.

Finally, we can write the relation between the Green function, density of state and hamiltonian [71]:

$$G_{SS}^{a,r}(E) = \lim_{\eta \rightarrow 0} \frac{1}{(E \pm i\eta - H_S)} \quad (2.60)$$

$$DOS_{SS}(\mathbf{r}, E) = \rho_{SS}(\mathbf{r}, E) = \pm \frac{1}{\pi} \text{Im}\{G^{r,a}(\mathbf{r}, \mathbf{r}, E)\} \quad (2.61)$$

where H_S is the hamiltonian of one of the part. The parameter η is a mathematical tool able to avoid the zero at the denominator and takes into account the enlargement of the levels: in this picture, the temperature effect in the experiments is considered. A large value of η can be not good in the determination of the gap in a semiconductor, whereas a small η gives high and thin peaks, making impossible the integration with energy steps larger than η . It is clear that a connection between η and the step of integration exists and has to be considered.

In the next section we will show the application of this formalism in our work: the STM images and the electron transport at graphene-MoS₂ interface calculation.

2.5.2 Application of the Keldysh-Green formalism

Scanning Tunneling Microscope images simulation

A Scanning Tunneling Microscope (STM) represents a powerful experimental technique to investigate the structural and electronic properties of surfaces. Since its invention in 1982 [72, 73] STM represents a revolution for the investigation of surfaces and low dimensional systems. Exploiting the tunnel effect between an extremely sharp tip and the sample separated by 5 to 10Å, the collected current will be proportional to the filled, or empty, states at the surface, depending on the applied bias. The result will be a real space current intensity map with atomic scale resolution. A pictorial diagram of the experimental set up is reported in Fig.2.9.

In the case of STM images calculations, the two parts forming the system are represented by the tip and the sample. The tip is supposed to be very thin, ending with a single atom in order to get an atomic resolution of the sample surface. A voltage between tip and sample leads to an electric tunneling current between them, thanks to the tunnel effect. The current will be given by electrons (occupied states) or holes (empty states) from the tip to the sample, depending on the sign of the applied voltage. The STM images can be performed in two different ways: constant current or constant height. The first type of measurements gives a direct information on the corrugation of the surface and can be realized by fixing the current and let the tip move vertically (perpendicular direction to the sample surface); in the second case, the constant height gives different current values, depending on the local electronic distribution on the surface.

In our calculations, due to the temperature $T = 0$ K and in the case of small voltages $V \simeq 0$, the current is calculated using equation 2.59.

The tip in a STM model can be treated in different ways. A simple approach is to consider

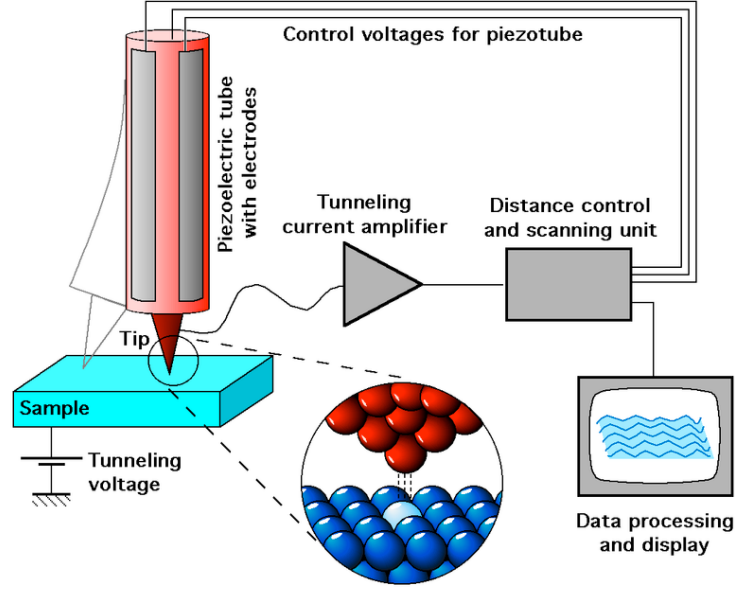


Figure 2.9: Scheme of Scanning Tunneling Microscope.

the tip as an orbital with spherical s-symmetry. However, in this way, it is obviously not possible to have informations about the kind of tip used in the experiments. In order to simulate an accurate STM image, it is necessary to consider and model the chemical properties of the atom forming the apex. One method to do that is to consider a cluster formed by a pyramid of 4 or 5 atoms coupled with a system that simulates a volume. In Fireball, the tip is built as a cluster of 4 or 5 atoms attached to a surface of the same material of the cluster, or, like in our calculations, as a pyramid composed by 35 atoms. The Green function related to the tip is given by:

$$g_{TT}^{r,a}(E) = \frac{1}{(E \pm i\eta)\hat{I} - \hat{H}_C^{eff} - \hat{\Sigma}_B^{r,a}(E)} \quad (2.62)$$

where \hat{H}_C^{eff} is the hamiltonian of the cluster of 4 or 5 isolated atoms, whereas $\hat{\Sigma}_B^{r,a}(E)$ is the self-energy matrix resulting from the coupling between the surface and the cluster. In this model, the hopping between the two parts is pre-calculated considering first the interactions between the dimers formed by one atom of the tip and one atom of the sample. This is repeated for all the combinations of atomic pairs and for a certain numbers of distances. All the calculated hoppings are stored and used by means of interpolations during the STM simulations. One of the first approximations of the interaction between tip and sample is the Bardeen approximation where the hopping is calculated as follows:

$$T_{ST}(\alpha, j) = \frac{\gamma}{2} \int_{\sigma_{T,S}} dS (\psi_T^*(\alpha) \nabla \psi_S(i) - \psi_S^*(i) \nabla \psi_T(\alpha)) \quad (2.63)$$

where γ is a semiempirical parameter with a range of values from 1.3 to 1.5, $\psi_T(\alpha)$ and $\psi_S(i)$ are the orbitals of atomic pairs of the tip and the sample. In this expression, the

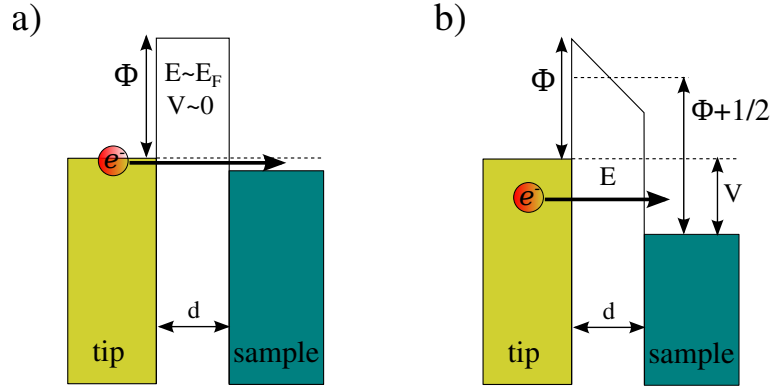


Figure 2.10: Scheme of barrier voltage for voltages $V \sim 0V$ in a) and for finite voltages in b).

integral is calculated on the surface σ respecting the following condition:

$$\int_{\Omega_S} \psi_S \psi_T d^3r = \int_{\Omega_T} \psi_S \psi_T d^3r.$$

In Fireball, the hoppings are calculated by going beyond the Bardeen approximation, introducing more contributions in the calculations. The first problem is the large distance : starting from a given distance, the hoppings reveal a non-homogeneous shape, responsible for the edge effects in the STM images. To solve this problem, the approximation of parallel planes is used, coming from the fact that at large distances the cluster attached to the surface and the surface itself can be approximated by a plane. It means that in this approximation the probability to tunnel through the barrier is given by:

$$P \propto e^{-2 \int_0^d \sqrt{2(U(z)-E)} dz} \cong e^{-2d\sqrt{2\phi}}$$

where $U = \phi$ for $0 < z < d$, and $V \simeq 0$.

The factor $e^{-2d\sqrt{2\phi}}$ is the probability of an electron to cross the barrier given by ϕ for small voltages V . The total probability amplitude can be written as

$$T_{Total} \propto e^{-z\sqrt{r\phi}}$$

where z is the tip-sample distance.

Thus, the hopping between each pair of orbitals of belonging on the tip and the sample follows the same exponential relation

$$T \propto f(z)e^{-z\sqrt{2\phi}}$$

where $f(z)$ is a smooth function such as the sum of T for all the pairs gives T_{Total} . Within the approximation related to large distances, the total probability can be approximated as

$$T_{Total} \propto f(d)e^{-d\sqrt{2\phi}}$$

and comparing that with the expression of T_{Total} written before we can conclude that

$$T \propto \frac{1}{d} e^{-d\sqrt{2\phi}}$$

valid for free electrons with bands similar to s orbitals. Finally, the expression for all the orbitals given by Harrison [74] is

$$T \propto \frac{1}{d^\alpha} e^{-d\sqrt{2\phi}} \quad (2.64)$$

where $\alpha = l_1 + l_2 + 1$, with l_1 and l_2 are the quantum number of each orbital of the pair of atoms. The constant we need to completely define the hopping expression is determined by connecting it with the expression given by the Bardeen approach. In the point where the change from one to the other occurs, the value of the two functions and their derivative is required to be equal.

So far, we have studied the case of small voltages where the electrons close to the Fermi level (namely with energy in the range $[E_F; E_F + eV]$) have the same probability to tunnel. On the other hand, for larger voltages, we want that the electrons close to the Fermi level have more probability to tunnel than the electrons in the lowest levels since the latter feel a larger barrier. Starting from the WBK approximation, we can approximate the triangular barrier as a rectangular one with high $\psi = \phi + \frac{1}{2}V$ (see Fig.2.10). In this case, the probability to tunnel from one side to the other is given by

$$T \propto e^{2d\sqrt{2(\psi-E)}}$$

and, since the work function ϕ is large compared to V , we can approximate the exponential part as follows:

$$T \propto e^{-2d\sqrt{2(\phi+\frac{1}{2}eV-E)}} \approx e^{-2d\sqrt{2\phi}} e^{\frac{2d}{\sqrt{2\phi}}(e-\frac{1}{2}eV)}$$

where $e^{-2d\sqrt{2\phi}}$ corresponds to the hopping related to the large distances.

The new equation for the current is, then, given by:

$$J = \frac{4\pi e}{\hbar} \int_0^{eV} Tr[T_{TS}\rho_{SS}(E)T_{ST}\rho_{TT}(E - eV)] e^{\frac{1}{\Delta E}(E-\frac{1}{2}eV)} dE \quad (2.65)$$

where $\Delta E = \sqrt{2\phi}/2d$. Here, as we required, the electrons with energy close to Fermi have the maximum probability to tunnel and that with energy $\frac{1}{2}V$ have the same probability as for small voltages.

Electronic Transport at graphene-MoS₂ interface

The same formalism is used to calculate the electronic transport at the graphene-MoS₂ interface. The difference is that in that case, the tip is given by one of the two planes (generally, the graphene layer) and all the parts related to the characterization of the tip are not present here. In particular, here the tip is composed by an extended plane of

C atoms forming the graphene plane (or Mo and S atoms, for the MoS₂ plane), or, in other words, we can imagine that each C atom is a tip. The hopping terms are calculated between all the atoms of graphene coupled with each atom of MoS₂. In this case we have not considered the approximation for large distances: here, for each C atoms we have close and far S and Mo atoms, meaning that the hoppings between one C atom and a sulfur atom, we call for simplicity S', far away is negligible with respect to the hopping between S' and the closer C atoms.

2.6 Summary

In this chapter we have detailed the theory and methods used in this work of thesis. The Density Functional Theory is at the basis of this work, allowing the calculation of the optimized atomic configurations and the electronic properties by mean of Density of State and electronic band structure. In the framework of Van de Waals heterostructures, the LCAO-S²+vdW formalism implemented in fireball code, allows us to take into account the Van der Waals forces, normally missed in the standard DFT, and to calculate the attractive interaction between the planes and the interplane equilibrium distance in graphene/MoS₂ and in other studied interfaces. The electronic transport calculations are based on the Keldysh-Green formalism that uses the occupation number provided by previous DFT calculations. It is used in both the Scanning Tunneling Microscope images simulations and for the analysis and comparison of graphene and copper AFM tip in chapter 5. In the study of the transistor formed by Van der Waals heterostructure shown in chapter 4, the scissor operator is used to simulate the gate voltage potential, leading to a shift of the band structure. Then, once the charges are calculated in DFT for each band alignment, the same Keldish-Green formalism allows us to calculate the transverse current at the interface, used to characterize the performance of the transistor model.

Chapter 3

Graphene/TMDC heterostructure

In this chapter we will present our study on graphene/MoS₂ heterostructure, in particular we focus on the influence of the orientation between the MoS₂ and graphene planes on the structural and electronic properties.

We first introduce separately both free-standing graphene and MoS₂ monolayers, then we discuss their structural and electronic properties, at the equilibrium and under positive and negative strains.

The second part is related to graphene/MoS₂ stacking: after pointing out the computational challenge related to the lattice mismatch and the periodic boundary conditions in the building of the supercells, we discuss the role of the rotation angle between graphene and MoS₂ on the global and local electronic properties.

A comparison with the experimental results (provided by the collaborators of Centre de Nanosciences et de Nanotechnologies, CNRS and Université Paris-Sud, Université Paris-Saclay and the Department of Physics and Astronomy, from University of Pennsylvania) is given and the role of the dangling bonds at the edges of MoS₂ flake on its structure is considered.

This chapter ends with the study of a more complex heterostructure composed by MoSe₂, another TMDC similar to MoS₂ also presented in the first part, on few-layer graphene deposited on SiC substrate. Here, our theoretical calculations support the experimental results provided by the group of CEA Grenoble by stressing the presence of an interplane interaction able to tune the electronic properties of the graphene planes.

In other words, in this chapter we perform an extensive study of the interactions in graphene/TMDC heterostructure: we start by a theoretical investigation of the van der Waals forces at the infinite interface, then we go further by including two other contributions, as the edges effect on the 2D flake and the interaction with the substrate.

3.1 Graphene: the first 2D material

As we already know, graphene was the first bidimensional material to be isolated ever. It is a single layer of graphite (Fig.3.1), namely composed by one plane of carbon atoms

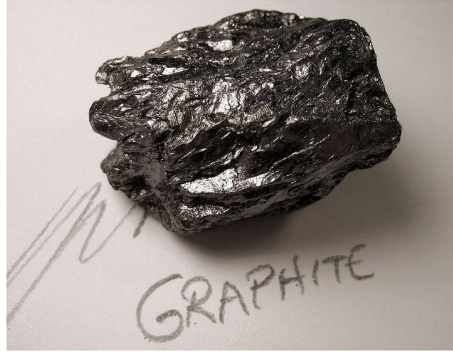


Figure 3.1: Image of a piece of graphite from the web ([75]).

organized in a honeycomb structure.

The in-plane stability of graphene, explained by the absence of dangling bond at the surface, together with the weak van der Waals interaction between the planes in graphite, allowed Novoselov *et al.* [1] to isolate a single graphene layer from graphite by means of mechanical exfoliation.

Due to its peculiar structure, graphene presents many surprising properties like a record stiffness (0.5 TPa), impermeability to gases, and low resistivity of $\sim 10^{-6}\Omega cm$. Furthermore, its high mobility makes graphene in a first line in the electronic devices with low dimension characteristics. However, its unique electronic structure that classifies it as a zero gap material, or semimetal, limits its applications to logic circuits for low-power switching. Many efforts have been done to open a gap on graphene, with the results to affect, at the same time, its fantastic properties. We know that one way to overcome this problem is to combine the mobility of graphene with the gap of a 2D semiconductor by means of heterostructures, since thanks to the van der Waals interaction, each layer can keep its main electronic properties.

Structural and electronic properties

Graphene is characterized by a honeycomb structure. Since it does not belong to the Bravais lattices, it can be described as a double shifted hexagonal lattice with 2 equivalent C atoms (black balls in the inset of Fig.3.2) forming the basis. The primitive cell is represented by the dashed lines and the lattice vectors by the arrow \mathbf{a}_1 or \mathbf{a}_2 in Fig.3.2a.

The in-plane lattice constant is $a \simeq 2.48 \text{ \AA}$ and the lattice vectors in Cartesian coordinates are

$$\mathbf{a}_1 = a \left(\frac{1}{2}, \frac{\sqrt{3}}{2} \right) \quad ; \quad \mathbf{a}_2 = a \left(-\frac{1}{2}, \frac{\sqrt{3}}{2} \right). \quad (3.1)$$

The lattice vectors of its hexagonal Brillouin Zone (BZ), defined as primitive cell in the reciprocal lattice (Fig.3.2b), are given by

$$\mathbf{b}_1 = \frac{2\pi}{\sqrt{3}a} (1, \sqrt{3}) \quad ; \quad \mathbf{b}_2 = \frac{2\pi}{\sqrt{3}a} (1, -\sqrt{3}). \quad (3.2)$$

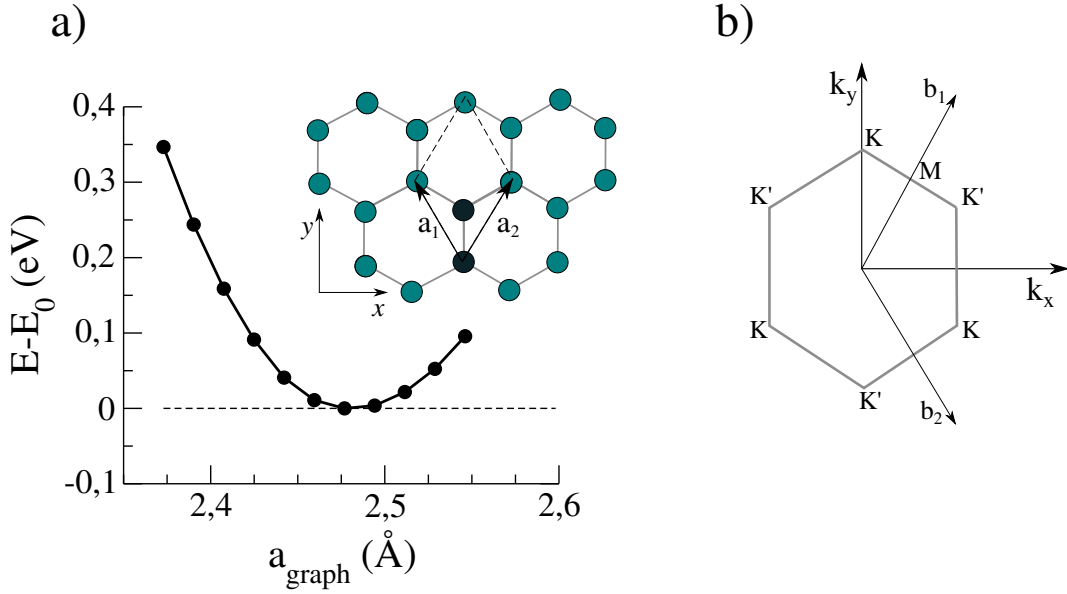


Figure 3.2: Plot of total energy as a function of lattice parameter in a) and representation of the lattice parameter in hexagonal structures in the inset. In b) the Brillouin zone and the reciprocal lattice vectors are shown.

This peculiar geometry, due to the sp^2 hybridization of carbon atoms, produces strong σ in-plane orbitals and unpaired π states. The π states are at the origin of the exceptional properties of graphene like linear dispersion of electronic bands (Dirac bands) around the K points of BZ (see Fig.3.3) left panel, with a zero-dimensional Fermi surface (FS) constituted by a single point (Dirac point). This means that electrons have photons-like energy dispersion with zero mass exhibiting extraordinary transport properties (described by a Dirac-like equation) [76]. Due to this peculiar band structure, characterized by linear dispersion, it exhibits giant mobility and electrons can travel for micrometers without scattering at room temperature. The corresponding resistivity is less than the resistivity of silver and it can sustain current densities $\sim 10^6$ times higher than the one of copper [77, 78].

According to the used code and the chosen parameters, we can find slightly different equilibrium lattice vectors for the same crystals. For this reason, once the pseudopotential and the atomic orbital radius in Fireball have been chosen, we evaluated the equilibrium structural parameter by comparing the total energies as a function of different values of $a = a_1 = a_2$. In this work, we have characterized the graphene layer by considering 2 electrons on s and 2 electrons on p orbitals with cut-off radii $r_s = r_p = 4.5$ a.u.; a mesh of 2018 k -points in the BZ for the electronic structure calculations was used.

In the case of graphene, the only parameter that can completely describe the structure is the in-plane lattice vector, while the distance between the C atoms of the same basis is given by $d_{C-C} = \frac{1}{\sqrt{3}} a$.

About the structural optimization, we have built different primitive cells 1×1 characterized by different in-plane dimensions. Since graphene has a bidimensional structure,

the out of plane dimension is kept at 99.0 Å to simulate an isolated freestanding layer. Finally, we performed the relaxation of the d_{C-C} internal coordinate. The value of the total energies for each cell is shown in fig.3.2: the equilibrium is found to be $a = 2.48$ Å in good agreement with the values in literature, given by $a = 2.46$ in [79].

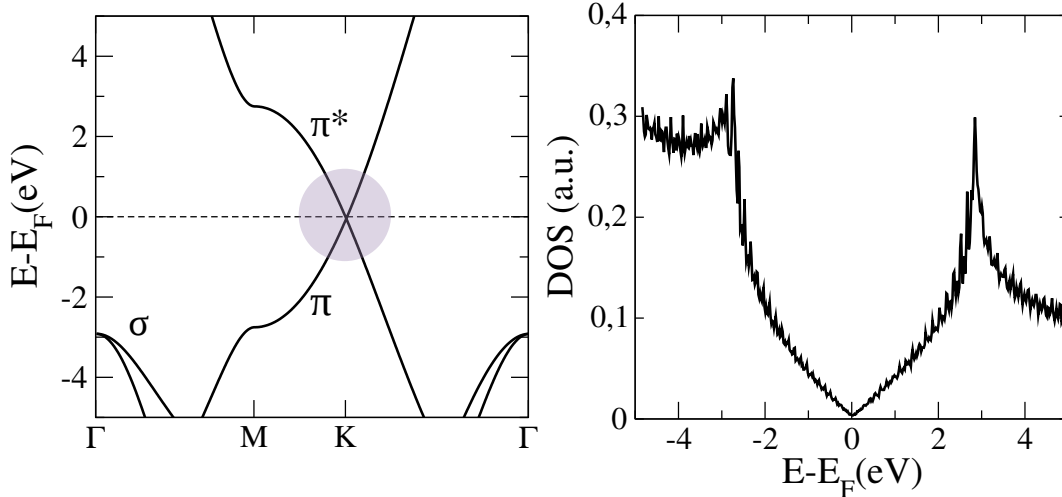


Figure 3.3: Calculated Band Structure with the Dirac point in the circle and Density of State of free-standing graphene, using the Fireball code.

The electronic properties, namely the calculated Density of State (DOS) and band structure (BS) are shown in Fig.3.3. The main features of graphene is the well known Dirac cone at the K point: the linear dispersion between a range of -2V and +2V forms two cones with the common vertex on the Fermi level. For that peculiar shape of the BS, graphene is classified as a semimetal, namely a metal (bands crossing the Fermi level) with a zero DOS at Fermi. Or, if we look at the Fermi Surface (FS), represented by the intersection point of the conduction and valence band, graphene can be defined also as a zero gap material. The linear behaviour is clearly represented in the DOS in Fig.3.3.

Strain effect on graphene electronics

In this work, the study of the uniform biaxial tensile strain effects on the electronic properties of a single crystal is strictly necessary in order to approach the problem related with the building of the supercells, fully described in Section 3.3.1.

For the moment, we focus on the strain effects on graphene. In order to reproduce the uniform biaxial tensile strain effect, we considered a standard (1×1) unit cell optimized for different lattice parameters around the equilibrium. For each value of lattice parameter, the band structures have been calculated and compared in Fig.3.4. As we can see around the K point of the BZ, the linear dispersion still characterizes the graphene electronics, except for a slight change of slope that does not bring any important undesirable contribution or problem in our work.

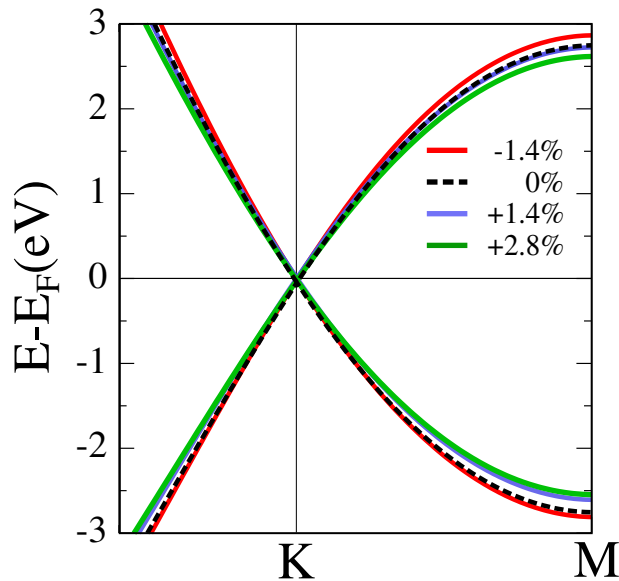


Figure 3.4: Graphene band structure around the Dirac cone for different applied strain.

3.2 MoS₂ monolayer: a 2D direct gap semiconductor

Monolayer molybdenum disulfide (MoS₂) is a graphene-like material, one of the most studied of the group of transition metal di-chalcogenide (TMDC). Together with graphite and hBN (hexagonal Boron Nitride), it was widely used as lubricant at first. MoS₂ is also mechanically flexible with a Young's modulus of 0.33 TPa, that makes possible to use it for transparent and flexible electronic devices as Field Effect Transistors [80]. The same kind of mechanical exfoliation with scotch tape can be used to isolate a single MoS₂ flake from the bulk (an image of a piece of MoS₂ is provided Fig.3.5). In the last years, thanks to its physical properties, it has an important role in device applications, in particular combined with graphene [81].



Figure 3.5: Image of a small piece of MoS₂, taken from the web [82].

The main interest in MoS₂ monolayer comes from its electronic properties: a direct gap of ~ 1.8 eV at the K point in the Brillouin zone, classifies this material as a direct gap semiconductor. It is interesting also to notice the layer dependence of the band structure,

and in particular of the gap: direct in monolayer phase, indirect from bilayer to bulk.

Structural and electronic properties

More complex in its structure, MoS₂ monolayer is composed by two sulfur atoms plane separated by a molybdenum plane. In the single layer of MoS₂ films, Mo (+4) and S (-2) are arranged to a sandwich structure by covalent bonds in a sequence of S-Mo-S planes (Fig3.6a on top). From an in-plane view (Fig3.6a on bottom), MoS₂ presents a honeycomb structure, with the basis composed by 3 atoms, S-Mo-S.

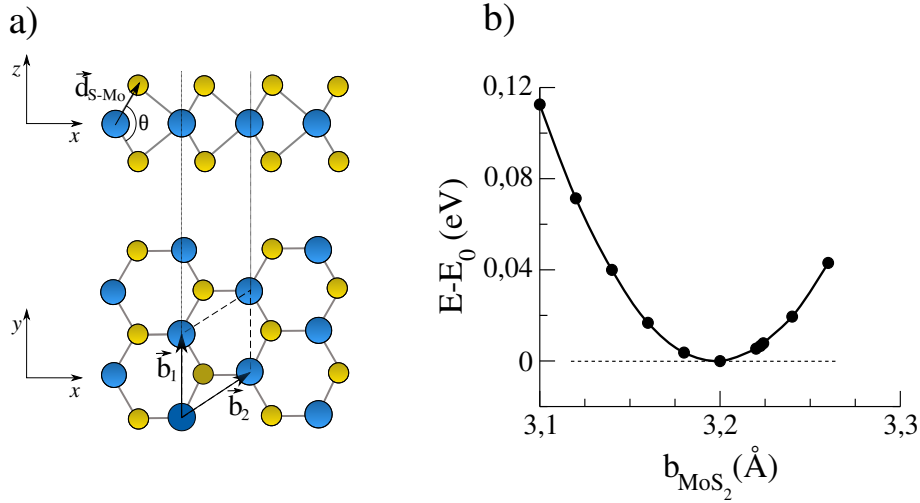


Figure 3.6: In a) the crystal structure of MoS₂ from lateral and top view (on the top and bottom, respectively) with lattice vectors $\mathbf{b}_{1,2}$; in the lateral view other two parameters defining the structure, θ and d_{S-Mo} , are shown. The blue (yellow) circles represent Mo (S) atoms. In b) the energetic curve giving the equilibrium lattice parameter.

The parameters describing its structure are represented in Fig3.6a: \mathbf{b}_1 and \mathbf{b}_2 (equivalent to \mathbf{a}_1 and \mathbf{a}_2 in graphene) define the in-plane structure, whereas $d_{S-Mo} = 2.44$ Å and the angle $\theta = 81.8$ deg, defining the S-Mo-S bond, describe the out of plane atomic arrangement. As in the graphene case, the optimization has been done by changing the in-plane lattice vector of the unit cell, while the two out of plane parameters change according to the in-plane one. Furthermore, the out of plane dimension of the unit cell will be fixed to 99.0 Å, as in graphene, to simulate an isolated free standing MoS₂ layer. For MoS₂ we used the following DFT parameters: for Sulfur (Molybdenum) we have 2, 4 and 0 (1, 0 and 5) e^- in s , p and d orbitals respectively with the following radius $r_s = 3.9$ a.u., $r_p = 4.5$ a.u., $r_d = 5.0$ a.u. ($r_s = 5.0$ a.u., $r_p = 4.5$ a.u., $r_d = 4.8$ a.u.). As we can see in Fig.3.6b, the calculated equilibrium lattice parameter is $b = b_1 = b_2 = 3.20$ Å, slightly larger than the experimental lattice parameter ($b=3.15$ Å in [83]) but still in good agreement.

The main electronic characteristic of MoS₂ is represented by the electronic gap of ~ 1.83 eV in the monolayer phase (see Fig.3.7). Here, the maximum of valence band (VB)

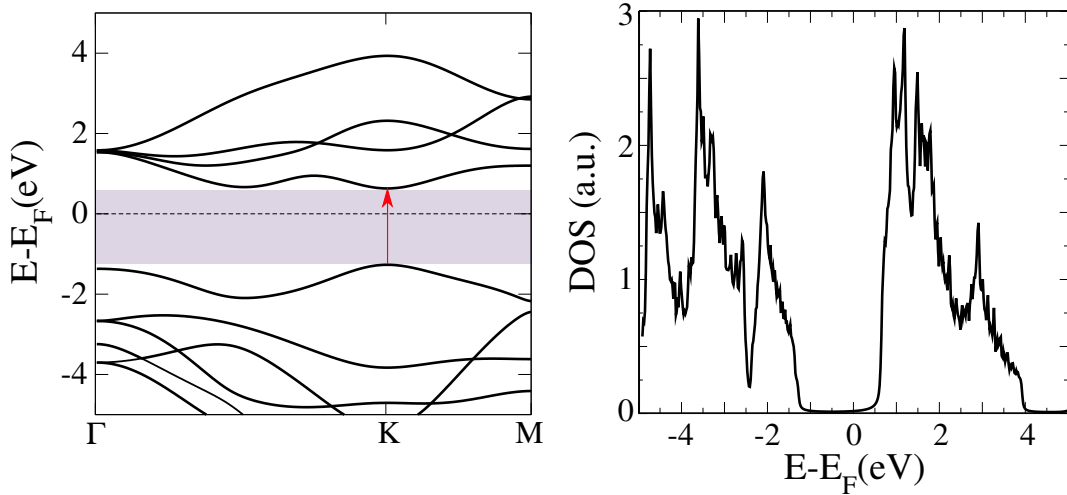


Figure 3.7: Calculated band structure and Density of State of free-standing monolayer MoS₂ using the Fireball code. The direct gap is indicated with the vertical arrow in K.

and the minimum of conduction band (CB) fall in K, revealing an important direct gap largely used in optics, solar cells etc. [84, 85].

The direct gap disappears once the second layer is added and so on until the bulk phase: here, the relative maximum of the VB in Γ increases and overcomes the one in K, while the minimum of CB falls in the middle point between K and Γ .

Strain effect on MoS₂ electronics

More than in graphene, a small uniform biaxial tensile strain on MoS₂ can strongly affect the electronic properties, in particular the electronic gap. The same procedure we described in graphene section has been used to study the strain effect on MoS₂. Here, once we fix the value of lattice parameters, the system will find the equilibrium by changing both the angle θ and d_{S-Mo} .

The tunability of the bandstructure of MoS₂ by varying the strain was one of our first published results in Ref.[86] in collaboration with the experimental group of Abdelkarim Ouerghi at the C2N, that we will present in the following.

The main feature observed here, in agreement with experimental observations, is related to the effect of positive strain on the gap type of MoS₂. Starting from the equilibrium BS in Fig.3.8 (black dashed lines) and moving to positive strain values, namely increasing the lattice parameter, the relative maximum of the valence band (VB) in Γ increases. Already at 0.6% (green lines), we can see the maximum of VB almost falling in Γ , whereas the minimum of conduction band (CB) is still in K. It reveals the important change of the gap type from direct to indirect for very small strain rate. Moreover, as the strain increases, the gap value is going to reduce. A strong evolution of the BS is also observed by applying a negative strain: at -0.6% rate the gap is already indirect, in this case from K in the VB to middle point between Γ and K in the CB, with a reduction of ~ 0.1 eV of the gap value.

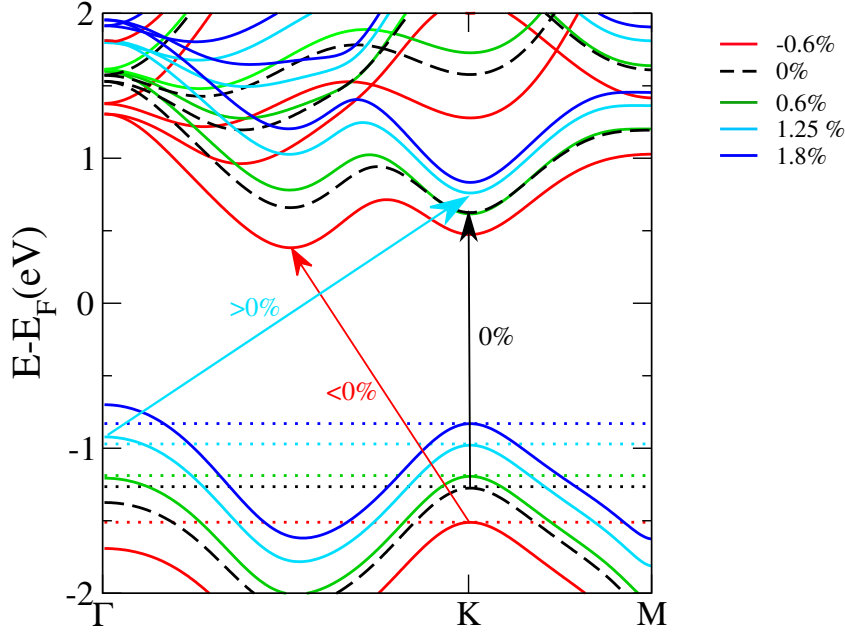


Figure 3.8: MoS₂ band structure for different compression rates showing the change from direct to indirect gap. The black dashed lines represent the optimized phase. The arrows underline the band gap type: direct for optimized structure (black arrow), indirect for positive (light blue) and negative (red) strain.

Therefore, we have shown here that, contrary to graphene, a small change in the structure of MoS₂ given by an applied strain, for instance, can induce an important modification of the electronic properties, namely the evolution from direct to indirect gap. This result has been taken into account in the building of the supercells of MoS₂/graphene heterostructures, as we will fully explain in section 3.3.1.

MoSe₂, another Transition Metal Dicalchogenide

In this short section we will introduce a second TMDC, the Molybdenum diselenide (MoSe₂), that we will consider at the end of this chapter. MoSe₂ is very similar to MoS₂, from both the structural and electronic points of view (see Fig.3.9). In fact, the atomic structure is the same as in the MoS₂, however, since Se is bigger than S, the lattice parameter of MoSe₂ is larger than the lattice parameter of MoS₂.

Using the same procedure, namely by comparing the total energy for different sizes of the unit cell as previously, the lattice vector of MoSe₂ is calculated to be $a = 3.32 \text{ \AA}$.

Regarding the electronic characteristics, we can briefly say that MoSe₂ is also a semiconductor with direct gap (of $\sim 1.8 \text{ eV}$) at the K of the Brillouin zone. The BS and the DOS are represented in Fig.3.9b and Fig.3.9c.

In this case, we will not investigate the impact of the applied isotropic strain on the MoSe₂ electronics. In fact, in the investigation concerning the interlayer interaction beyond vdW between few-layer graphene, SiC substrate and MoSe₂ itself, the strain effect on MoSe₂ is

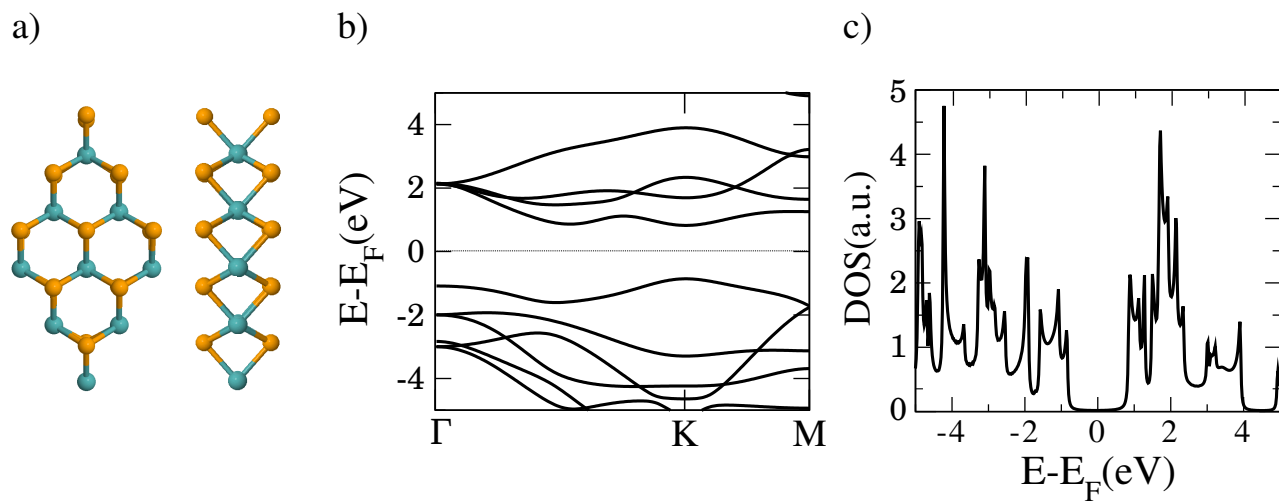


Figure 3.9: In a) the atomic structure is shown, with orange and blue circles for Se and Mo atoms, respectively. The BS and DOS of isolated MoSe₂ are represented in the b) and c) panel.

not crucial.

3.3 Graphene/MoS₂: different properties for different orientations?

In the next sections we will analyze graphene/MoS₂ interface focusing the attention on the role of specific rotation angles between the layers on the properties of graphene, MoS₂ and the whole heterostructure [15]. So far, the interaction between graphene and MoS₂ seems not to be clear yet, since several theoretical and experimental papers exhibit specific modification of graphene and MoS₂ electronic properties, according to specific rotation angles between the layers.

This topic has been already treated in some previous theoretical and experimental works [16, 17, 87, 88]: the possibility to tune the electronic features of 2D crystals in a controlled way by means of different techniques is a fascinating research area from the point of view of the fundamental physics and in nanoelectronic applications as well.

From a theoretical point of view, DFT calculations require the building of a superstructure, namely a supercell that is at the same time a multiple of MoS₂ and graphene unit cell, repeated in the whole space by means of the periodic boundary conditions. In most of the cases, due to the lattice mismatch, the choice of the supercell is a compromise between the reasonable dimension and the artificial strain on the component materials necessary to compensate the mismatch. Moreover, as demonstrated in the previous sections, the strain on MoS₂ can have an important effect on the electronic properties, especially affecting the value and type of the energy band gap [89].

In the following section, we consider different rotation angles between graphene and MoS₂, in order to elucidate the mutual influence between two monolayers. We first discuss the structural aspects of the graphene/MoS₂ interfaces, namely the unit cells for DFT calculations considered for the different rotation angles and the corresponding interaction energies. Then we analyze the electronic band structures and Density of States, and finally we present Scanning Tunneling Microscopy (STM) images calculations which exhibit different patterns, called Moiré patterns, for the different structures [86].

3.3.1 Lattice mismatch problem: building the supercells

The study of interfaces, involving two crystals with different lattice parameters, as in the case of graphene/MoS₂, leads to a well known problem in DFT calculations: the design of the supercell. In fact, due to the imposed periodic boundary conditions required to reproduce an infinite interface, a superstructure with specific basis of lattice vectors has to be found [90]; the basis of lattice vectors has to be commensurated with both the graphene and MoS₂ parameters. However, a perfect matching of the two structures is not obvious, and sometimes it can be obtained for very big supercells, making DFT calculations impractical. As a consequence, the matching of the two structures in the new superstructure can be obtained inducing necessarily a small error in the optimization process. It means that, on the way we choose the supercell, the structures relax differently, which induces an artificial strain on MoS₂, on graphene, or on both, depending on the cases.

This argument is valid for any rotation angle. In principle, to each angle corresponds a different matching and, consequently, a different strain on the 2D crystals.

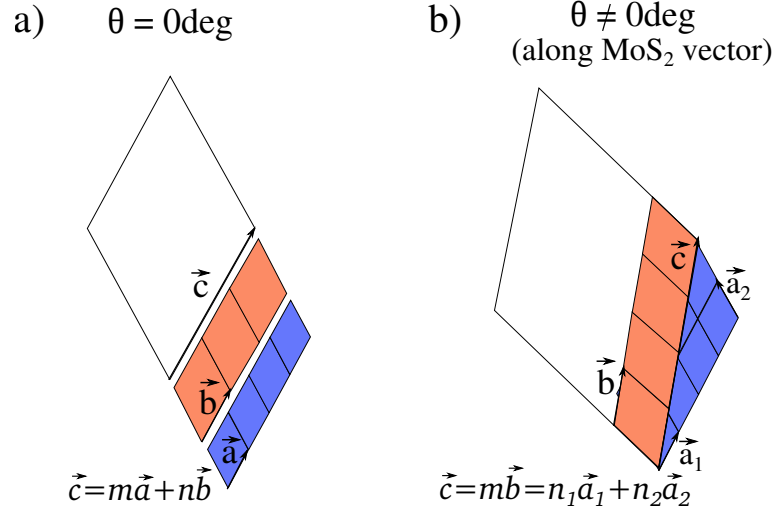


Figure 3.10: Representation of the supercells for $\theta = 0$ deg in a) where a , b and c are parallel and $m(n)=3(4)$. In b) we consider the case of a generic $\theta \neq 0$ deg: c is aligned with b for an optimization in MoS₂ lattice vector. White rhombus defined by \mathbf{c} represent the supercells, whereas the small red (blue) rhombus represent the MoS₂ (graphene) 1x1 cell. It is necessary that an integer number of red and blue small rhombus fits in the supercell.

In the simplest case, when the angle $\theta = 0$ deg, the lattice vectors of supercell (\mathbf{c}), of graphene (\mathbf{a}) and MoS₂ (\mathbf{b}) are parallel (see Fig.3.10a), and they satisfy the following relation:

$$c = na = mb,$$

where n and m are integer numbers. In this case, if we want to avoid the strain on MoS₂ we will choose c to be exactly a multiple of b ; however, due to the mismatch between MoS₂ and graphene of 28%, c will not be at the same time an exact multiple of a , causing an artificial strain on graphene.

If $\theta \neq 0$, we can choose \mathbf{c} being parallel to \mathbf{b} (\mathbf{a}) and forming an angle defined by θ with \mathbf{a} (\mathbf{b}). Depending on the crystal we want to keep at the equilibrium, for example MoS₂ (graphene), \mathbf{c} will be chosen parallel to \mathbf{b} (\mathbf{a}). Consequently, \mathbf{c} will be an exact multiple of \mathbf{b} , and at the same time a linear combination of \mathbf{a}_1 and \mathbf{a}_2 defined in Fig.3.10b. Now, the relation between \mathbf{a} , \mathbf{b} and \mathbf{c} becomes

$$\mathbf{c} = m\mathbf{b} = n_1\mathbf{a}_1 + n_2\mathbf{a}_2,$$

where n_1 and n_2 are also integers, \mathbf{a}_1 and \mathbf{a}_2 are the two components of vector \mathbf{a} . Now, in order to fix a specific angle, a relation between n_1 and n_2 is needed; from a simple geometrical analysis, valid for $0 < \theta \leq 30$, we have:

$$n_1 = \frac{\text{sen}(60 - \theta)}{\text{sen}\theta} n_2.$$

| angle (deg) | 0 | | 10 | | 20 | | 30 | |
|-----------------|------------------|------|------------------|------|------------------|------|------------------|-------|
| lattice vector | MoS ₂ | Gr |
| d_{C-C} (Å) | 1.39 | 1.43 | 1.41 | 1.43 | 1.40 | 1.43 | 1.42 | 1.43 |
| a_{MoS_2} (Å) | 3.20 | 3.30 | 3.20 | 3.24 | 3.20 | 3.27 | 3.20 | 3.22 |
| strain (%) | -2.8 | +3.1 | -1.4 | +1.2 | -2.1 | +2.2 | -0.7 | +0.5 |
| corrugation (Å) | 0.53 | 0.14 | 0.11 | 0.08 | 0.03 | 0.03 | ≤0.03 | ≤0.03 |

Table 3.1: Evolution of the C-C distance in graphene, the MoS₂ lattice parameter, the strain and the corrugation for 0, 10, 20 and 30 degrees according to the corresponding lattice vector optimization, either for MoS₂ or graphene, respectively, first and second column. A positive strain corresponds to a compression whereas a negative strain corresponds to an extension of the layer. In the strain row, under the columns defined with “MoS₂” (“graphene”) we write the strain on graphene (MoS₂) since MoS₂ (graphene) is optimized. Finally, we always refer to the graphene corrugation since on MoS₂ the corrugation is negligible.

Fig.3.10 provide a visual explanation of this technical part.

3.3.2 Four orientations: structural optimization

In order to study the effects of orientation, we consider 4 different rotation angles θ : 0, 10, 20 and 30 degrees. From the symmetry of the system, every angle θ larger than 30 degrees is equivalent to $60^\circ - \theta$. For each case, we have designed a supercell with reasonable numbers of atoms, favoring the optimization along MoS₂ or graphene lattice vector, depending on the layer we want to keep in the optimized structure. It is important to perform these two different calculations since, in that manner, we can observe the differences in the electronic properties induced by the calculation conditions, namely the artificial strain, and remove them from the possible physical effects at the interface. According to their corresponding lattice vectors, these different structures have then been optimized and the equilibrium distance between the two layers is determined, making use of the LCAO-S²+vdW formalism implemented in the Fireball code and discussed in the second chapter.

The corresponding interaction energy curves as a function of the average carbon-sulfur planes distance between graphene and MoS₂ are represented in Fig.3.11. The geometries of the unit cell designed for each angle and for graphene or MoS₂ lattice vectors are represented in the insets.

Except for the 0 degree structure, there is no noticeable difference between the interaction energies corresponding to optimization, either with the graphene or the MoS₂ lattice vectors. In all the structures, the interaction energy is around 22 meV/Å. This value is a bit lower than the one found for the AB stacking of graphene, around 40 meV/Å, calculated using the same formalism. This smaller interaction energy can be explained by the honeycomb structure of MoS₂ composed of an alternance of sulfur and molybdenum atoms, with the last kind in a lower plane.

Consequently, the molybdenum atoms are located farther from the graphene plane,

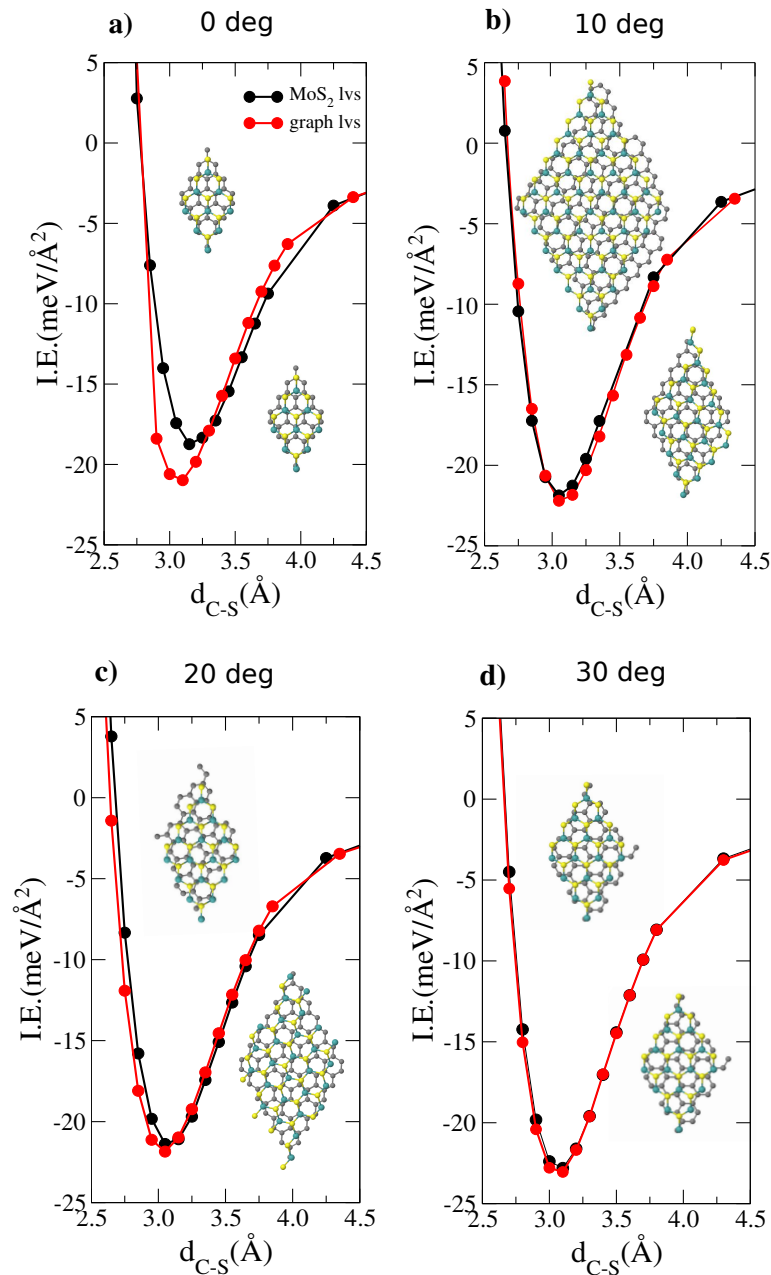


Figure 3.11: Representation of the calculated interaction energies of the graphene/MoS₂ interfaces for a) 0, b) 10, c) 20 and d) 30 degrees, as a function of the average carbon-sulfur planes distance. The corresponding geometries for graphene or MoS₂ lattice vectors are represented in up and down insets, respectively.

which reduces the overall interaction energy with the graphene sheet. Regarding the 0 degree graphene/MoS₂ interface, which is composed of a 3×3 MoS₂ and a 4×4 graphene unit cell, this superstructure presents the most important strain after optimization, either for graphene, 3.1% in extension with the MoS₂ lattice vectors, or for MoS₂, 2.8% in com-

pression with the graphene lattice vectors. As a consequence of this important strain, the graphene plane presents a larger corrugation which is responsible for the energy difference between the two lattice vectors optimization. Since there is no significant difference for the other rotation angles, we can deduce that the interaction energy mainly depends on the strain and the graphene corrugation. Regarding the equilibrium distance, defined as an average distance for the corrugated system, in all the cases it remains almost constant at 3.1 Å, independently of the strain or corrugation. The main structural characteristics for the different rotation angles are summarized in Table 3.1. The most important result is related to the corrugation. First of all, the corrugation only affects the graphene layer, while the MoS₂ remains flat even under strain. This is probably related with the three-layer structure of MoS₂ with respect to the monolayer structure of graphene. However, the corrugation is not only an effect of the in-plane compression of the graphene layer since it has also been found, with lower rate, even in graphene lattice vector optimization. Furthermore, a complementary test was made by optimizing the isolated graphene layer under a strain of -2.8%, as we have for 0 deg: in this case the corrugation is negligible, proving that it is related to the relative position of the S and C atoms, and it is enhanced by the compression of graphene layer. The maximum value of z displacement of C atoms arises when the two configurations, C atom on the MoS₂ hollow site (shorter distance between the planes, represented in Fig.3.12a, left panel) and C on S with the C-C and S-Mo bonds overlap (larger distance between the planes, represented in Fig.3.12a, right panel), are present in the unit cell. As the angle increases, the probability to find both configurations is lower, leading to a decrease of the corrugation (see Fig.3.12).

3.3.3 Global electronic properties

Once we have obtained the structural optimization for the four orientations taking into account the van der Waals forces, we moved to the analysis of the electronic structure calculation.

Optimization with respect to different lattice vectors leads to rather different results with respect to the electronic properties even though the unit cells are in principle equivalents. Looking at Fig.3.13, we can observe as at 0 degrees, in graphene lattice vector optimization (left part), the MoS₂ band gap is substantially reduced from 1.83 eV to 1.15 eV, and the bottom of the conduction band is located right at the Fermi level. Furthermore, in the case of graphene lattice vector optimization, the MoS₂ DOS shows a strong modification with respect to the isolated MoS₂ (compare Fig.3.13c black curve and Fig.3.7 left panel), which is not the case when MoS₂ is optimized (see Fig.3.13d).

Also, we can observe a small p -doping in graphene, as the Dirac point is shifted above the Fermi level. This is related with the important artificial strain on the MoS₂ layer, favoring a charge transfer from graphene to MoS₂. The reduction of the gap, as well as the switch from direct to indirect gap, is a result we have already discussed in the previous section concerning the strain effect on MoS₂. However, the charge transfer between the layers, leading to the doping of graphene, is an effect coming from the presence of both layers. In fact, even if graphene and MoS₂ interact by mean of a weak interaction, a small

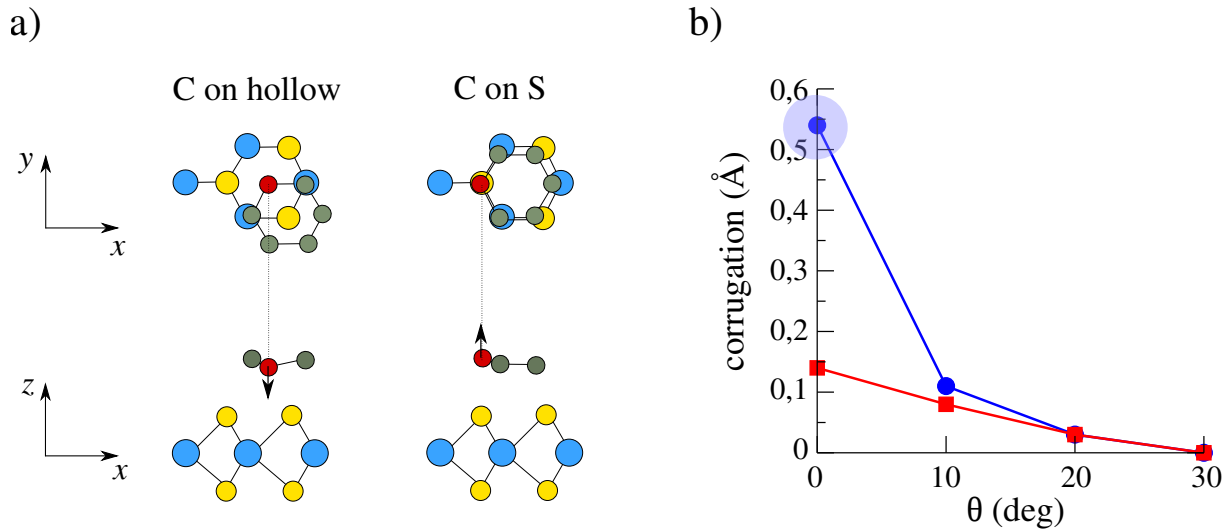


Figure 3.12: a) Graphic representation of the position of C atoms with respect to the S atoms for $\theta = 0$ degrees corresponding to the larger z displacement and, as a consequence, larger corrugation. On the left panel, the C atoms on the MoS₂ hollow can move closer to the MoS₂ plane than for C on S atom case; in fact, for C on S, represented on the right panel, C feels the repulsive interaction with the lower S atom leading to C moving farther from the MoS₂ plane. b) Corrugation of graphene calculated in MoS₂ (blue circles) and graphene (red squares) optimized parameters as a function of the rotation angle θ . The corrugation is calculated as the difference between the larger and lower z coordinate of C atoms.

charge transfer is possible of ~ 0.0055 el/Å². Since the same strain on graphene does not show any important effect on the electronic structure, we will consider the MoS₂ lattice optimization for the rest of the study, in order to avoid any artificial strain effects. In this way we are able to separate the rotation and the artificial strain, focusing our attention on the role of the pure orientation on the electronic properties.

The band structure and the DOS for 0, 10, 20, 30 degrees are represented in Fig.3.14. For each angle, the Dirac point is now located at the Fermi level, as expected for the isolated graphene layer. Notice that the Dirac cone is mapped at the Γ point for the 10 and 30 degree structures, due to the particular symmetry of the corresponding supercells. Indeed, as is well-known [31,32], when an $n \times n$ supercell is considered, the corresponding BZ is reduced by a factor of $n \times n$. As a consequence, the k-points are remapped into the shrunken BZ by projection. This is the so-called BZ folding effect, shown in Fig.3.15.

While Γ is always located at the center of the BZ, the other symmetry points (K and M in the hexagonal structure) can be projected in different points depending on the periodicity and the crystal structure of the supercell. In the specific case of a hexagonal crystal structure, when n is a multiple of 3, the K symmetry point is projected on Γ , as happens in our case for the 10 and 30 degree configurations.

Also, the bottom of the MoS₂ conduction band is now located at 0.3 eV above the

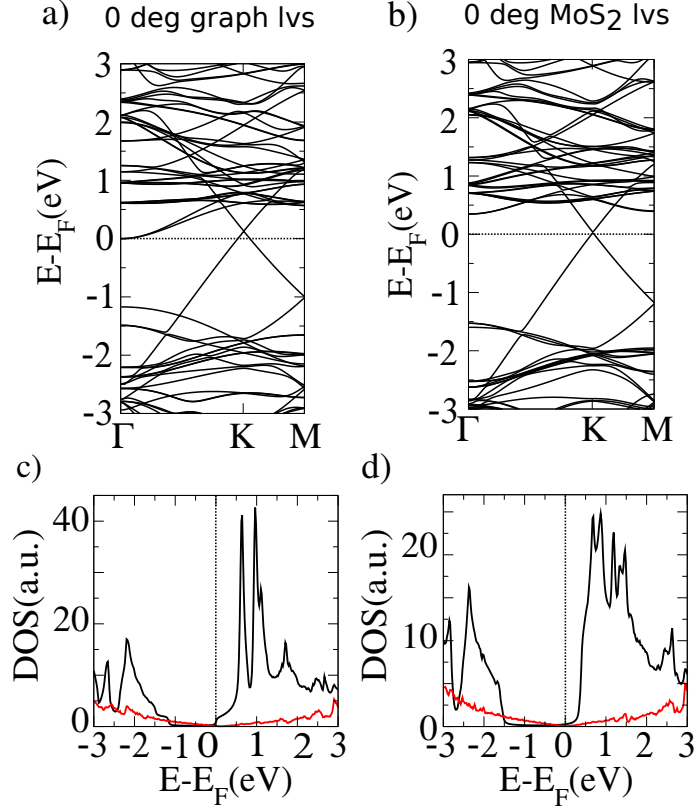


Figure 3.13: Calculated band structure and DOS for the 0 degree graphene/MoS₂ unit cell optimized using: a) and c) graphene lattice vectors, b) and d) MoS₂ lattice vectors. On the left, for graphene lattice vector optimization, a small p -doping of graphene is observed due to the artificial strain induced in MoS₂, favoring an important charge transfer. The red (black) line refers to graphene (MoS₂) DOS.

Fermi level and the MoS₂ band gap presents the same value for all the considered angles. Since the 20 and 30 degrees configurations are made with the same number of MoS₂ unit cells, we can do a MoS₂ band to band comparison that does not reveal any band structure dependence on the orientation. The similarity of the DOS for each configuration also demonstrates that the orientation does not affect the global electronic properties which results in the simple superposition of the electronic properties of the single system, as suggested by Geim *et al* [8]. However, in these initial calculations, there is an electronic level misalignment that should be corrected. Using the 0 degree cell and comparing the level positions with respect to the isolated layers, we have defined a unique scissor potential that will be applied for all the angles considered here. For example, the scissor-corrected DOS and band structures for 0 and 20 degree are represented in Fig.3.16. It is important to notice that the MoS₂ conduction band is now shifted by 0.7 eV above the Fermi level.

We can thus conclude this paragraph by stating that the global electronic structure of the graphene/MoS₂ interfaces is not affected by the rotation angle. However, small modifications of the local electronic structures may appear, as we will discuss in the following.

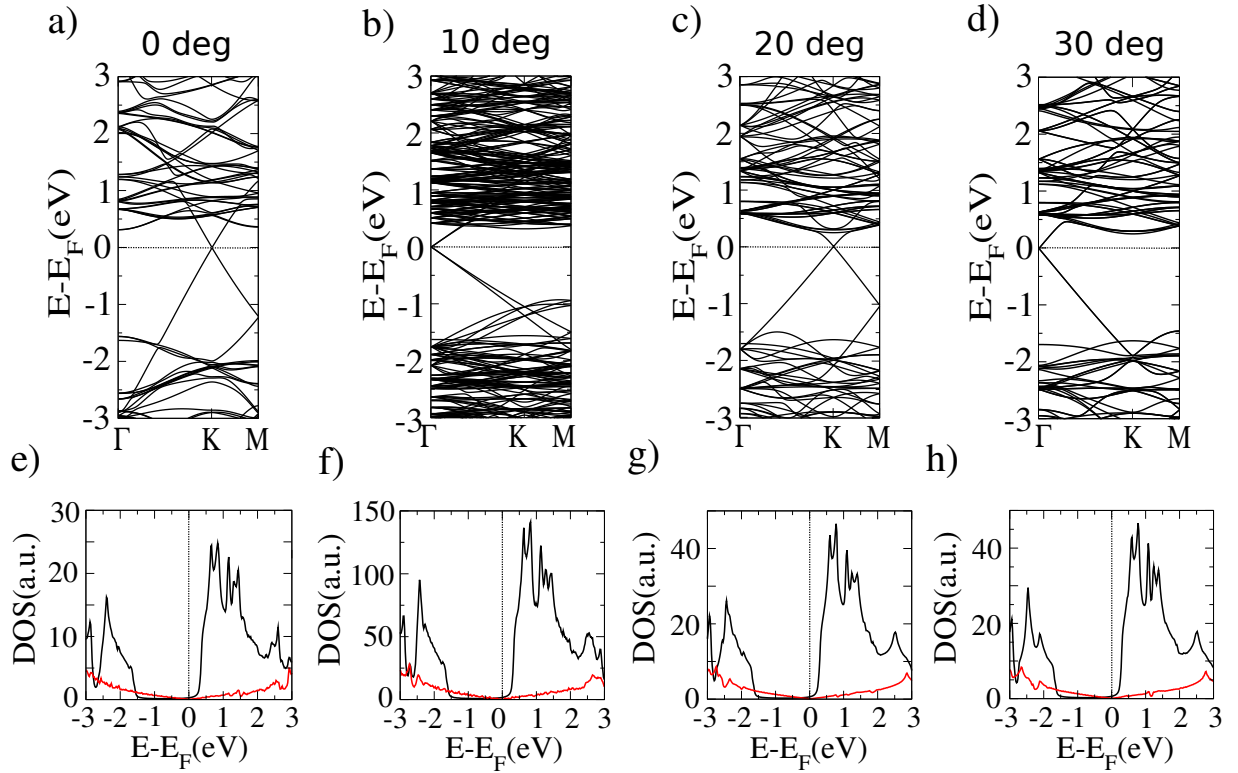


Figure 3.14: Electronic band structures and DOS without the scissor operator for 0 degree a) and e), 10 degree b) and f), 20 degree c) and g), 30degree d) and h) in MoS₂ lattice vector optimization. The black (red) lines in DOS corresponds to MoS₂ (graphene) layer.

3.3.4 Local electronic properties: STM calculations

We now consider the modeling of STM images of graphene/MoS₂ interfaces. In order to well analyze the images of the interface, we first take a look at the STM images of the isolated graphene and MoS₂ planes, presented in Fig.3.17 a) and b) respectively. In both cases, an hexagonal arrangement is obtained, where the maximum corresponds to the C atoms in graphene for a voltage of -0.1 V while the bright spots are associated to both S and Mo sites on the MoS₂ for $V=+0.7$ V. Even though the Mo atoms are located more than 1Å below the S atoms, the much higher electronic contribution compensates the geometrical effect.

In Fig.3.18 we present the STM images for 0 and 20 degrees, at 0.7 V (*i.e.* in the conduction band of MoS₂), based on the scissor-corrected electronic structures, the atomic structure unit cell is superposed. As a first remark, we can deduce that even though the global electronic properties remain the same, at the local scale different Moiré patterns can be obtained for the STM images according to the rotation angle. It is important to notice that the bright spots for 20 degrees are placed on the hollow sites of the graphene monolayer due to the large contribution of the non-directional *d*-orbitals in the tip and the

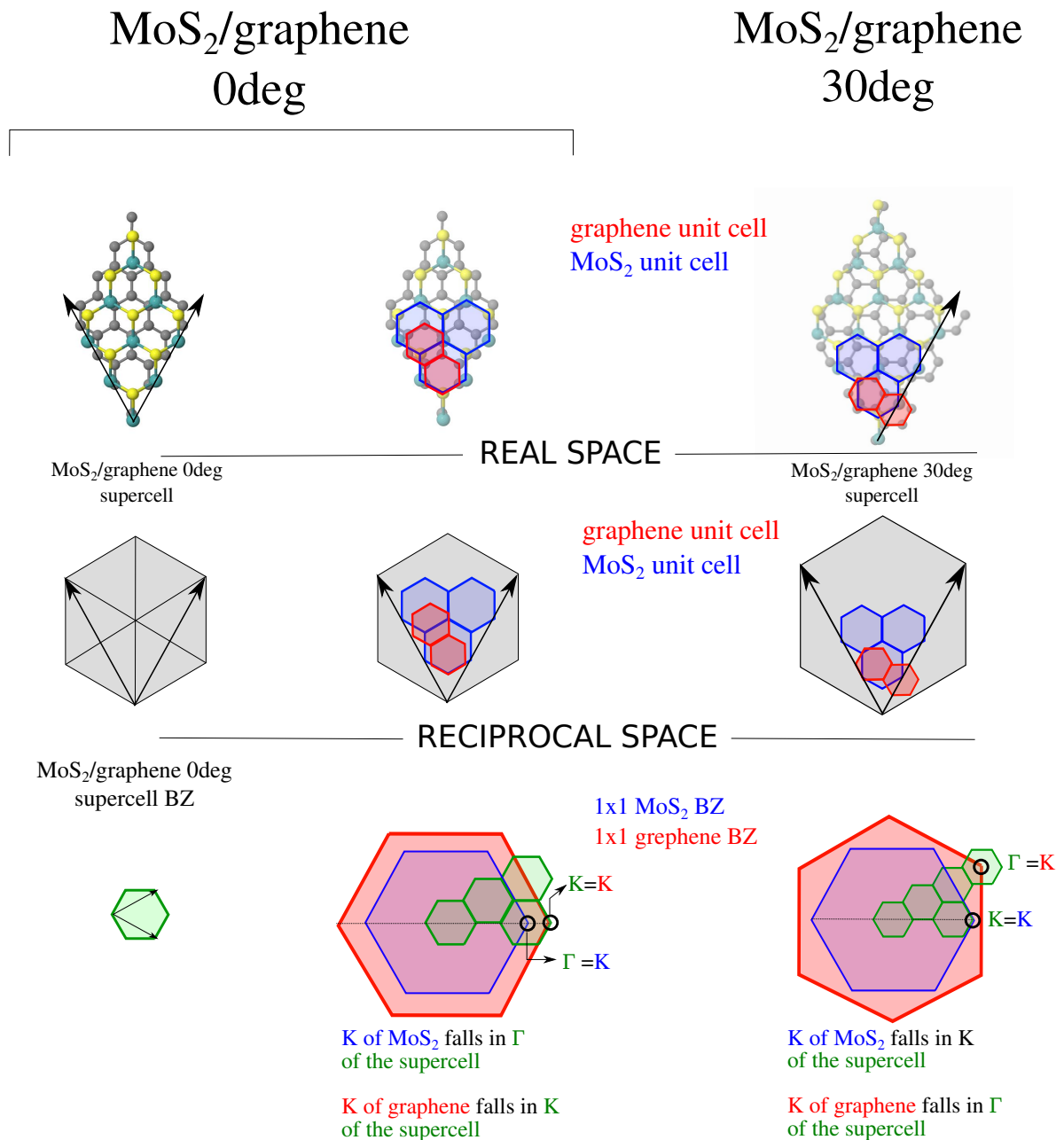


Figure 3.15: Representation of folding effect in the re-mapped position of the symmetric points Γ and K in the folded supercell BZ, for 0 deg and 30 deg. In the real space we find the blue (red) hexagons representing the MoS₂ (graphene) 1×1 cells. The supercell in the real space is represented with grey hexagon. In the third panel representing the reciprocal space we find: the supercell BZ represented by the small green hexagons, the 1×1 MoS₂ and graphene BZ represented by the blue and red big hexagons, respectively. In order to know where the symmetric points of graphene and MoS₂ are re-mapping in the supercell, we will repeat the supercell BZ in the bigger 1×1 cells of MoS₂ and graphene until the symmetric points match. According to the rotation angle, the symmetric points can fall in the same position or be re-mapped.

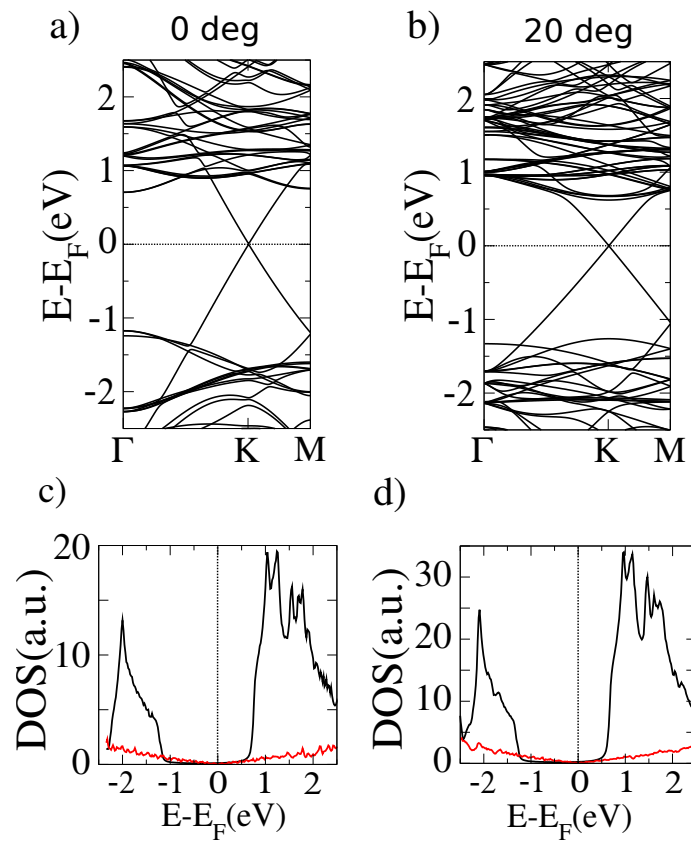


Figure 3.16: Electronic band structure and DOS for a) and c) 0 degree, b) and d) 20 degree in MoS₂ lattice vector optimization with scissor operator.

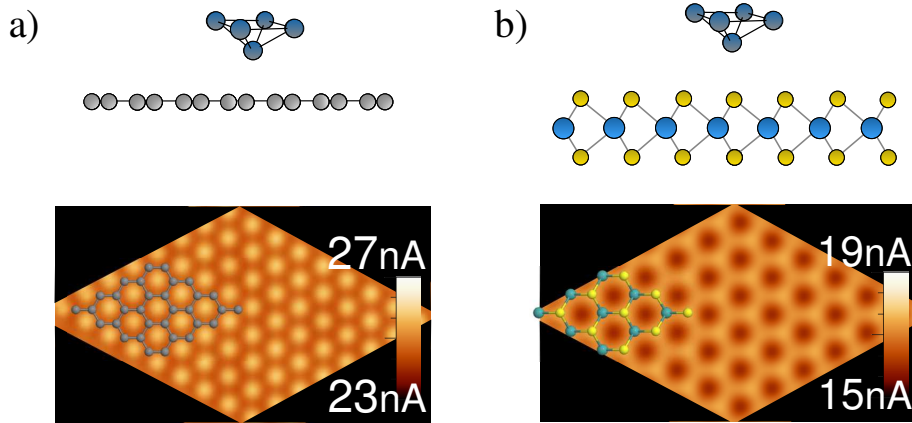


Figure 3.17: Calculated STM images of isolated graphene and MoS₂ for a) and b), respectively. The cartoons represent the considered systems, tungsten tip and graphene or MoS₂, for the relative STM images below.

C-C distance reduction due to the graphene compression. Those Moiré patterns have been already observed in ARPES experiments for example, as mini-gap opening in the global bandstructure of the interface [91]. As the electronic structure of the C atoms is almost unaltered, the difference in the brightness of the spots is directly linked to the corrugation in the graphene sheet. For example, the Moiré pattern for the 0 degree unit cell exhibits large black area around the C-atoms in the lower position, *i.e.* the hollow site with a S atom below, while the brightest sites correspond to the coincident points where a C atom of the graphene monolayer falls over a S atom of the MoS₂ layer. In order to check the effect of the MoS₂ layer in the current, we represent in Fig.3.18 c) and d) the STM image for an isolated graphene plane in the configuration of the graphene/MoS₂ interface for 0 and 20 degrees, respectively (namely keeping the structure and the electronics of graphene in graphene/MoS₂ interface). The main features of the graphene/MoS₂ STM image are caught by the image of the isolated graphene layer, but less defined spots are obtained. This result means that there is a modulation effect in the image due to the inclusion of the MoS₂ layer. The STM images of the other cells show a less pronounced contrast between the bright and the dark areas due to the lower corrugation. Hence, the corrugation decreases as the rotation angle is increased (up to 30 degrees) as we reported in Table 3.1. Also notice that the corrugation is mainly due to the interaction between graphene and MoS₂ and we found with further calculations that, without MoS₂, the graphene monolayer remains flat even in the most corrugated case, which also corresponds to the most strained case. On the other hand, the interaction between graphene and MoS₂ is reflected in the change in the STM image, when the MoS₂ underlayer is removed (compare Fig.3.18 a) and b), and 3.18 c) and d) images). In that respect, graphene acts as a grid for MoS₂ electronic structure.

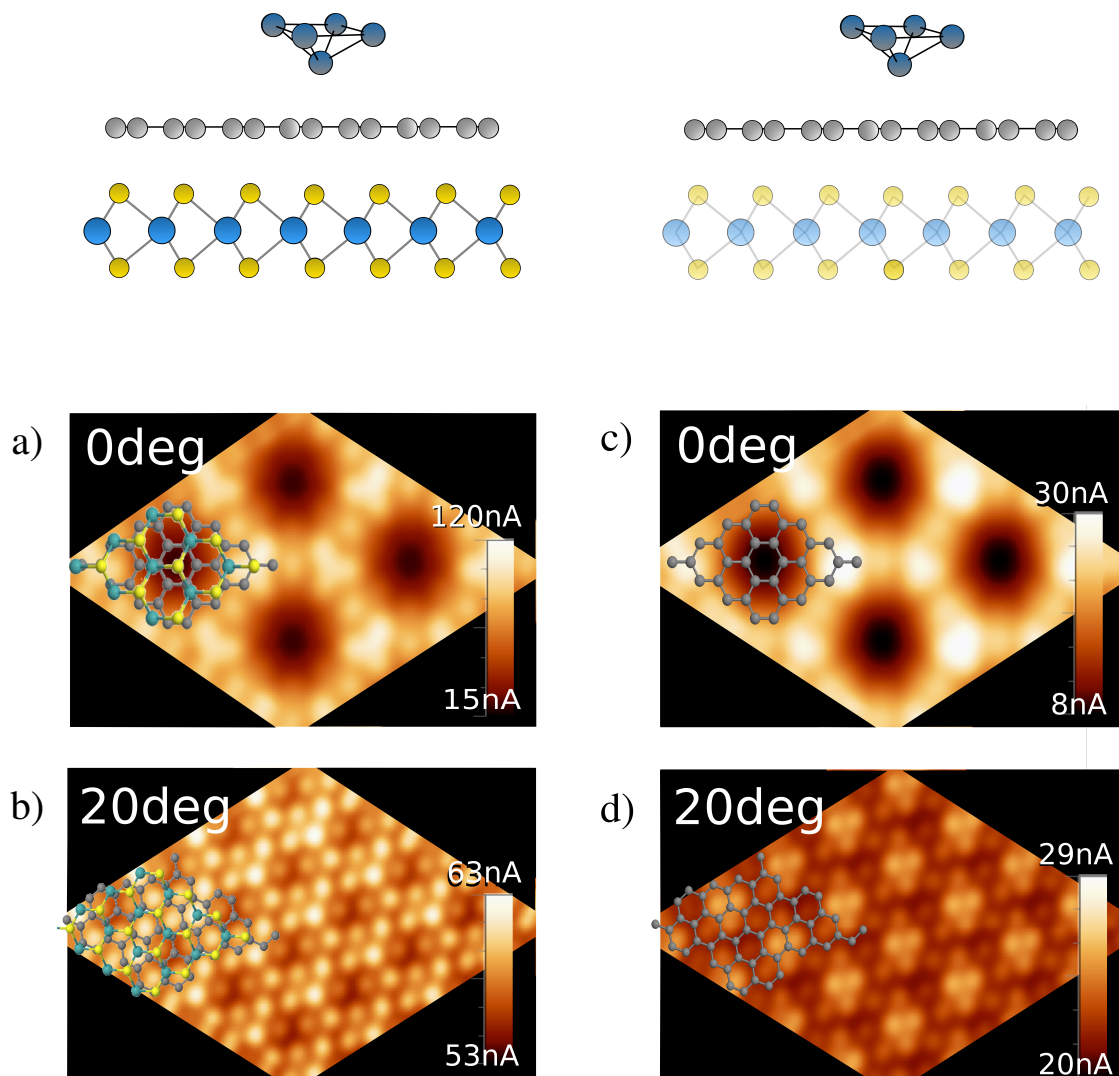


Figure 3.18: Calculated STM images of graphene/MoS₂ for a) 0 degree and b) 20 degrees. In c) and d), STM images calculated on isolated graphene, in the corresponding graphene/MoS₂ configuration, keeping both the structural and electronic modifications given by MoS₂ on graphene. The cartoons represent the considered system for the STM images under the same column: on the left, tungsten tip on graphene/MoS₂ interface; on the right, same tip on graphene in the corresponding graphene/MoS₂ structural and electronic configuration, namely without considering the contribution of MoS₂ on the tunneling current.

Summary

Together with the shown results, we have also calculated the charge transfer between the two layers, which is very small ($0.005 \text{ el}/\text{\AA}$), in agreement with the unaffected electronic structure with the rotation angle. As a consequence of these results, it appears that the graphene/MoS₂ interfaces will not be affected by the rotation angle between the two layers. However, their local electronic properties modifications can be exploited through specific connections on the area with high or low electronic density.

To summarize, this part of the work represents a full study of the influence of the rotation angle on the electronic properties of the graphene/MoS₂ interface. As a result, the global electronic structure remains unaffected by the rotation, even though calculations have to be conducted with a careful choice of lattice vectors and supercells to avoid artificial effects. For example, Yandong Ma et al [16] have theoretically demonstrated small gap angle dependence the graphene/MoS₂ interface determined by *ab initio* calculations. It resulted in a gap opening in the graphene bandstructure for specific rotation angle at the graphene/MoS₂ interface, which might be due to the strain induced by the choice of the supercell and the corresponding lattice vectors. The rotation angle has however an influence on the local electronic properties through the different Moiré patterns observed in the calculated STM images.

These results, however, present differences with some experimental results as the band bending [92] observed at such interfaces, able to modify the global electronic properties of the system.

The discrepancy between the theoretical and experimental results are also illustrated in a collaboration with the experimental group of Centre de Nanosciences et de Nanotechnologies, CNRS and Univ. Paris-Sud, Université Paris-Saclay and the Department of Physics and Astronomy, from University of Pennsylvania, Philadelphia [86]. The results coming from this collaboration are presented in the next section.

3.4 Oriented MoS₂ on graphene: experimental results

By making use of several characterization techniques, the experimental group supervised by Abdelkarim Ouerghi investigated the impact of the change of orientation between MoS₂ and graphene layers on the properties of MoS₂ [86].

From the experimental point of view, a high quality substrate is the starting point of the study of heterostructures, since their properties is strongly affected by the quality of the interface between the underlying substrate and the top-layer. Epitaxial graphene on silicon carbide (SiC) was used as a substrate, providing advantages as the highly ordered crystalline structure favoring the commensurate growth. The obtained MoS₂ monolayers are composed by two MoS₂ oriented flake of $33^\circ \pm 2^\circ$ for the small flake and $4^\circ \pm 2^\circ$ for the big one, showing equilateral triangle shapes with lateral sizes of ~ 20 to $\sim 200 \mu\text{m}$. The high quality of the MoS₂/graphene heterostructure was ensured, underlined by the uniform

color within one single flake in the optical image (Fig.3.19a). A schematic presentation of the sample is provided in Fig.3.19b.

By means of Raman spectroscopy and photoluminescence (PL) measurements, the experimental group was able to explain the evolution observed in MoS₂ structural and optical properties when two different orientations are considered. From the structural point of view, for the two flakes grown in exactly identical conditions, a variation of strain of $0.6\pm 0.1\%$ is found (larger strain in the bigger flake), justified by the different orientations. On the other hand, in Fig.3.19c and Fig.3.19d the PL data obtained by the experimental group, provide the information about the band gap modification. The image in Fig.3.19c represents the PL map from the single layer MoS₂ regions, in which we can easily distinguish the different PL intensities between the big (darker color) and the small flake (brighter color). Moreover, from the PL spectra reported in Fig.3.19d, we can notice the strong peak at around 1.85 eV of the small flake, reflecting the direct bandgap at the K point of the BZ, whereas the big flake is characterized by a smaller peak displaced at 1.79 eV. The band gap values of 1.85 eV and 1.79 eV for both the small and big flakes respectively (Fig.3.19d) are in agreement with those reported for MoS₂ monolayers. Moreover, it is found that the ratio between the PL intensities of the two flakes of about 3/2 is similar to what has been observed for monolayer and bilayer MoS₂, where the gap becomes indirect. Even if several hypothesis can be made to understand the origin of this change in MoS₂ bandgap, revealed by PL measurement, as the presence of impurities, the most reasonable explanation is related to the bandgap transition from direct to indirect in MoS₂. In fact, the PL quenching occurred for the flake affected by higher tensile strain which may be responsible for the transition from direct to indirect bandgap in monolayer MoS₂.

Our DFT calculations, already discussed in the previous section 3.2, support this result. The value of the band gap we found is in agreement with the experimental results (we recall the Fig.3.8 where the evolution of the band structure under biaxial strain is shown), as well as the evolution of the band gap type from direct to indirect at 0.6% of strain. All these results suggest that tuning the interlayer orientation could induce a strain change in MoS₂ which may cause variations of MoS₂ bandstructure [93, 94]. Thus, it seems possible to tune the band structure around the K point via selectively choosing different orientations of the considered MoS₂ flakes.

It is important to underline that these experimental results suggesting the possibility to tune the band gap of MoS₂ by changing the orientation are not in contrast with the previous theoretical results that the orientation alone does not affect nor the band gap neither the main feature of band structure.

In fact, this discrepancy can be explained in the following way: in the theoretical approach, it is possible to isolate the orientation effect from the edge, impurity and strain. Referring to the strain effect, we chose the supercells keeping the MoS₂ in the optimized structure - whereas the graphene was affected by a small strain - because the MoS₂ electronic characteristics are strongly dependent on the strain. In this way, any potential modification of the band structure, that we did not find in our calculations, had to be referred to the orientation. Moreover theoretically, the interface is composed of two infinite planes, which implies a full van der Waals interaction between the two structures. On the other hand, the ex-

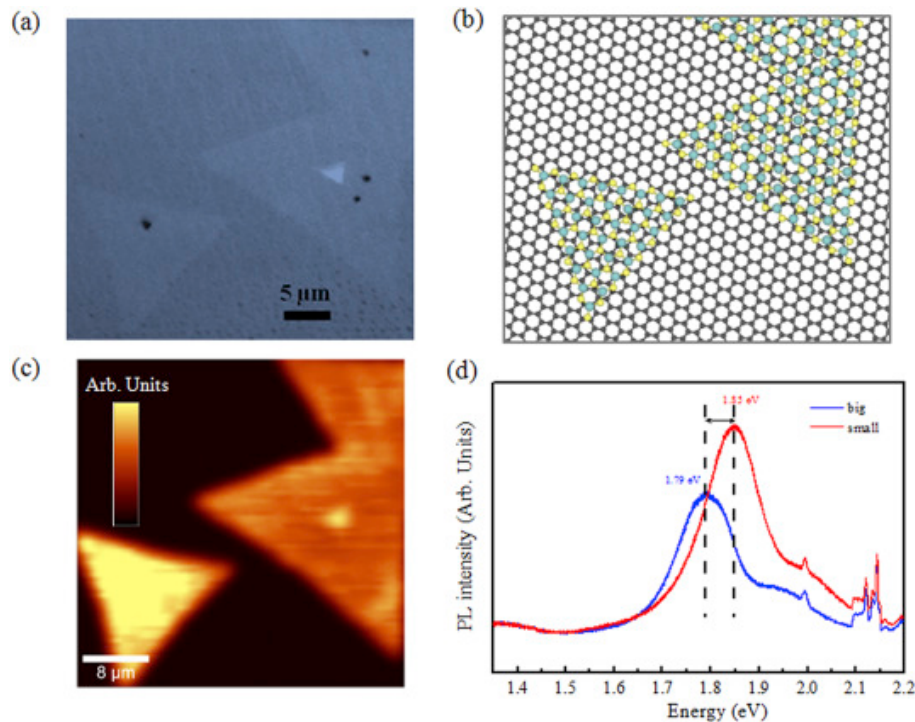


Figure 3.19: a) Optical image of the MoS₂ flakes transferred onto the epitaxial graphene layer, b) 3D schematic structure of single layer MoS₂ flakes on a graphene supporting substrate; in c) the map of the photoluminescence intensity of the MoS₂ flakes on graphene is shown and in d) the PL spectra corresponding to the big (blue curve) and small (red curve) flakes of MoS₂ on graphene are characterized [86].

perimental graphene/MoS₂ interface is composed of MoS₂ triangles deposited on graphene, which present therefore connections at the border, whose nature is slightly different from vdW interactions. Indeed, the triangle edges present dangling bonds which are much more reactive than the π orbitals involved in the weak vertical interaction. We think that the main difference in structural and electronic behaviour of vdW heterostructures between experiment and theory comes from those dangling bonds forming lateral heterostructure between MoS₂ and graphene that can be responsible for strain effects and, consequently, for the band gap modification.

3.5 MoSe₂/graphene: beyond van der Waals interaction

In this section we will discuss the results obtained in collaboration with an experimental group in the CEA Grenoble, recently published in [95]. This project and all the experimental activities we show in this section were led by M. Jamet at Spintec.

The vdW heterostructure MoSe₂/few-layers graphene, grown on Silicon carbide (SiC) is

characterized: the surface analysis gives a complete picture of the atomic structure and the electronic properties of the heterostructure.

The main result related with our work consists in the band-gap modulation in the few-layer graphene, well supported by electron spectroscopy data and our DFT calculations. The most important part of this research is represented by the fact that, in this heterostructure, the interlayer interaction goes beyond the simple van der Waals leading to an important charge transfer, that is not present in the graphene/MoS₂ case previously discussed, due to the absence of substrate.

In the following, we will show some results obtained by the experimental group, mostly focusing on the measurements, then our calculations and the explanation of the opening of the band gap in K. The experimental group has used different techniques to completely characterize the MoSe₂/few-layer graphene heterostructure: scanning tunneling microscopy and scanning tunneling spectroscopy at low temperature (STM and STS, respectively), grazing incidence X-ray diffraction (GIXRD) using synchrotron radiation, and photoemission electron microscopy imaging in k-space (k-PEEM). These techniques allowed to study the atomic (STM, GIXRD) and electronic (STS, k-PEEM) structures of the vdW heterojunctions. In this work, the large-scale heterostructure was grown by MBE [96] using the vdW epitaxy of MoSe₂ on a graphene/SiC substrate.

In Fig.3.20a and b, we report the measurement performed by the experimental group of the band dispersion of few-layer graphene, obtained using k-PEEM: the band structure of MoSe₂/few-layer graphene on SiC and the few-layer graphene on SiC (without MoSe₂) are shown in Fig.3.20a and Fig.3.20b, respectively.

In both cases (with or without MoSe₂) we find the typical linear dispersion, however, the two images reveal some differences defining the effect of MoSe₂ on the band structure of few-layer graphene. One effect is the decrease of the photoemission signal close to the region at 0.3 eV below the Fermi level revealing a band-gap opening when the MoSe₂ is on the few-layer graphene. Another effect we can observe is the broadening of the Dirac linear dispersion if MoSe₂ is placed on the few-layer graphene. This changes of the electronic states reveals an important interaction between the 2D layers. Furthermore, the plot of the integrated intensity as a function of the binding energy in the area around $k_{\parallel}=0$ of the heterostructure and bare graphene (Fig.3.20c), confirms this feature: the distinct dip at 0.3 eV below Fermi level for the heterostructure with MoSe₂ is assigned to the existence of a band gap in few-layer graphene.

By means of our theoretical calculations it was possible to provide an interpretation to what has been found experimentally, namely the increase of the band-gap value in few-layer graphene of approximately 250 meV.

The origin of the gap opening can be found by analyzing all the possible phenomena at the interface.

For instance, the opening of the gap can be due to the strong chemical interaction affecting the chemical configuration of graphene. Hence, the switching from sp^2 to sp^3 orbitals causes the destruction of the linear dispersion. However, we know that there is no chemical bond between graphene and MoSe₂, according to the lack of dangling bonds at the surface

characterizing the vdW heterostructures.

Another phenomena that can have an effect on the electronics of graphene comes from the relative orientation of lattices: for instance, in MoS₂/graphene [91] and hBN/graphene [97], obtained by mechanical exfoliation and a transfer process, the opening of the minigaps is a consequence of the superlattice potential associated with a long-range Moiré pattern or a breaking of inversion symmetry in the graphene sublattices. However, the minigaps are located far away from the Fermi level, suggesting that the gap opening in this case is not related to the super potential.

Furthermore, the experimental data from GIXRD and STM did not reveal any Moiré signature in the heterostructure, that should be seen for a Moiré period of $\lambda = (1/m+1)a \approx 1$ nm [98], where m , the lattice mismatch between MoSe₂ and graphene, is 36% and a relative rotation of lattices is 0 degrees.

Consequently, one can deduce that the electronic structure evolution and the opening of the gap in few-layers graphene is due to the not negligible charge transfer between the layers, enhanced by the presence of MoSe₂. The charge transfer, given by proximity effect inside the vdW gap through orbitals overlapping, leads to the Fermi level shift and a consequent hole or electron doping in few-layer graphene. In particular, the high n -type doped MoSe₂ observed in STS measurements gives rise to a significant electron transfer from graphene to MoSe₂. At the end, the larger band gap, increased with the presence of MoSe₂ monolayer, is due to an enhancement of electrostatic potential and a consequent reinforcement of dipole fields in few-layer graphene [99].

To support this experimental observation, we performed first-principles calculations taking into account vdW interactions between different layers. As in the experiment, we considered two different systems, with and without MoSe₂, in particular bilayer (BL) graphene/SiC and MoSe₂/BL-graphene/SiC (BL graphene has AB-stacking order). The corresponding unit cells used for calculations are shown in Fig.3.21a and b, in which we can recognize the carbon buffer layer between SiC and graphene, as formed during the silicon sublimation process [100].

Regarding the structure, we found an out of plane contraction (6.5%) of the MoSe₂ layer, from 3.38 Å for a free-standing layer down to 3.16 Å for MoSe₂/BL-graphene/SiC, caused by the electron transfer between the BL-graphene and MoSe₂. However, according to the used LDA-DFT technique known to underestimate lattice parameters by approximately 5%, the calculated value is smaller compared to the layer thickness extracted from X-ray diffraction of 3.34 Å.

The charge transfer, indicated as numbers in units of elemental charge (e) per unit cell for each layer, is estimated for both the considered systems and indicated in Fig.3.21a and b. The presence of MoSe₂ increases the charge transfer leading to a n -doped MoSe₂, in agreement with STS measurement where n -type doping in MoSe₂ is observed. The evolution of the charge transfer from BL-graphene/SiC to MoSe₂/BL-graphene/SiC is in agreement with the experimental result and with the explanation of the opening of the gap. It has also been found that increasing the number of graphene layers in the calculation, from two to four, leaves almost unchanged the charge distribution between MoSe₂ and graphene, indicating the low impact of the graphene layers on the charge transfer process.

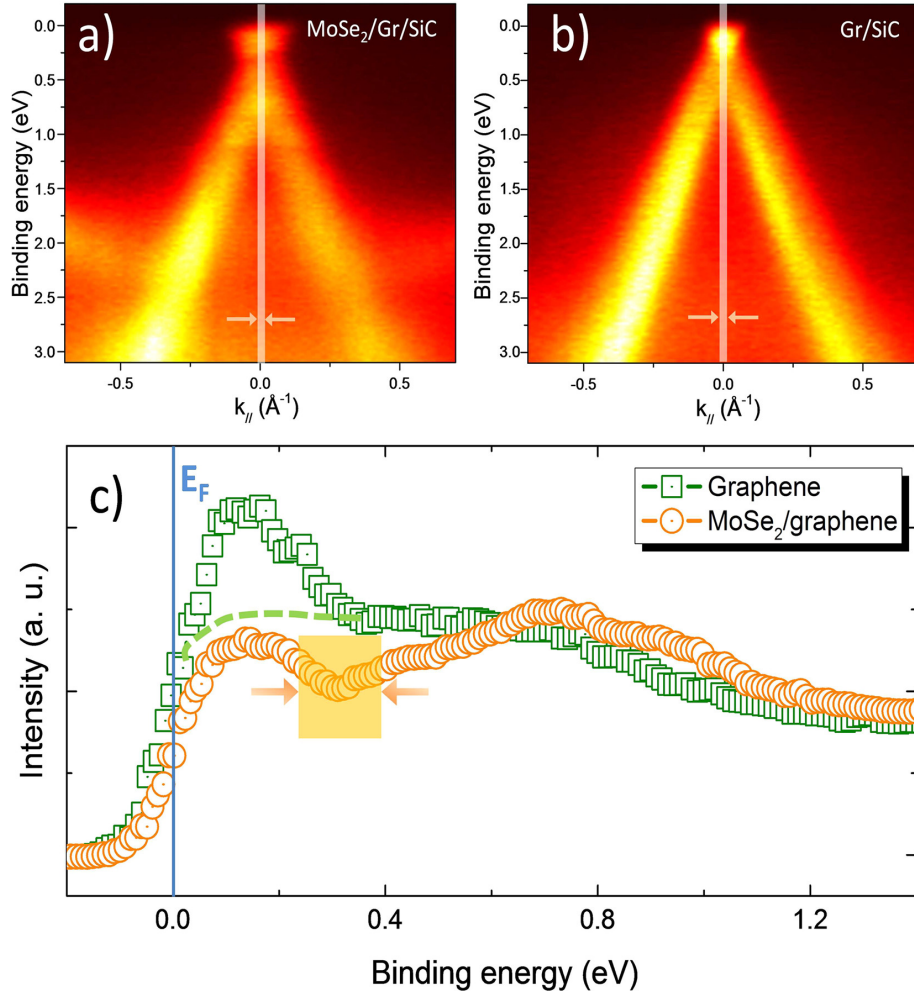


Figure 3.20: Dispersion of graphene π bands as a function of the k_x direction in the case of the MoSe₂/few-layer-graphene heterostructure a) and of the few-layer-graphene/SiC substrate b). The integrated intensity curves over binding energy from E_F to $E_F + 1.4$ eV are reported in c), extracted from the area around $k_{||} = 0$ (white rectangles in a) and b)). The dip corresponding to the band gap is highlighted by arrows.

The band structure of bilayer graphene shown in 3.21 is highlighted in red and blue, showing two distinct cones for the conduction and valence bands. We can deduce that the adjacent graphene layers are electronically decoupled and the nearly independent linearly dispersing bands at the K point of graphene appear [101].

The difference in the two systems is in the gap value, 158 meV for BL graphene/SiC and 256 meV for MoSe₂/BL graphene/SiC. The opening of the gap can be explained as following: without MoSe₂, a charge transfer from the substrate on the lower graphene is found, whereas on the upper graphene it is very low. This charge transfer leads to an electric field responsible for the breaking of sublattice symmetry within graphene sheets leading to the gap opening [102]. Then, adding the MoSe₂ layer, the charge transfer on

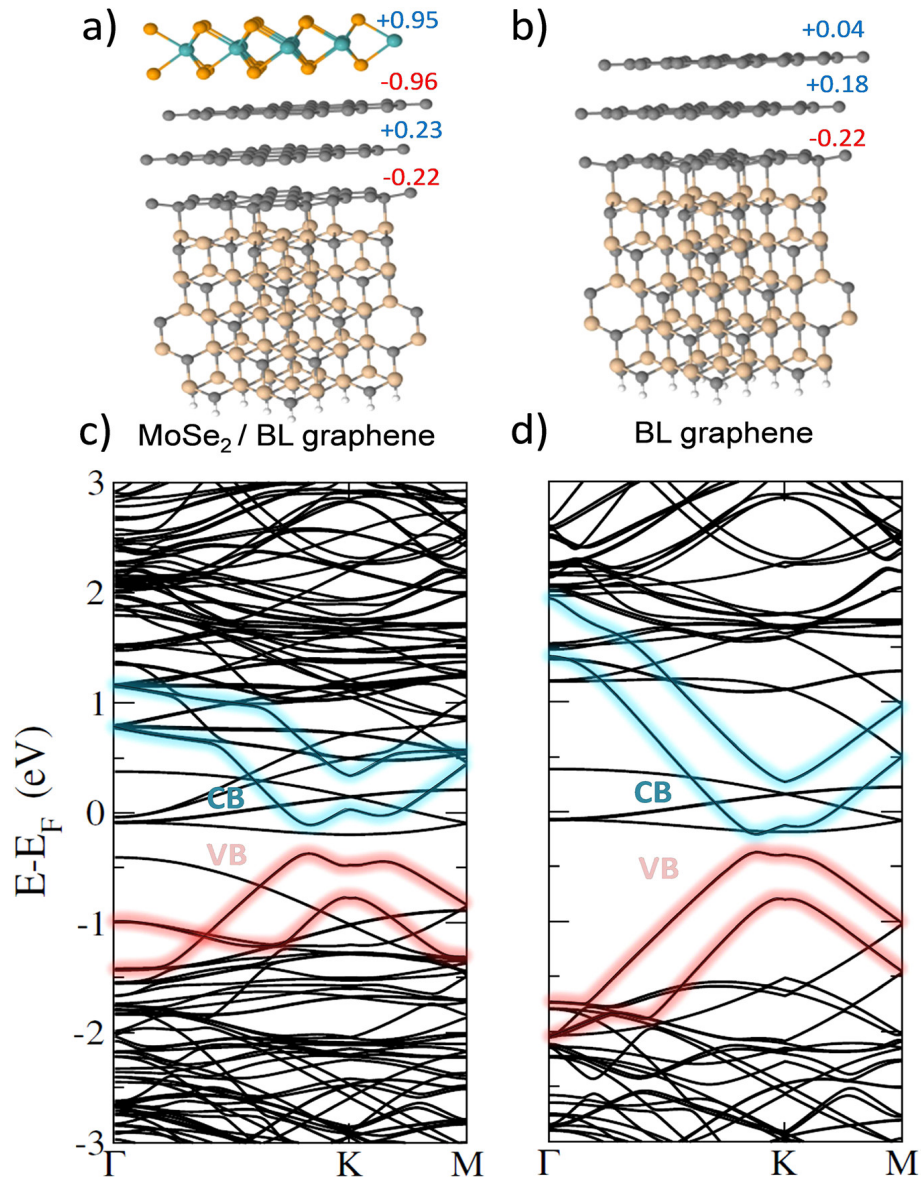


Figure 3.21: Calculation results obtained from heterostructure and MoSe₂-free substrate with BL graphene: charge distribution in different layers in the heterostructure a) and MoSe₂-free substrate b). The amounts of transferred charge calculated for each atomic layer are also displayed (positive or negative signs indicating an excess or a deficit of electrons, respectively). Band structures of heterostructure and MoSe₂-free substrate are shown in c) and d), respectively.

the upper graphene drastically increases, and the electric field felt by the first graphene as well, causing the increase of the gap value as well. The electric field coming from the charge transfers between the different layers is responsible of the breaking of sublattice symmetry within graphene sheets leading to the gap opening [102].

However, in the experimental band dispersion data in Fig.3.20, the few-graphene layers on SiC do not show any gap, but a single cone with very broad branches. This discrepancies with the theoretical results have to be assigned to the difference of the number of graphene sheets in the experiment and in the calculations: the estimated seven graphene layers in the experiment are responsible for the vanishing of the gap.

Summary

The origin of the band-gap opening was interpreted as a result of a significant electron transfer from graphene sheets to MoSe₂. We have to notice that this kind of modification of the band structure was not found in our theoretical calculations of MoS₂/graphene, since in that case the substrate was not considered and, consequently, no charge transfer from the substrate was present to break the symmetry and to modify the electronic properties of the component 2D layers.

In this section, we pointed out that few-layer graphene was subjected to charge transfer processes from the substrate and the TMDC layer, leading to an enhancement of the band-gap-induced electric field in the graphene sheets.

Chapter 4

Graphene and MoS₂ for a new Field Effect Transistor generation

The transistor represents the fundamental building block of modern electronics. Being able to switch or amplify the signal, it allowed the building of smaller and cheaper electronic devices, as computers, calculators, radios...

The first transistor (see Fig.4.1) was built in 1947 in USA, in the Bell Telephone Laboratories [103]. Here Shockley, Bardeen and Brattain, already before the second World War, were convinced that silicon semiconductor, recently discovered to exist in *n* or *p* doping type according to the kind of impurity, was extremely useful to amplify current signals and, consequently, to become the basis of all electronic devices. The first transistor was made by a *n*-doped germanium (base) and two gold contacts (emitter and collector). They demonstrated that by varying the current to the base, it was possible to obtain a linear variation of the collector potential. In 1956, the Nobel prize was conferred to Shockley, Bardeen and Brattain, for the discovery of transistor which was defined as "probably the most important invention of the 20th Century".

In general, the transistor is a three terminal, solid state electronic device able to control the electric current flowing in the channel region between two contacts (called collector/emitter or source/drain) by changing the electric current or the voltage using the third contact (called base or gate). Nowadays, there exist many kinds of different transistors, and here we will focus on one specific type called Field Effect Transistor (FET), that uses a potential to control the electric current flowing in the device, by affecting the size and the shape of the channel. A schematic FET is shown in Fig.4.2. The current flowing between the source and drain contacts, in the region called channel, is controlled by the gate, placed on the top.

According to the applied voltage between the gate and the bulk and the source-drain voltage, the current in the channel presents three different behaviours related to three states operation of transistor:

- the OFF region, when the channel is not active and no current flows in the transistor;
- the ohmic or linear region, where the transistor behaves as a resistor;



Figure 4.1: First transistor built in 1947 by Shockley, Bardeen and Brattain (picture taken from the web [104]).

- the saturation region, where the current does not depend on the voltage between the source and drain (V_{SD}) anymore.

In Fig.4.3 the fundamental operation of a transistor is shown.

As we said in introduction, the transistor can amplify or switch the current. In this work, we focus on the second operation type FET, namely a logic device. In this case, a transistor can be found in ON or OFF state, depending on the applied gate voltage, determined by the largest I_{ON} current and by a very low I_{OFF} flowing in the channel, respectively.

For a logic transistor, the ratio between the ON and OFF current (called ON/OFF ratio), is a parameter describing its performance, and its value should be between 10^4 and 10^7 .

Since its birth, the transistor was able to decrease the size of the electronic devices, however this process becomes a sort of challenge in the next future and so far: the continuous miniaturization of the electronic devices and the increase of circuit complexity is the results of the Moore's law [19].

To sustain this process, there is a continuous improvement of the small devices operations in the last years: faster and less power consumption transistor have been produced, and the ability to integrate complex function increases. However, the progressive miniaturization reaches a limit beyond which the performance of a FET starts to decrease. The main problems are related with the discreteness of matter, short channel [23, 24] and surface effect, due to dangling bond. They become more important in very small devices bringing to the knowledge that the scaling of devices and simultaneously good performance become more and more difficult.

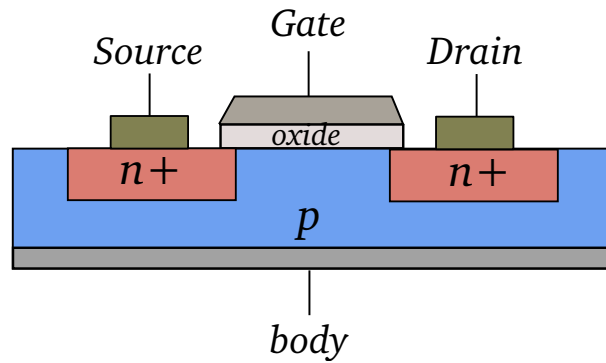


Figure 4.2: The three terminals source, drain and gate are shown. The source and drain contacts are connected to the n doped part of the semiconductor, whereas the bulk (the whole blue area) and the channel (the part of the bulk between the n doped region) are p doped. The gate, placed on top, tunes the current flowing in the channel.

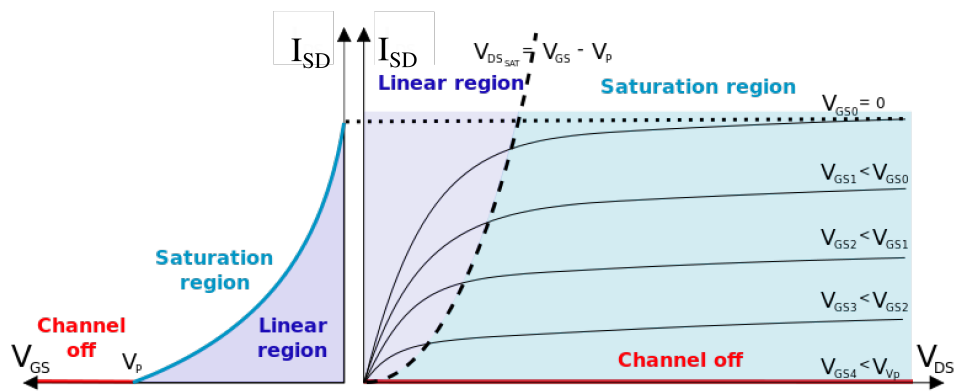


Figure 4.3: The operation of transistor is shown. The current I_{SD} as a function of gate voltage V_G is presented on the left. On the right we found different I_{SD} curves as a function of the source-drain voltage V_{SD} , for different gate voltages V_G . V_p represents the threshold voltage, under which the current does not flow (OFF state). The linear and the saturation region are underlined.

One of the solutions to this problem has been found in considering new materials able to satisfy the law of miniaturization. These new materials are represented, for example, by the class of 2D crystals. The advantages to use 2D materials come from the possibility to reduce the dimensions of devices, making them flexible and transparent; the fantastic properties coming from the reduction of the material dimensionality from 3D to 2D as the Dirac cone in graphene, direct gap of MoS₂ and so on, are extremely useful in electronic devices; furthermore, the problem related with the surface effect due to the presence of dangling bonds is avoided. However, there are some negative aspects related to the utilization of these 2D crystals. For example, at the beginning, graphene was acclaimed as the perfect material for high-performance transistors; in fact, already in 2007, only 3 years after its discovery, it was placed in the Emerging Research Devices chapter of the International Technology Roadmap for Semiconductors (ITRS), and the first transistor did not shrink to be built [105]. However, this euphoria is found to be not sustained in the short and medium term: graphene conquered the scientific community thanks to its large carrier mobility, a precondition for fast transistors, however, it does not present any bandgap, and a FET based on gapless channels can not switch off. Consequently, it is not fully suitable for logic circuits.

Many efforts have been done to open the gap of graphene, for example forming a narrow graphene nanoribbons, whose gap values are around 300–400 meV [106–108], meeting the target of the minimum estimated gap needed between 360 meV and 500 meV. However, nanoribbons of graphene are difficult to prepare with a defined width that brings at the good gap value. Also the bilayer graphene was included, but it is related with a reduction of the mobility [109, 110].

Due to the undesired effects connected to the gap opening of graphene, recently, the vdW heterostructures were considered to build a transistor. In particular, a vertical transistor composed by two graphene contacts separated by semiconductor or insulator layers was considered. The most important example is given by Britnell *et. al* [28] who built a transistor composed by two graphene layers separated by a thin Boron Nitride (BN) tunneling barrier. The current from one graphene layer to the other is a tunnel current through the BN barrier, led by the voltage between the graphene layers. The tunnel current is then controlled by the gate voltage applied between the Si wafer where the heterostructure is deposited and the closer graphene layer. Another important example of vertical FET is given by Georgiou *et al.* where the barrier between graphene layer is replaced by WS₂ layers [34]. Due to the smaller bandgap of WS₂ with respect to hBN and a specific position of the Fermi level in the gap, it is possible to have current transport by tunneling or thermionic emission.

Another kind of FET is given by the band-to-band Tunneling Vertical Transistors [111], where two semiconductors MoS₂ and WSe₂ are used in a dual-gate device architecture (two symmetric gates control independently the carrier concentration and the electric potential of the interface). In this system, characterized by a weak electrostatic screening, the band alignment is tuned thanks to a high gate coupling efficiency. Also, the contemporary lateral and vertical band-to-band tunneling in MoS₂/WSe₂ heterojunction were investigated

[112]. An interesting 3D-2D semiconductors junction characterized by strong doping given by substitutional dopants for the 3D component and by field effect in 2D crystal, provides a very good performance [113]. Finally a transistor completely dominated by vdW interaction in each part was realized and characterized [31], revealing a good performance operation. The in-plane transistor with 2D channel was also proposed in the last years, one for all characterized by MoS₂ channel [25] showing a very large mobility of MoS₂.

In this chapter we present a very simple model for field effect transistor bases on the graphene-MoS₂ interface, where the two monolayers are used as the source-drain electrodes [114]. Despite the used approximations and its simplicity, this model is able to reproduce the transistor operations, allowing the complete investigation of the electronic transport at the graphene-MoS₂ interface. At the center of our investigation there is the modification of the transport current between the electrodes when additional alternate layers of graphene and MoS₂ are stacked on top of them. In particular, we will focus on the current evaluation as a function of the gate voltage, for a fix source-drain potential, providing a comparison of the slope of the current curve and the ON/OFF ratio for all the studied heterostructures. We believe that this kind of study is necessary to define the possible role of the vertical van der Waals heterostructures in the new FET generation.

The electronic transport properties at the graphene-MoS₂ interface are obtained by means of Density Functional Theory (DFT) and non equilibrium Green's function formalism presented in chapter 2.

4.1 Graphene-MoS₂ interface for a FET modelization

In the framework of DFT, the study of big systems is limited by the size of the cell and the number of atoms. In transistor framework, if we imagine to include the metal contacts on the electrodes and the substrate to reproduce a real transistor with all its single component parts, the calculations would be too much expensive in time. Furthermore, due to the periodic boundary conditions in which the DFT code works, more complicated systems without in plane periodicity would be also too expensive or in some cases, impossible to calculate. The idea is, hence, to simplify the model, by considering only the interface where the electronic current is calculated and also an effective gate potential to avoid the inclusion of the dielectric substrate.

The choice of graphene and MoS₂ is explained: graphene is used because of the low DOS, that led to much greater increase of E_F with respect to conventional two-dimensional gas with parabolic dispersion [115–119] leading to a greater change of extra charge in graphene, responsible for the current. However, as it can be seen in Ref.[28], the absence of bandgap in graphene affects the performances of the transistor, due to the low ON/OFF ratio. In our model, the main idea is to combine the gap of MoS₂ with the graphene characteristics, using these two 2D crystals as electrodes. Therefore, the transverse current between graphene and MoS₂ electrodes, I_{SD} , is allowed by the voltage applied between the two layers, called the source-drain voltage V_{SD} , and it can be tuned or switched by means of a second voltage V_G on graphene. The gate voltage V_G is responsible for the rigid shift of the bands

of graphene with respect to the gap of MoS₂, simulated by applying the scissor operator on it, which represents the effective gate potential felt by graphene (normally reduced of ~ 100 times with respect to the real applied gate potential when a dielectric of 300nm of SiO₂ is placed between the gate and the electrode).

The scissor operator, discussed in 2.3, consists in an extra potential added to the sub-Hamiltonian written in localized orbital basis set of a system, in order to shift the electronic levels of the corresponding subsystem with respect to the rest of the system. It can be seen as an extra electric field applied to one subsystem. In the present case, we shift the electronic levels of the graphene monolayer with respect to the levels of MoS₂, in order to reproduce the effect of an electrostatic gate applied to the system. Since this operator is part of the Hamiltonian, the electronic density is correctly recalculated through the usual self-consistent process, and the charge transfer is correctly taken into account. This approximation works very well here due to the weak coupling between the 2D materials through vdW interaction.

In our calculations, the scissor operator has been applied only on graphene, by selecting the eigenorbitals $|\alpha(k)\rangle$ corresponding to carbon atoms. The initial shift given by $\Delta\alpha(k)$ is applied on the selected eigenorbitals (all the carbon orbitals) which build the graphene sub-Hamiltonian. This sub-Hamiltonian is part of the whole Hamiltonian over which the self-consistency is performed. Thus, the whole system reacts to the scissor and the whole electronic density is recalculated. In our specific case, when the selfconsistency is reached, the energy shift of the graphene eigenvalues with respect to MoS₂ is always lower than the applied $\Delta\alpha(k)$, as a consequence of the response of the system. In this work, we refer to the gate voltage as the value of $\Delta\alpha(k)$ applied on the graphene eigenorbitals. Thus, V_G and $\Delta\alpha(k)$ are the same value. Moreover, the value of $\Delta\alpha(k)$ is the same for all the eigenorbitals where it is applied.

The choice of MoS₂ as electrode has to be further explained: its intrinsic electronic band gap is here used to switch the current, and consequently, the transistor, from the OFF to the ON state. In fact, the transverse current I_{SD} occurs only if there are accessible states on both electrodes: in graphene, due to the Dirac cone, there are always available electrons (except at the Dirac point) for the current, whereas in MoS₂, due to gap, the current is possible only if we fall into CB or VB. In fact, for a specific range of V_G , the band alignment is such that the Fermi level falls in the gap of MoS₂ and the current is forbidden, in principle. For V_G out of this range, we move from the OFF to the ON state of the device, characterized by the Fermi level approaching the CB or VB of MoS₂, where there are accessible states and the current is allowed. In fact, the Fermi level approaching VB and CB leads to a charge transfer (Q) between graphene and MoS₂, or in other words to a charge redistribution between the planes, that is found to be at the basis of the device operation. We found that the Q curve as a function of V_G is strongly connected with the transport characteristics as the slope of $I_{SD}(V_G)$. However, there is a difference between this model and the real vertical tunneling transistors, since here we are considering an isolated system in which the total charge is zero and the current is given by the flowing of the charges already inside the system and separated by the gate voltage, whereas in 2D vertical transistor, extra charges are pumped on the graphene layer by means of the gate

voltage.

Our bricks to build the different heterostructure is composed by 4 MoS₂ and 7 graphene unit cells mutually rotated by 15 degrees. The choice of the 15 degrees rotation for the supercell is motivated by our results presented in chapter 3: any oriented supercell is equivalent from the global electronic transport point of view. The MoS₂ is optimized while graphene presents a small strain that, as we already shown, does not affect the electronic properties close to the Fermi level. Hence, we will use the smallest possible unit cell in order to reduce the calculation time, since we know that the orientation between the layers does not affect the electronic transport properties of the interface.

In the next section we will first analyze the characteristics of the simple graphene/MoS₂ heterostructure as a transistor and then, we stack additional layers forming further systems as graphene/MoS₂/graphene with V_G applied on the first graphene and on both, MoS₂/graphene/MoS₂ and graphene/MoS₂/graphene/MoS₂.

4.1.1 Band alignment in graphene/MoS₂ heterostructure

The effects of scissor on the band alignment in Fig.4.4 are explained below. Starting from the initial position, namely for $V_G = 0$ V, the Dirac point falls in the MoS₂ gap (at -0.6 V from the conductance band), and moves towards the conductance band (CB) as the voltage positively increases, or towards the valence band (VB) when V_G is negative. For positive gate voltages, the graphene bands shift to higher values: the Fermi level defined by graphene move towards the CB as it can be seen in Fig.4.4b. For more positive voltages $V'_G > V_G$, Fermi level moves on the CB and a migration of electrons from graphene to MoS₂ occurs (see Fig.4.4c), providing the accessible states for the current.

In the case of negative V_G , we have an opposite shift as it is shown in Fig.4.4d, with the Fermi level approaching the VB. Then, for more negative gate voltage $V'_G < V_G$, the Fermi level falls on CB and a migration of electrons from MoS₂ to graphene occurs. At this point, we found an almost similar, however symmetric, situation as for positive larger voltages (compare Fig.4.4c and Fig.4.4e). In the following sections we will refer to this migration of electrons from graphene to MoS₂ as the charge transfer Q on MoS₂ and vice versa.

In order to understand the mechanism of our transistor it is necessary to take a look at the band shift, by means of the DOS alignment for different V_G . First of all, we observe from the DOS that the shift as a function of V_G is not linear: when the Fermi level falls in the MoS₂ gap, an increase of the gate voltage of 1 V (from -0.3 V to +0.7 V in Fig.4.5b and Fig.4.5c) yields a shift of the BS of almost 0.7 V. On the other hand, when the Fermi level approaches the CB (or VB), the same V_G increased by 1 V causes a reduced shift since a charge transfer from graphene to MoS₂ (or from MoS₂ to graphene) occurs, which is more expensive in terms of energy with respect to moving the graphene bands in the gap. It means that, in order to reach the first electronic states in CB (VB) of MoS₂, and consequently the current saturation, we need an effective V_G which is larger than the value of the gap. This is the reason why we need to calculate the electric current for a range of V_G from -5 V to +5 V (larger than the gap of MoS₂). Note that when the Dirac point is in the gap, it defines the Fermi level, whereas when it is close to CB (VB), the charge

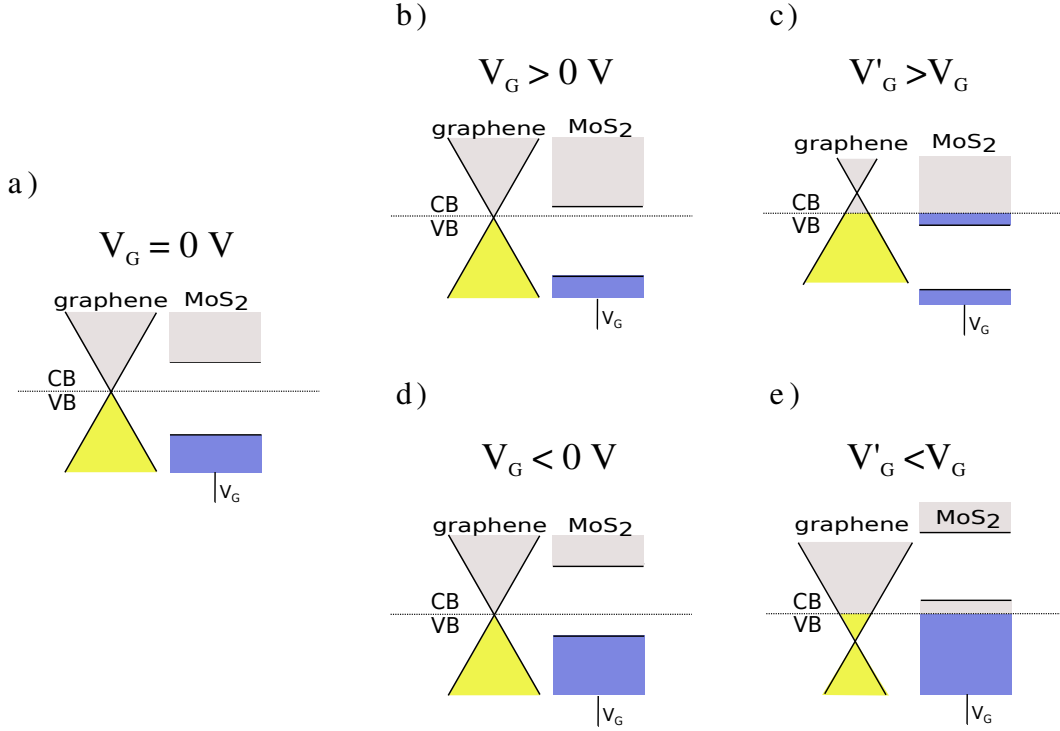


Figure 4.4: Band diagrams: alignment of graphene and MoS₂ Fermi electronic levels for positive and negative V_G , where the Dirac cone falls in the MoS₂ gap (panel b and c) and for larger absolute values V'_G where the the Dirac cone falls in the CB and VB, in panel d) and e), respectively.

transfer from graphene to MoS₂ (from MoS₂ to graphene) results in an electronic doping of graphene causing a displacement of the Fermi level from the Dirac point.

In the next part of this chapter, we will quantify the relative alignment of the bands, that can be seen as the position of the DOS of each electrode and additional layers with respect to the Fermi level, by calculating and comparing the evolution of the charge transfer Q as a function of V_G , since Q is proportional to the integral of the DOS.

4.1.2 Graphene/MoS₂ electronic transport properties

We now move to the quantitative evaluation of the charge transfer for graphene/MoS₂ by plotting the $Q(V_G)$ curve (see Fig.4.6a for the structure). As we said, the approach of the Fermi level to CB or VB leads to a charge transfer Q between the layers. In Fig.4.6b we plot Q at the interface as a function of V_G . This curve shows three regions characterized by linear behaviour with two different slopes. The plateau-like part (with smaller slope) coincides with the Fermi level moving in the MoS₂ gap, namely for a range of V_G of ~ 2 V, corresponding to the OFF state of the transistor (here we can still find finite $Q=0.18$ el/unit cell, even for $V_G=0$ V, coming from the interaction between the layers). Then,

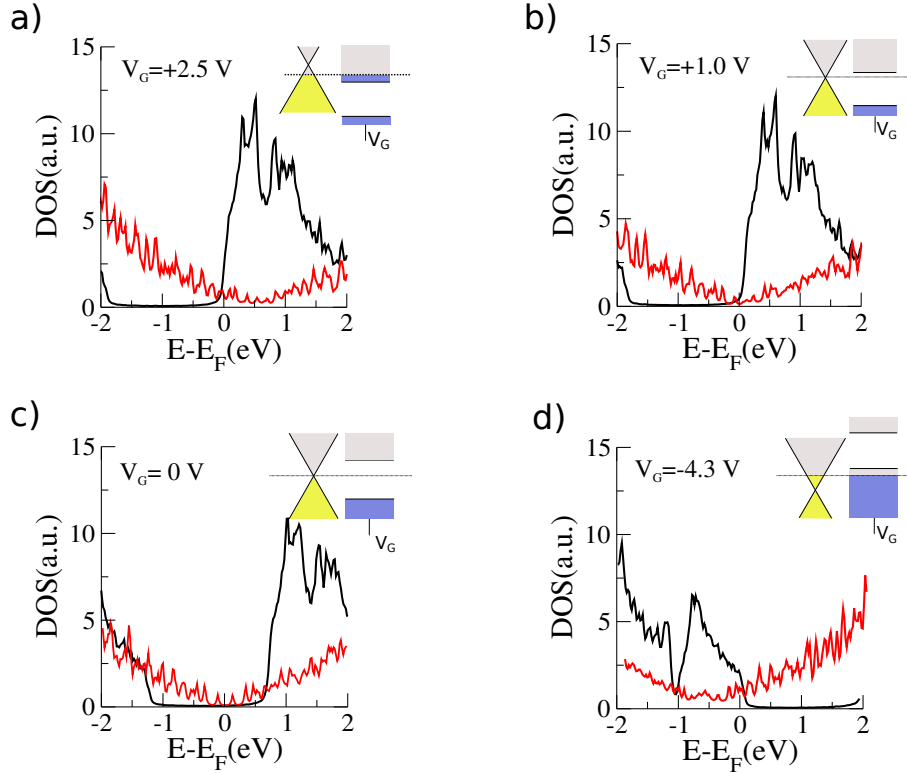


Figure 4.5: DOS and relative band alignment for different values of V_G . The red (black) line correspond to graphene (MoS₂) DOS.

right out of the OFF range of V_G , we found the very important part, called the junction region, defined as the range of V_G where the Q curve changes its slope from the OFF to the ON linear parts, occupying around 1 V: the change of slope does not suddenly occurs. For larger V_G , we recover the two second linear regions, for positive and negative voltages. We note that even in the OFF region, we have a charge transfer Q that leads to a non zero electronic density in the gap of MoS₂.

In Fig.4.6b we show the behaviour of $I_{SD}(V_{SD})$ calculated for a range of V_{SD} between -0.5V to +0.5V and for different V_G . For gate voltage $V_G = -1.0$ V, corresponding to the OFF state of the transistor, the current is very low, however, when the Dirac cone approaches VB (CB), for $V_G < -1.7$ V ($V_G > +0.3$ V), we observe an increase of the positive (negative) branch of the current curve for positive (negative) V_{SD} ; this corresponds to the ON state.

In Fig.4.6d the current $I_{SD}(V_G)$ for $V_{SD} = -0.1$ V is shown for a V_G range between -5V and +5V, corresponding to the range where the ON/OFF switch occurs. Again, in the OFF region around -1.5 and +0.5 V, we found very low current corresponding to the plateau in $Q(V_G)$, whereas in the ON region we can find two important parts: one is the increase of $I_{SD}(V_G)$, related to the change of Q slope, and the other one is the saturation of the current, for $V_G > 2.0$ V and $V_G < -3.0$ V, corresponding to the second linear region of Q . The main parameters we want to modify by stacking additional layer is the slope of $I_{SD}(V_G)$ and the ratio between the higher and lower current, called ON/OFF ratio, defining

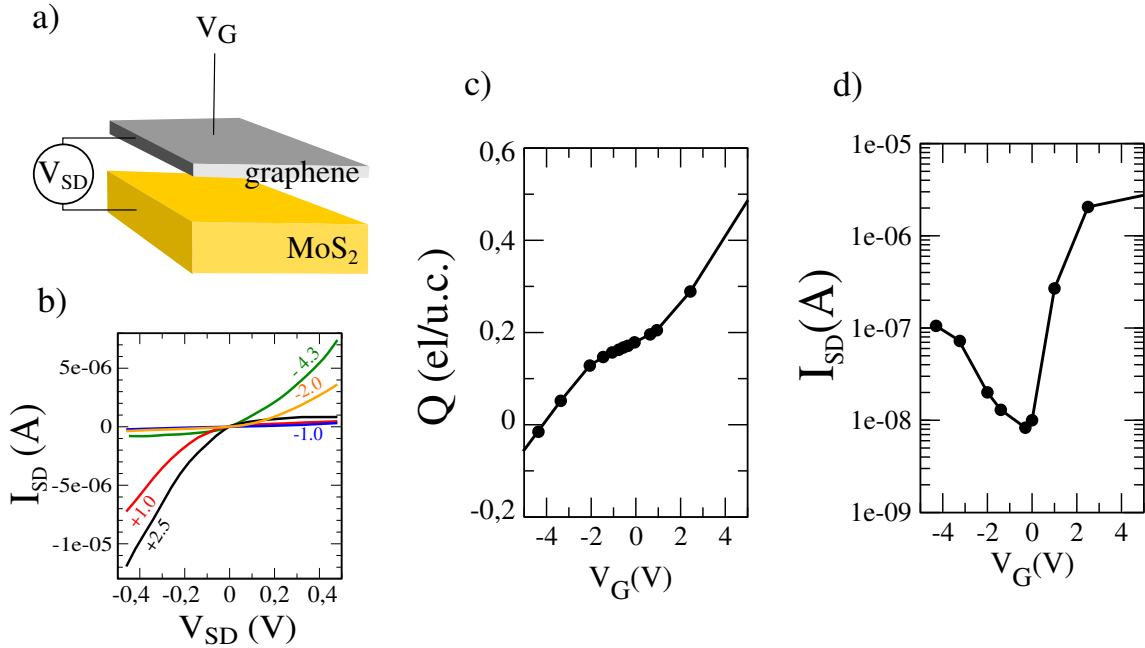


Figure 4.6: Graphic representation of the transistor model composed by graphene/MoS₂ heterostructure in a), charge transfer Q on graphene is represented in b). $I_{SD}(V_{SD})$ for different V_G in c) and $I_{SD}(V_G)$ for $V_{SD} = -0.1$ V in d) are shown.

how good the performance of the transistor is. In this work, the slope of $I_{SD}(V_G)$ is defined as the increase of the current curve in the V_G range from 0 V to +2 V, whereas the ON/OFF ratio is the ration between the current at $V_G = 5$ V and the current at $V_G = 0$ V. In this first configuration we found a slope of $\sim 2 \times 10^2$ and an ON/OFF ration of $\sim 2.4 \times 10^2$.

4.1.3 Adding graphene layer: graphene/MoS₂/graphene

Starting from graphene/MoS₂ heterostructure, we now stack an additional graphene, obtaining graphene1/MoS₂/graphene2 where, as previously, graphene1 and MoS₂ are the source and drain electrodes (see Fig.4.7a).

As we know from the previous chapter, the presence of the second graphene does not affect the electronic properties of the component layers, and so on of the electrodes, however, its presence modifies the band alignment. Also, the band alignment is strictly connected to the charge transfer Q , and as we will see, to the current as well. In Fig.4.7b we plot Q for each layer, in black, red and green lines for graphene1, MoS₂ and graphene2, respectively. The dashed lines correspond to the charge transfer on graphene in the original graphene/MoS₂ heterostructure.

We found that the charge transfer for all the three layers are very different from what we had before. The first difference is that Q varies less with respect to V_G than in the previous graphene/MoS₂ device, due to the presence of the second graphene layer. Furthermore,

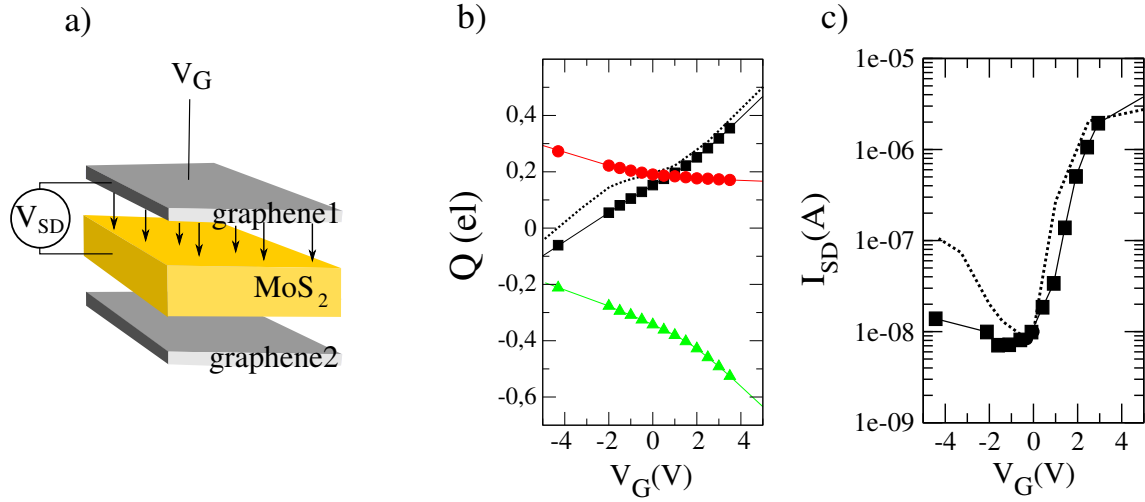


Figure 4.7: Graphic representation of the transistor model composed by graphene1/MoS₂/graphene2 heterostructure in a), charge transfer Q on graphene1, MoS₂ and graphene in black, red and green, respectively, is plotted in b). In c), $I_{SD}(V_G)$ for $V_{SD}=-0.1V$ is shown together with the current obtained in the first case, in solid and dashed line, respectively.

here, we do not have the three linear regions as before and Q on graphene1 has almost the same slope for all the V_G range. Looking at Q on MoS₂, however, we can recognize two region from $-5 V$ to $+0.5 V$ and from $+0.5 V$ to $+5.0 V$ characterized by small and very smooth change of slope.

The second graphene layer, even if it does not modify the electronic properties of the electrodes, as we demonstrated in chapter 3, is able to affect the band alignment, resulting in a different charge redistribution on the graphene1-MoS₂ interface.

The transverse current calculated at graphene1-MoS₂ interface, $I_{SD}(V_G)$, is represented in Fig.4.7c. The change of Q is reflected in the current behaviour: the OFF region seems to be larger, according to the absence of the third linear region in Q for negative V_G , and also for positive values, the increase of I_{SD} is slower than in the previous transistor, as Q slower increases.

In this configuration, the presence of the second graphene layer reduce the effect of V_G in the switching of the charge transfer curve from the OFF to the ON region. The junction region increases and, consequently, the current shows a smoother increase with respect to graphene/MoS₂, clearly visible since here it is necessary to apply a larger value of V_G of 1 V to recover the same current as in the previous graphene/MoS₂ system. It results in a worsening of the transistor parameter given by the slope of I_{SD} ($\sim 1.4 \times 10^2$). However, the ON/OFF ratio seems to be larger than in the previous case, being almost 10^3 ($\sim 2.8 \times 10^2$).

The idea is to try to increase the velocity of the band shift, that can be analyzed by looking at Q shape, in particular at the junction between the linear regions that should be as small as possible to lead to a faster increase of I_{SD} . In other words, we want the

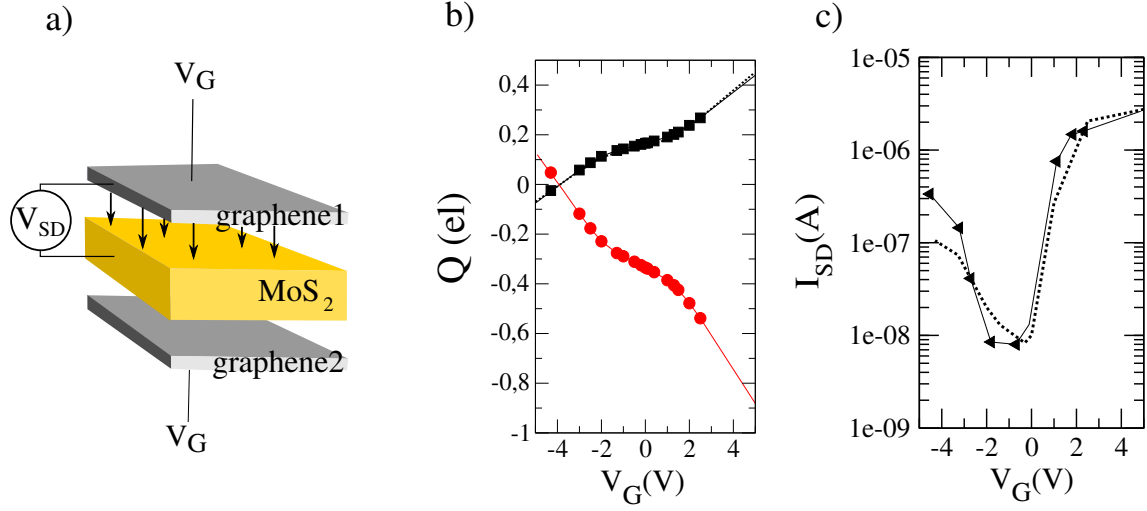


Figure 4.8: Graphic representation of the transistor model composed by graphene1/MoS₂/graphene2 with V_G applied on both graphene in a), charge transfer Q on graphene and MoS₂ (black and red line, respectively) is shown in b). In c), $I_{SD}(V_G)$ for $V_{SD}=-0.1$ V is shown together with the current obtained in the first case, in solid and dashed line, respectively.

Fermi level to move as fast as possible towards the CB or VB edges of MoS₂. We will try to achieve it by using the heterostructure and by applying the gate voltage on the two graphene layers.

Double gate on the two graphene layers

By considering the same heterostructure graphene1/MoS₂/graphene2 (Fig.4.8), it is possible to make something different: we apply the same gate voltage in both graphene layer in order to use also the second graphene as an active component, by shifting also its band. This is a symmetric system from the point of view of the band shift, composed by two distinct and equivalent interfaces: graphene1-MoS₂ and MoS₂-graphene2, being the first interface where the V_{SD} is applied and the current calculated. The symmetric configuration ensures that both graphene layers present the same alignment. The analysis of the charge transfer and the transport characteristics have been repeated in this new configuration and the results are presented in Fig.4.8.

First of all, we take a look at the charge transfer: obviously, we find the same Q curve on both graphene layers, as we expected from the symmetry of the system. Then, we notice that the Q curve corresponds to the one found on graphene in the first configuration (compare the black continuous and dashed lines in Fig.4.8b), revealing a kind of independence between the two graphene1/MoS₂ and MoS₂/graphene2 interfaces.

Here, the same V_G brings to doubled charge transfer on MoS₂ electrode, in both ON and OFF zones. However, the junction region is not thinner than in the previous case, meaning that the same range of V_G as in MoS₂/graphene is necessary to move from the

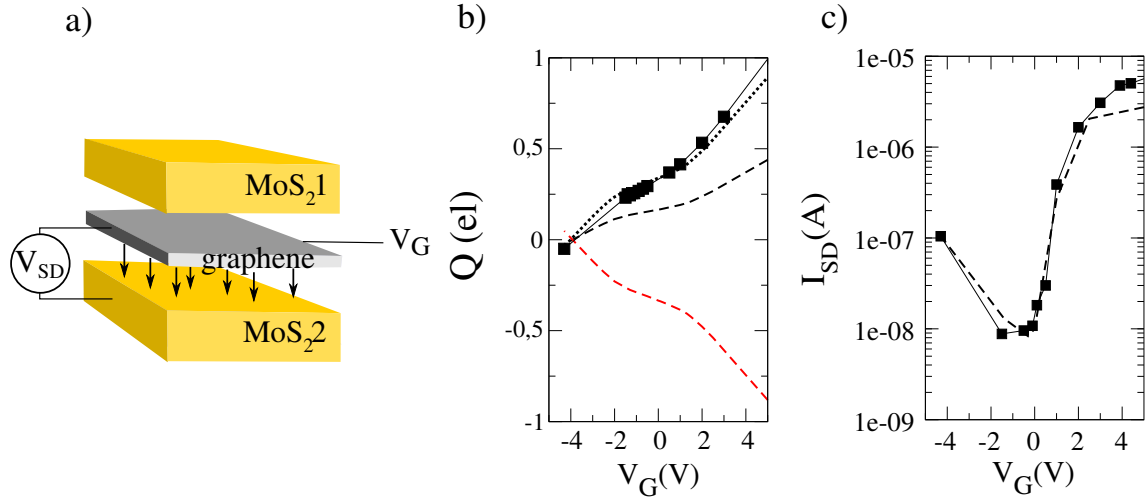


Figure 4.9: Graphic representation of the transistor model composed by MoS₂1/graphene/MoS₂2 is shown in a), the charge transfer Q on graphene (black and red line) is compared with the charge transfer obtained in the previous case (dashed lines) and its doubled value (dotted line) in b). In c), $I_{SD}(V_G)$ for $V_{SD}=-0.1V$ is shown together with the current obtained in the first case, in solid and dashed line, respectively.

OFF to the ON part. The consequence is that the increase of the current does not occur faster than before. For this reason, we do not expect an important improvement of I_{SD} with respect to the graphene/MoS₂ interface, as we can observe comparing the continuous and dashed lines in Fig.4.8c. We also notice that, as a consequence of the Q doubling on OFF and ON region, the ratio between the two slopes of Q curve calculated on MoS₂ characterizing the ON and OFF regions does not change.

4.1.4 MoS₂/graphene/MoS₂

According to the previous configurations, here we have another symmetric system composed by an additional layer of MoS₂ on the original graphene/MoS₂ interface. The complete structure, composed by MoS₂1/graphene/MoS₂2, is represented in Fig.4.9a. The electronic transport calculations have been performed on the second interface defined by the graphene-MoS₂2 layers.

This system represents essentially the inverse with respect to the previous one and the same argument regarding the band alignment and the charge transfer Q can be used here: hence, we expect to find an almost double charge on graphene electrode (instead of MoS₂) with respect to the first graphene/MoS₂ interface, since here it interacts with two MoS₂ layers and the interfaces are equivalent.

In Fig.4.9b we report Q on graphene for the first graphene/MoS₂ configuration, and the calculated double value, represented with the dashed and dotted line, respectively. The two curves are similar, even if here the ON and OFF regions are less clear than before. However, the slope of I_{SD} is not expected to change. On the other hand, we find

an improvement of I_{SD} in terms of ON/OFF ratio, probably related to the higher Q on graphene electrode, resulting in a larger value of the DOS at the Fermi level. With these last results, we can confirm that the two interfaces act as if they were independent one from each other, resulting in an almost doubled charge transfer on the electrode placed between two layers compared with the single graphene/MoS₂ interface. Now we just need the last example, in order to complete our analysis of the mechanism at the basis of the transport properties between two electrodes when the extra layers are added. In the next configuration we will double the charge transfer on both electrodes.

4.1.5 MoS₂/graphene/MoS₂/graphene

Considering the results of the previous cases, we now move to the last configuration: MoS₂1/graphene1/MoS₂2/graphene2 heterostructure with gate voltage applied on two graphene planes (Fig.4.10a). The electrodes are graphene1 and MoS₂2.

Following our idea, we do not expect any change of I_{SD} slope with respect to the previous configuration, except for a possible larger ON/OFF region given by larger Q on both electrodes and, consequently, a larger DOS at Fermi. Of course, we found the doubled Q on both electrodes as it can be seen in Fig.4.10b, where Q on graphene (black line) and Q on MoS₂ electrodes are shown and compared to the charge transfer in the simple graphene/MoS₂ configuration (dashed line). We confirm that the charge transfer between the layers can be evaluated by considering each interface independently from the others.

Also in this last case, we can relate the charge transfer (Fig.4.10b) and I_{SD} (Fig.4.10c). As we expect from the previous discussions, the slope of the current is not improved with the additional MoS₂ and graphene layers whereas we can find an improvement of the ON/OFF region.

The case of hBN/graphene/MoS₂ mixed heterostructure

In this small section we would like to show the possibility to predict the shape of the charge transfer Q on the intermediate layer in a mixed heterostructure, by considering separately the single interfaces and the charge transfer Q between them. Here we consider MoS₂/hBN/graphene heterostructure, that can be decomposed in two different interfaces, MoS₂/hBN and hBN/graphene represented in Fig.4.11a. Here we just compare the sum of the charge transfer Q on graphene calculated in the separated interfaces, 2) + 3), 2) and 3) in Fig.4.11b (the light and dark green for hBN-graphene and graphene-MoS₂, respectively), with Q on graphene calculated directly in the hBN/graphene/MoS₂ heterostructure (labeled with 1) in Fig.4.11b).

Comparing the sum of Q from the separated interfaces and that calculated in the hBN/graphene/MoS₂ heterostructure, 2) + 3) and 1) in Fig.4.11b, we find a good agreement in the shape of the curve, whereas we have a vertical shift of more or less 0.1 electrons. However, as we illustrated in the previous sections, the shape of Q , in particular the junction region and the ratio between the slopes in the ON and OFF linear region, are the

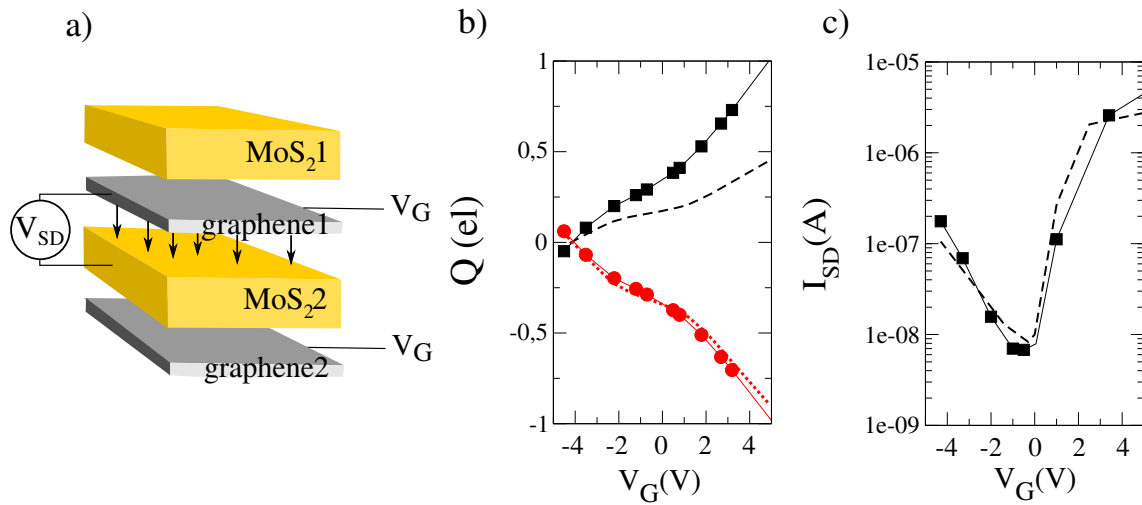


Figure 4.10: Graphic representation of the transistor model composed by MoS₂1/graphene1/MoS₂2/graphene2 is shown in a), the charge transfer Q on graphene1 and MoS₂ (black and red line, respectively) is compared with the charge transfer obtained in the first case (dashed lines) in b). In c), $I_{SD}(V_G)$ for $V_{SD}=-0.1V$ is shown together with the current obtained in the first case, in solid and dashed line, respectively.

most important parameters to characterize the current at the interface. From a computational point of view, the possibility to succeed in this kind of prevision separating the single interfaces, is important because it avoids the problem related to the building of the supercell considering the mismatch between three or more different 2D crystals.

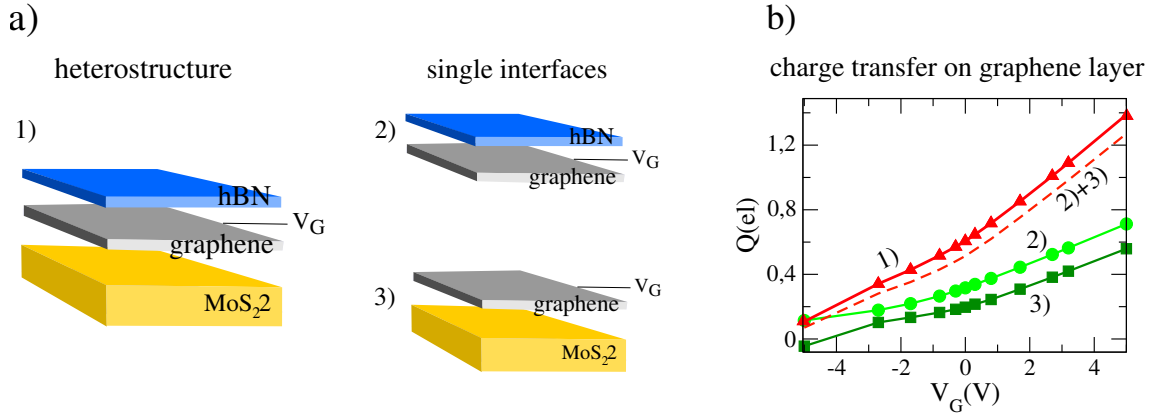


Figure 4.11: In a) the hBN/graphene/MoS₂ heterostructure labeled with 1). The 2) and 3) are the graphic representations of the single interfaces hBN/graphene and graphene/MoS₂. In b) we plot the charge transfer Q on graphene, calculated directly in 1) (red line) and as a sum of the Q calculated on graphene in the 2) and 3) interfaces (light and dark line respectively). The dashed red line is Q calculated as a sum of the charge transfer in the single interface 2) and 3).

4.2 hBN/graphene, the charge transfer depends on the DOS

At this point, after a complete description of the role of the additional layers in the electronic transport characteristics, we want to focus on the intrinsic parameters affecting the slope of $I_{SD}(V_G)$. We show here that the fundamental role is played by the shape of the DOS in the CB and VB edges. The way the DOS increases, since we do not have a perfect sharp band edge, is reflected on the charge transfer curve, in the junction region and then in the current slope. At the end, the slope ratio between the OFF and the ON Q region is a consequence of the DOS shape at the gap edges.

A simple test is performed on hBN/graphene heterostructure shown in Fig.4.12a). The hBN is not suitable in the role of electrode because of its very large band gap. However it provides a very clear example to demonstrate how the shape of the CB and VB edges affects the increase of the current. The switch of the charge transfer from the OFF to the ON linear region of hBN/graphene and graphene/MoS₂ (blue and red lines in Fig.4.12b), respectively) is underlined by the arrows. The slower switch in hBN/graphene leads to a larger junction region. Thus, we expect a smoother increase of I_{SD} curve compared to the current in graphene/MoS₂, as it is shown by the blue and the red lines, respectively, in Fig.4.12c). The slow increase of the charge transfer represented by the blue line in Fig.4.12b (and compared to the faster charge transfer in graphene/MoS₂ in red) determines a large junction region. Hence, we expect a smoother increase of I_{SD} curve compared to the current in graphene/MoS₂, represented by the blue and the red lines, respectively, in Fig.4.12c). The very slow increase of the charge and, consequently, of the current with respect to graphene/MoS₂ case, is related to a smoother CB edges of hBN (blue line in Fig.4.12d

around 1 and 2 eV) with respect to the one of MoS₂.

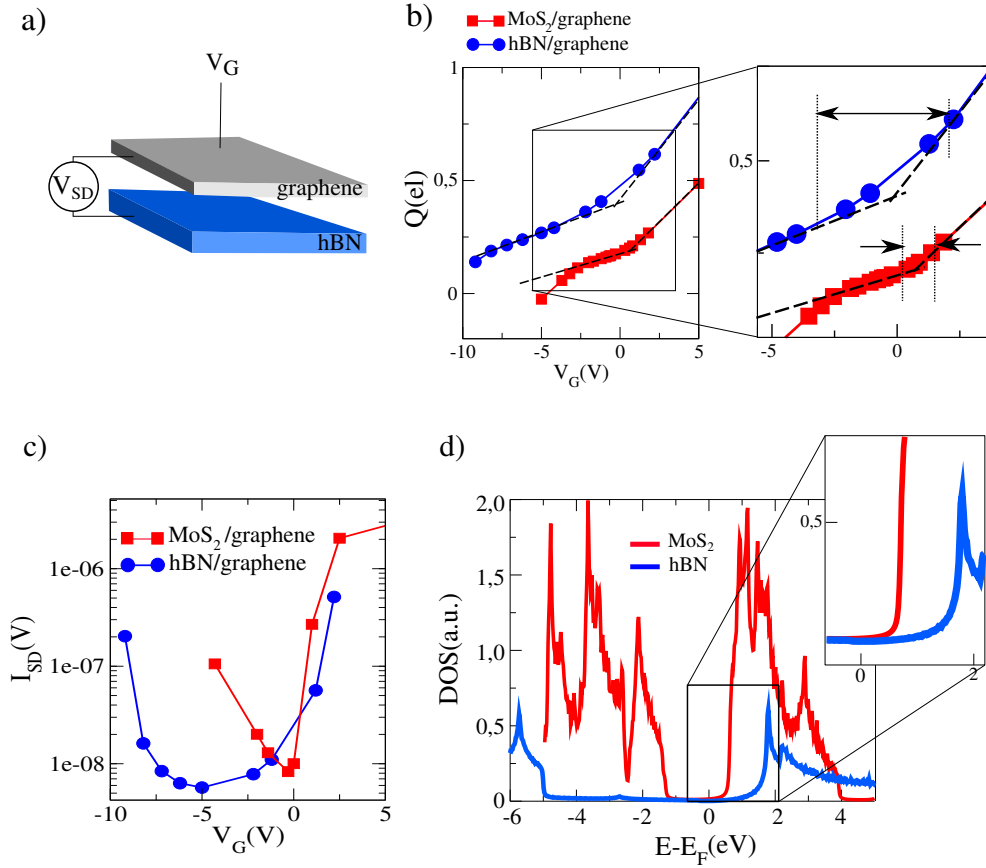


Figure 4.12: Graphic representation of the graphene/hBN interface is shown in a). In b) the charge transfer Q calculated on graphene layer for hBN/graphene (blue line) is compared to the one calculated on graphene in graphene/MoS₂ (red line). In c) the current calculated at the graphene/hBN interface as a function of V_G is described by the blue line, whereas the red line is the current corresponding to graphene/MoS₂, already shown in previous sections. In d) the comparison between the partial DOS of MoS₂ (red solid and dashed lines) and that of hBN (blue line). The CB edges shows different shape, smoother in hBN than in MoS₂, as shown in the inset.

4.3 Summary

So far, we have studied the mechanism at the basis of the graphene/MoS₂ transistor performance by observing and comparing the results coming from four heterostructures of alternate graphene and MoS₂ layers. In all these systems, we have chosen the graphene and MoS₂ electrodes where the electronic transport calculations were performed, and we have studied the influence of the additional layers on the performance of the transistors. We have focused our attention on the current modulation as a function of the gate voltage,

namely $I_{SD}(V_G)$, relating its behaviour to the charge transfer Q (and, consequently, to the band shift): we found that the width of the junction region is strictly related to the slope of $I_{SD}(V_G)$. The more the change of slope of the charge transfer from OFF to ON region fastly occurs, namely for small V_G range, the more $I_{SD}(V_G)$ will rapidly increase.

By stacking additional layers, it is possible to tune the effect of the gate voltage on the band shift and, consequently, on the charge transfer: we have seen that we are able to reduce the effect of V_G on the charge transfer and on the current just by adding an extra graphene layer non connected to the gate as in the first graphene1/MoS₂/graphene2, worsening the performance of the transistor; on the other hand, we can improve the V_G effect on the charge transfer on the electrodes, connecting also the second graphene to the gate potential. However, even if Q is doubled on the electrodes, the current does not switch faster, since nor the *velocity* of Q curve to move from the OFF to the ON region, neither the increased ratio of Q , namely the ratio between the ON and OFF region slope, change. By stacking additional layers, the current can at least show an increase of the ON/OFF ratio, probably due to more charges at the Fermi level, determining the current. We found that the heterostructures composed by alternate layers beyond the electrodes does not represent the way to really improve the transistor performance. Moreover, further additional planes beyond MoS₂/graphene/MoS₂/graphene do not affect the charge transfer on the electrodes, as a consequence of the interface independence. A very simple scheme of this characteristic is shown in Fig.4.13a.

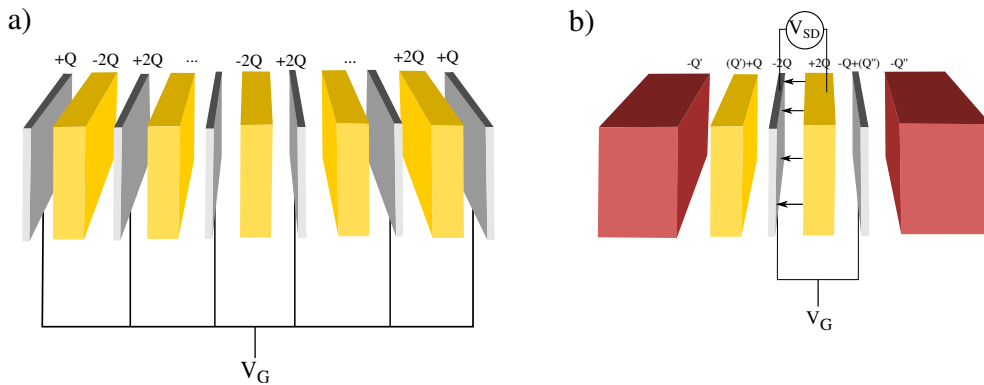


Figure 4.13: In a) is represented a sequence of alternate graphene-MoS₂ interfaces, with graphene layers connected to a gate voltage; the charge transfer between the layers is given by a succession of $+2Q$ and $-2Q$. It demonstrates that the charge transfer on the layers in the middle is affected just by the closer plane and the presence of the farther layers is negligible. In b) a scheme of the smallest heterostructure (MoS₂/graphene/MoS₂/graphene) that can be used to avoid the effect of the undesired charge transfer given by external layers (the red objects) on the electrodes given, in this representation, by the graphene and MoS₂ in the middle.

However, this kind of independence found in the vdW heterostructures interfaces when the alternate graphene layers are connected to the gate, can be useful if we want to avoid the charge dispersion on the electrodes. One possible structure is represented in Fig.4.13b:

if we add extra vdW layers on top and bottom of MoS₂1/graphene1/MoS₂2/graphene2, as the copper in the transistor, for instance, the charge transfer necessarily present at the external interfaces does not affect the charge transfer and consequently the electronic transport between the electrodes.

Moreover, the independence of the interfaces can also be used to study the heterostructures composed by more than two different crystals like, for example, hBN/graphene/MoS₂. The possibility to separate the two interfaces allows us to avoid the computational problem of the lattice mismatch between three crystals and to build and analyze even different supercells with different size for each interface. For example, it can be possible to study, in the framework of DFT, transistors with a more complex structure, made by vertical stacking of 2D crystals, just by considering separately each interface.

We can conclude by saying that the mixed vertical heterostructures composed by more than two different crystals are not useful to improve the performance of transistor, whereas the choice of the semiconductor with a sharp band edge is more important to increase the current slope for a fast switching device.

Chapter 5

Defects on MoS₂: detection by graphene tip

In the previous chapter we modeled a transistor made by vertical stacking of graphene and MoS₂ monolayers, by focusing the attention on the charge transfer between the planes, resulting from the band alignment modulated by gate voltage. In our model, as already stressed, we consider infinite planes of graphene and MoS₂, without edges or impurities, and the electronic transport and properties of graphene and MoS₂ come from an ideal system. However, defected crystals are frequently produced in experiments and it is impossible to work with defect-free or impurity-free materials: as well as the edges effect already discussed in Sec.3.4, the presence of impurities and defects in crystals can strongly modify the properties of each layer and affect the transport characteristics at the interface. Hence, it is strictly necessary to take into account the role of defects since they can induce, in the case of electronic devices, worst operation performance or failure. In manufacturing industry, such as the micro- and nano-electronics, the process of collecting and analyzing data to determine the causes of failure, called failure analysis, is strictly necessary at every step of a product life cycle.

5.1 Introduction to defects on MoS₂ and their characterization

The characterization of defects goes through the structural deformation analysis and the study of its effects on the properties of the material. Sometimes the presence of defects can improve some specific characteristics of the materials thanks to the doping effect coming from impurity. Defects on graphene were extensively studied and all the recent results are reported in [120]: the defects, sometimes found to enrich the graphene functionality, are analyzed taking into account their effects on chemical, electronic, magnetic and mechanical properties. Defected TMDC have been largely investigated as well [121], as we will see in the state of art section.

The detection of defects can be done using STM, representing a non-destructive technique and an efficient tool to explore the electronic structure in each point of the surface. It gives the possibility to analyze the changes in the images pattern of the ideal substrate leading to the classification of the more frequent defects. On this respect, many works can be found in the literature showing STM measurements over a single or several MoS₂ layers [122–129].

As well as STM, another used technique is the Atomic Force Microscopy (AFM). AFM is characterized by a sharp tip, fixed at the free end of a cantilever, scanning the sample surface by means of the interaction existing between the probe tip and the sample surface. This interaction causes the cantilever deflection and by means of a laser beam, focused on the tip head and scattered toward a photodiode detector, the cantilever displacements during the scans are continuously monitored and the forces acting between the tip and the sample are measured.

In this chapter we present the analysis of the defects in MoS₂ monolayers by using graphene tip for both STM and AFM simulations. In particular, the characterization of some MoS₂ point defects is done by analyzing the conductance and force given by STM and AFM measurement respectively, considering a graphene tip and a standard Cu tip. The low reactivity of the graphene tip is demonstrated, as a consequence of the weak vdW forces mediating the tip-MoS₂ interaction. In fact, even for short distances where the Cu tip-sample interaction is characterized by chemical bonds and the risk of tip-sample atomic transfer appears, the graphene tip ensures a more stable AFM measurement.

The results presented here were obtained in collaboration with Cesar González, from Department of Theoretical Condensed Matter Physics & Condensed Matter Physics Center (IFIMAC), Facultad de Ciencias, Universidad Autónoma de Madrid, and published in Ref.[130]. Here we present an exhaustive *ab initio* analysis on clean and defective MoS₂ in order to fully describe the potential use of a graphene-based tip in non-contact (nc)-AFM. The detailed overview of the estimated forces is complemented by a full analysis of electronic transport on each site. For that purpose, the evolution of the conductance with the tip distance over each site has been simulated, as well as the theoretical STM images. The results are compared to the values obtained with a standard metallic Cu tip, showing the potential use of the graphene-based tip for combined STM/AFM measurements.

In the following we provide state of art on the previous experimental and theoretical studies on defected MoS₂ using metal and graphitic-like tips. Then we will detail the used tips, and the sample given by pristine and defected MoS₂ monolayer with four different defects, and the calculation details in terms of parameters and procedures.

5.1.1 State of art

Initially, the S and Mo vacancies in MoS₂ were studied using DFT by Noh *et al.*, [131], where a careful analysis of Scanning Transmission Electron Microscopy (STEM) measurements, different kind of defects (both vacancies and antisites) were considered in order to explain the features obtained in the experiments [132, 133]. However, the structural analysis of defects was insufficient and a subsequent study of the semiconductor or metallic

character of the defective MoS₂ required a systematic STM investigation [124–129]. Recently, González *et al.* provide an improvement in the characterization of a great collection of point defects, considering both S and Mo vacancies together with their corresponding substitutional atoms [134], using a more accurate Keldysh-Green’s functions formalism for STM images calculations. In parallel, a theoretical investigation of defective MoS₂ using *ab initio* simulations of AFM was also published [135] providing an analysis of the forces curve from long distances to the contact regime, calculated over each defect, comparing the highly reactive copper tip and a less reactive semiconducting silicon tip. The results are the followings: the attractive force between the tip and the sample strongly depends on the nature of the tip; the second result concerns the important reactivity of the defective monolayer (both of them will be discussed in the next section for Cu and graphene tip comparison). Furthermore, the cited results were confirmed with the physisorption or dissociation of different molecules on selected defects [136–144].

Regarding the graphitic tips, some years ago, Castellanos-Gomez *et al* used carbon fiber tips to form molecular junctions [145, 146], implanted on quartz tuning fork force sensor able to make simultaneous STM/AFM measurements. In a first step, their potential use on a gold surface was obtained and later, the carbon-based tip was approached at the contact regime to an organic molecule previously deposited over a conducting surface.

Then, Dappe *et al* and González *et al* proposed a graphitic-like tip for STM simulations as well as an electrode in a molecular contact [147, 148]. The demonstrated atomic resolution showed its potential use for STM measurements. Moreover, with respect to the contact formed between the metallic electrodes and the sample, the electronic current for graphitic-like tip is much lower, making possible the measurement on more fragile sample as molecules. The absence of chemical bonds between the tip and the sample, reveals the low reactivity of this tip and prevents the formation of plateaus, characteristic in the metallic contact. This property justifies the interest for this kind of low interacting contacts.

Contrarily to STM, the MoS₂ monolayer has not been deeply studied with the AFM technique. In most of the measurements, AFM results have been used essentially to test the quality and the number of layers obtained during the MoS₂ synthesis [149–152]. In a recent work, the atomic resolution was obtained on a similar material, the MoSe₂ monolayer [153], while an analysis of the defects on MoS₂ has been performed combining noise-current analysis with AFM [154].

5.1.2 Calculation parameters

The study here presented on the detection of defects in MoS₂ monolayer have been performed within the DFT methodology, by using both Fireball and plane wave Vienna Ab initio Simulation Package (VASP). The structural optimizations were performed by C. González with VASP [155–157], using the following calculation parameters: regarding the exchange and correlation potential, the functional used is GGA within the Perdew, Burke and Ernzerhof (PBE) approach [158, 159], combined with Projector Augmented Wave (PAW) method; the k-points in the first BZ and the energy cutoff are 4 and 400 eV, respectively; the force threshold for the convergence used is 0.02 eV/Å. In order to

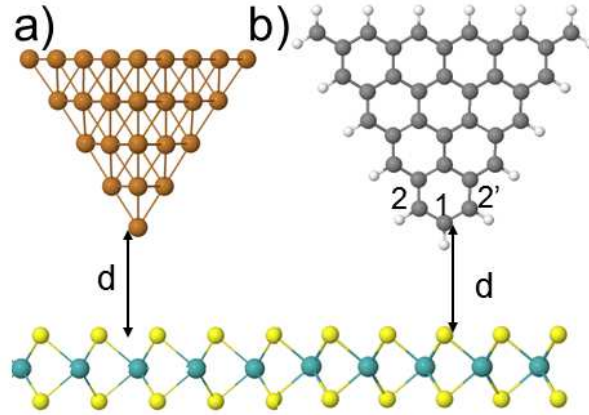


Figure 5.1: Lateral view of the atomic structure for a) a Cu tip and b) a graphene-like tip over a pristine single layer of MoS_2 . The yellow/blue/brown/grey/white spheres represent the S/Mo/Cu/C/H atoms, respectively. The initial distance is defined for each tip.

consider the vdW interactions between the graphene-tip and the sample, the Grimme's parametrization implemented in VASP has been used [160].

Here we considered four different defects configuration: a S and Mo vacancy, one Mo substitutional atom on a single S-vacancy and two Mo atoms occupying a S-divacancy. For each case, a supercell composed by 6×4 unit cell, formed by 72 atoms, was built. All the information related to the atomic and electronic structure of these defective MoS_2 structures can be found in a previous study provided by González *et al.* [134].

In order to completely analyze the performance in defect detection of graphene-tip, we performed the same calculations for a Cu tip as well. The graphene-like tip is formed by a ribbon of 35 C atoms saturated by 17 H atoms, whereas the Cu tip has a pyramid-like structure composed by 35 atoms oriented in the (111) direction (the atomic configurations of both tip are shown in Fig.5.1 a) and b) respectively).

The positions of the tip with respect to the sample are the followings: over S and Mo atoms for the pristine case, over the defects in the other configurations. For each configuration, the atomic optimization is done starting from the initial position where the distance between the last Cu or C and upper S plane is 5.0 \AA and 5.5 \AA respectively, and then rigidly approaching the tip of 0.25 \AA each time. For all the cases only the first Cu or C atoms and the lower S plane are fixed.

At the end of the structural optimization, the conductance calculations, the STM images and the DOS, calculated only in some specific cases, are simulated with the Fireball code. For MoS_2 and graphene, the same basis set as in the rest of this work are used, while for Cu (H) the cutoff radius are the following: $r_s=4.50 \text{ a.u.}$ $r_p=5.70 \text{ a.u.}$ $r_d=3.70 \text{ a.u.}$ ($r_s=3.80 \text{ a.u.}$).

Using the Hamiltonian calculated within the Fireball methodology, the electronic current can be estimated following the non-equilibrium Green's functions technique, as dis-

cussed in the second chapter.

5.2 STM images simulated with the graphene tip

First of all we report the calculated STM images using graphene tip. As we can see from Fig.5.2, the graphene tip is able to provide atomic resolution in the MoS₂ monolayer sample. Before describing the STM images, we first analyze the structure of graphene-tip and its peculiar DOS: the last C atom labeled with 1 in Fig.5.1 does not contribute to the tunneling current since it presents a large gap of 5.0 eV around the Fermi level (see the peak labeled with 1 in Fig.5.2, left panel), whereas the C atoms labeled with 2 and 2' are characterized to have a semi-occupied p-like state at the Fermi level perpendicular to the graphene plane (see the central peak in Fig.5.2, left panel)[148]. In Fig.5.2a we report the simulated STM images for bias voltage of -0.1 V, corresponding to higher states in the valence band of p-semiconductor: the maximum of the current is found close to S atoms, and a triangular pattern is obtained (the position of the tip over a maximum point has been indicated with grey spheres). At this site, the p-states of the C atoms maximize the current established with the surrounding S atoms from the monolayer. Additionally, the corrugation has been estimated at a tip-S distance of 4.0 Å yielding values of 0.15 Å and 0.05 Å using the graphene-based and Cu tips respectively. We can conclude that the graphene tip provides larger atomic resolution than a conventional metallic Cu tip on a MoS₂ monolayer as obtained before on a graphene sheet [148]. The fact that the S atoms give more contribution in tunneling current is not surprising since, even if the DOS related to the S atoms is lower than Mo DOS, the S atoms are located closer to the tip. In Fig.5.2b the applied bias voltage is +1.9 V, exploring the empty states in the conduction band of MoS₂ sample and the pattern reveals an asymmetric hexagon. The brighter zone are displaced from the S atom and they have another shape with respect to the previous case. In panels c) and d), we come back to the bias of -0.1 V, however the orientation of the tip is modified, with an angle of 15 deg and 30 deg, respectively, with respect to the *z* axis. Here we can find the differences between the panel a) and b) of Fig.5.2 directly related to the different orientations of the p-states of the tip and the changes in the coupling with the S atoms in the monolayer. For STM standard distances (between 4.0 and 6.0 Å), our simulations show that the first geometry (the so-called 0 degrees) leads to a more stable configuration. For this reason, the rest of the STM simulations (and even the AFM calculations of the following subsections) will be performed with this tip orientation.

We turn now our attention to some selected defects: the S vacancy, the Mo vacancy, the substitutional Mo atom in a S vacancy and two substitutional Mo atoms in a S divacancy. The simulated STM images are shown in Figure 5.3 for $V=+1.9$ V in order to include the effect in the electronic current of all the new states appearing in the MoS₂ gap due to the inclusion of the defects. Using this voltage, a comparison to previous results calculated with a metallic tip can be again established [134]. The S vacancy (panel a)) breaks the zigzag symmetry of the pristine monolayer, leading to some brighter spots around it. This result mimics the depression obtained in previous experimental and theoretical works [122, 127].

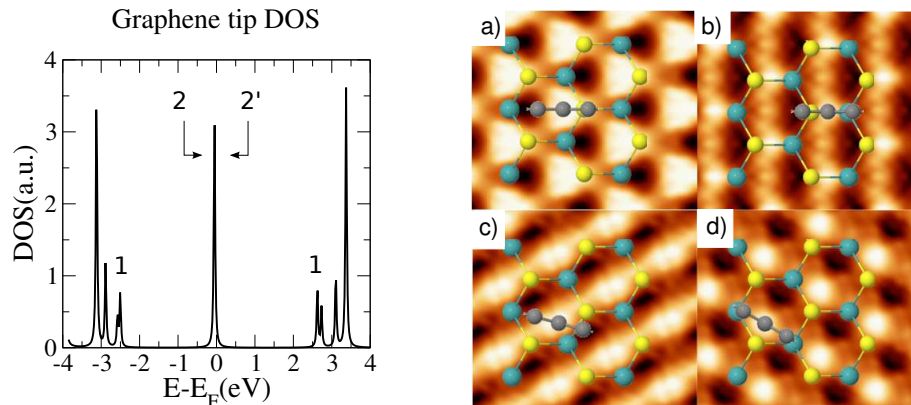


Figure 5.2: On the left panel, the DOS for graphene tip calculated with fireball: the peak at Fermi energy is given by the lateral C atoms (2 and 2'), whereas the peak at ± 2.5 eV are given by the last carbon atom (1). On the right, calculated STM images on a pristine MoS_2 monolayer using a graphene-like tip: a) $V = -0.1$ V, b) $V = +1.9$ V, c) $V = -0.1$ V with the tip rotated 15 degrees and d) $V = -0.1$ V and the tip rotated 30 degrees. A ball and stick model is superimposed. The three grey circles correspond to the last three C atoms of the tip, showing its orientation in the simulation. The STM images have been graphed using the WSxM software [161] and provided by C. González.

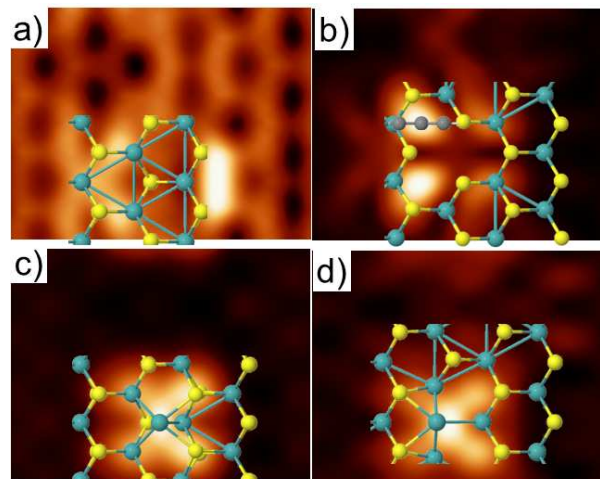


Figure 5.3: Calculated STM images at +1.9 V with a graphene-like tip for a) S vacancy, b) Mo vacancy, c) one substitutional Mo atom occupying a S vacancy and d) two substitutional Mo atoms on a S divacancy. The corresponding atomic configurations of the MoS_2 defects are superimposed. The grey spheres in b) indicate the orientation of the tip. The STM images have been graphed using the WSxM software [161] provided by C. González.

Also the asymmetric image is again related to the orientation of the tip which is convoluted with the electronic density of the atoms around the S vacancy. In the other three cases (Figures 5.3 b)-d)), the results change from the data previously obtained with a metallic tip (see the images in reference [134]). In the Mo vacancy, the image shows four asymmetric maxima at each side of the defect instead of the three very symmetric protrusions, obtained close to the neighboring S atoms with the metallic tip. Now, with the graphene-like tip, the current is maximized at the site where the C atoms with the half-filled p state can interact with the dangling bonds of the S atom originally bonded to the absent Mo atom. In the left side, both C atoms can be coupled with any state of the surrounding S atoms, while on the right side the interaction can involve only one C atom. In the two substitutional cases, the maximum, originally obtained over the topmost Mo atoms with the metallic tip, has been displaced. In fact, the maximum is splitted in several spots showing the different sites where the p_y-orbitals of the C atoms can be coupled to d-orbitals of the substitutional Mo atoms.

5.3 Tip approach pristine and defected MoS₂ monolayer

In this section we will analyze the force and conductance results of graphene tip on pristine and defected MoS₂ and we compare them to the Cu tip results. We will start with the pristine MoS₂, then we move to the missing Mo and S atoms, and finally we consider the substitutional Mo atoms in mono- and di- S vacancy.

5.3.1 Pristine monolayer

Here we consider the pristine MoS₂. The results shown in Fig.5.4 have been calculated over a S atom (green squares) and a Mo atom (blue circles). By looking at the forces minima (Fig.5.4a and Fig.5.4b for graphene and Cu tips respectively) we can deduce that the interaction between graphene-tip and the sample is ruled by vdW interaction, their values are -0.14 nN and -0.19 nN over the S and Mo atom respectively, one order of magnitude lower than in the Cu-tip case. At the force minimum, no bonds are formed between the atoms from the graphene tip and the monolayer (see the insets in panels a) and c) for the case of Mo and S respectively) while several bonds can be formed with the Cu tip (as it is shown in the insets of panels b) and d)) due to the strong interaction established between the apex and the S atoms in the monolayer.

The minimum appears at similar last tip atom-S distances for both tips, even if the force origin between the sample and the two tips presents a great difference. In fact, for both tips, the force minimum over Mo atoms is located at lower distance with respect to the S site, due to the lower position of the Mo plane. Regarding the graphene-tip, the non isotropic shape and the short distance of the second C-layer (only 0.7 Å far away) lead to a slight increase of the minimum force over the Mo atom than over the S site.

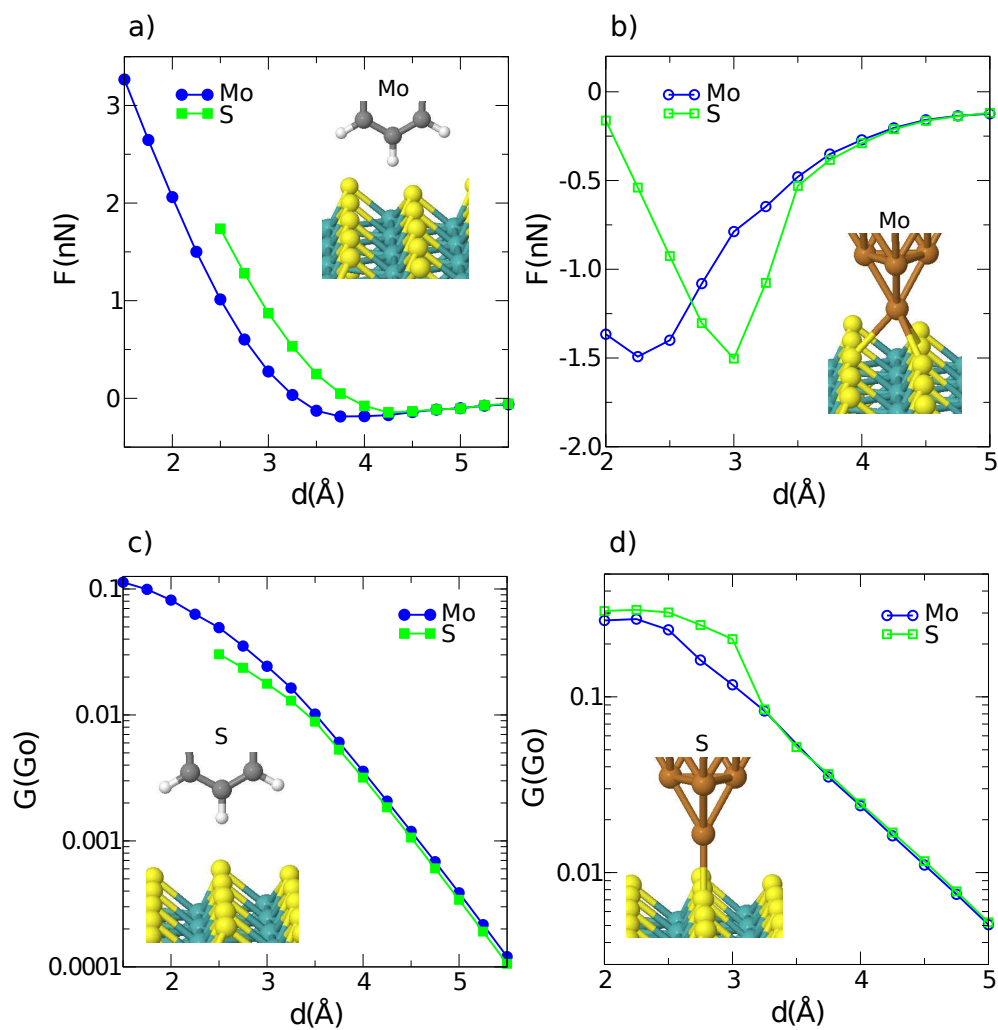


Figure 5.4: a) Force and c) conductance curves on the S (green squares) and Mo (blue triangles) atoms calculated with a graphene tip; b) and d) the same for a Cu tip. The conductance-axis is in logarithmic scale. In the insets the atomic structure of the minimum force on the four cases. The yellow/blue/brown/grey/white spheres represent the S/Mo/Cu/C/H atoms.

Due to the absence of dangling bonds in graphene tip and MoS₂ atoms in the attractive regime, neither the tip nor the MoS₂ has been deformed. In the repulsive regime, however, the tip produces a great deformation on the MoS₂ monolayer, suggesting the lower flexibility of the substrate.

On the other hand, the Cu tip presents a strong deformation at the contact point, illustrated by the displacement over S and Mo atoms of 0.25 and 0.20 Å, respectively. The Cu tip results also to be softer than graphene tip. Another consequence of the lack of dangling bonds in graphene-tip is that the conductance monotonically grows over both sites (see Figure 5.4 c)) even for distances closer to the force minima. Below the tunneling regime (see the straight line in the logarithmic scale), the curve evolves to a final saturation associated to the multiple scattering effect. Notice that no plateau is formed as expected for metallic contacts. In graphene tip, the conductance at the Mo site is slightly larger than over the S atom, however it is explained also looking at the STM images where the maximum current values are displaced from the atomic sites. In general, for graphene tip, the conductance is lower than for the Cu tip, except for short distances where they become comparable.

For Cu tip, the conductance grows until the contact, where the plateau is formed, as we can see in Fig.5.4d. The conductance plateau occurs at around 3.5 Å over the S atom, meanwhile it still grows for the Mo atom since the contact is formed deeper in the tip approach (at 2.5 Å). Altibelli *et al* [162] suggested that at low distances there can be a contrast change, leading to a larger value over the Mo atom. Our results seem to be in contradiction with this idea because the conductance is larger over the S atoms at all the distances evaluated. The different behaviour can be explained with the inclusion of the atomic relaxation and the electronic reconfiguration that our conductance simulations take into account.

5.3.2 S and Mo vacancy

The cases of S and Mo vacancies can be approached using the same analysis as in the pristine MoS₂. The force and conductance curves are shown in Fig.5.5 for both graphene and Cu tips. As in the previous case, the forces between the Cu tip and the sample is lower than in graphene case, however here the minima on both vacancies are found almost at the same distance with the Cu tip (at 2.00 Å), contrary to what happens for graphene where the minimum is obtained at different heights (at 3.00 and 3.75 Å for S and Mo vacancy, respectively). Again this result is linked to the atomic configuration of the tip: as previously mentioned, the C2 atoms are only 0.70 Å above the last C atom while the second layer of Cu is placed at around 2.00 Å above the apex: it means that for graphene tip, the C2 atoms can interact with S atoms close to the Mo vacancy, whereas in Cu tip the second Cu layer is too far.

On the S vacancy, the C2 atoms can fall on the Mo sites placed in their sublayer more than 1.50 Å below, allowing a slightly larger attraction (-0.50 nN) at shorter distances compared to the Mo vacancy case. Furthermore, the graphene tip leads to a minimum of -0.31 nN in both S and Mo vacancy sites, which represents a difference with the Cu tip,

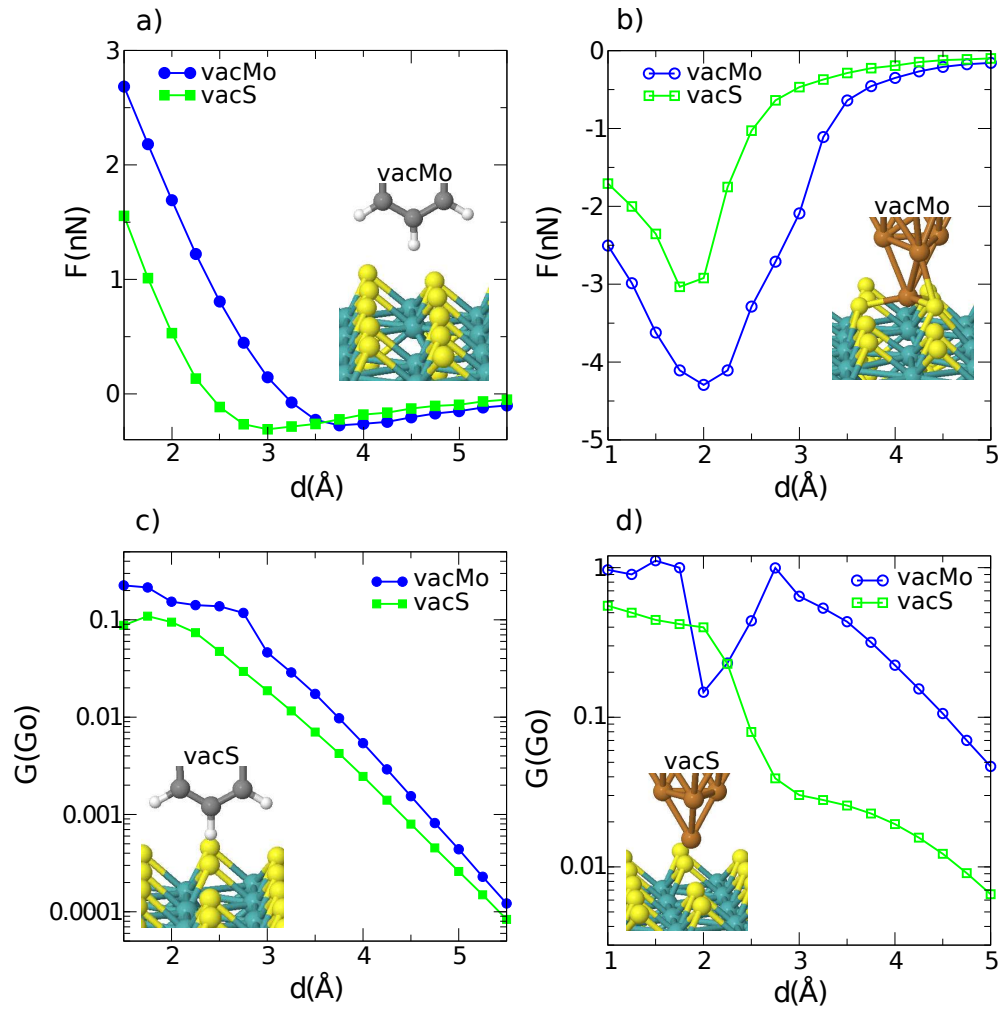


Figure 5.5: a) Force and c) conductance curves on the S (green squares) and Mo (blue triangles) vacancies calculated with a graphene tip; b) and d) the same for a Cu tip. The conductance-axis is in logarithmic scale. In the insets the corresponding atomic structure of the minimum force on the four cases. The yellow/blue/brown/grey/white spheres represent the S/Mo/Cu/C/H atoms.

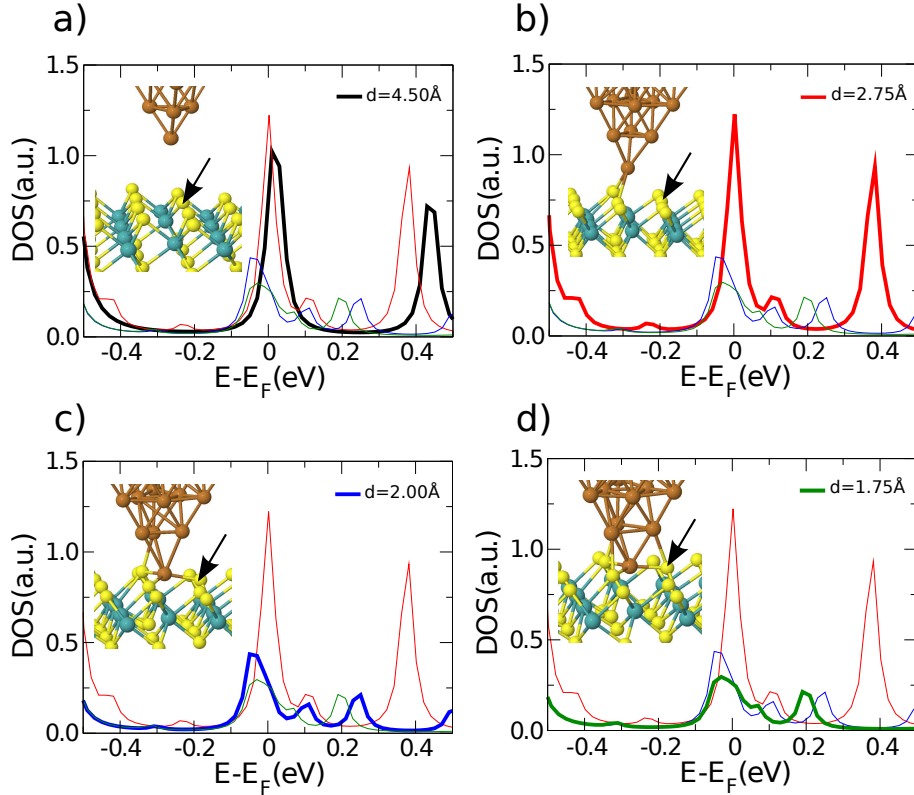


Figure 5.6: Electronic DOS of the S atom indicated with an arrow in the atomic structure of the inset. The DOS have been calculated at different distances in the Mo vacancy case contacted by a Cu tip. In each panel, the highlighted line corresponds to the DOS at the indicated distance: a) black line at 4.00 Å, b) red line at 2.75 Å, c) blue line at 2.00 Å and d) green line at 1.75 Å.

where the interaction between the tip and the sample gives different force minimum values. In both graphene and Cu tip there is a force growth, however larger in Cu tip (from -1.50 to -4.30 nN and from -1.50 to -3.00 nN for Mo and S vacancy respectively) due to the strong covalent bonds formed between the apex and the surrounding atoms, S atoms on the Mo vacancy and Mo atoms on the S vacancy (see the atomic models in the insets of Fig.5.5).

As in the previous case, the conductance curves, Fig.5.5c and Fig.5.5d for the graphene and Cu tips respectively, the values are much larger for the Cu tip. Regarding the graphene tip, even though we are considering vacancies in MoS₂, the behaviour of the conductance remains very similar, indeed, no bond is formed between the tip and the atoms of the vacancies and consequently the conductance remains in the tunneling regime, as indicated in Fig.5.5c. For close distances, the conductance saturates due to the multiple scattering effect. For all the distances, the value is larger over the Mo vacancy.

Using the Cu tip, the conductance curves show completely different characteristics (Fig.5.5 d). In the Mo vacancy, we can observe the standard tunneling regime behaviour

until a tip-MoS₂ distance of 2.75 Å, with the beginning of a jump to contact between 3.00 and 2.75 Å. At this point, a sudden decrease, from 1.00 G₀ to 0.15 G₀ at 2.00 Å, is obtained, instead of an expected plateau. After the decrease, for shorter distances, the conductance increases again until about 1.00 G₀, yielding finally a plateau. In order to explain this unexpected behaviour, we perform DOS calculations of a specific atom S close to the Mo vacancy, underlined by the black arrow in the inset in Fig.5.6. Before the contact, the three Sulfur atoms around the Mo-vacancy are equivalently decoupled from the Cu tip, showing one peak associated to the dangling bonds around the vacancy, as reflected in panel a). At 2.75 Å only one S atom remains unbonded to the Cu apex maintaining the peak at the Fermi Level, as shown in panel b). At the same time the other two S atoms, connected to the tip, present a broadened and slightly displaced DOS peak from the Fermi level. When the tip is approaching to 2.00 Å, the Cu-S bond is formed (see panel c)) and the peak is reduced. From this point, the apex is contacted to the three S atoms and additional bonds are formed with the Cu atoms of the second layer, yielding the plateau of conductance synonymous of the formation of a stable contact. Hence, the decrease of the conductance between 2.00 and 2.75 Å is justified by the DOS evolution.

On the other hand, the S-vacancy presents two clearly differentiated regimes: the tunneling and the contact regime. A characteristic plateau is formed after the Cu-S bonds formation at 2.00 Å. In this case, the Cu apex is bonded to the three neighboring Mo atoms at the same distance, leading to a more conventional curve. The value of the plateau is larger over the Mo vacancy due to the larger number of atoms contacted by the tip in this case (see the insets of Fig.5.5b and Fig.5.6).

The similarity between the two tips is related to the greater conductance characterizing the Mo vacancy, due to the better coupling of the tip-orbitals with the dangling bonds of the neighboring S atoms with respect to the neighboring Mo atoms in S vacancy.

5.3.3 Mo substitutional atoms

Finally, we will analyze the results on two substitutional cases, namely one Mo atom occupying a Sulfur vacancy and two Mo atoms on a S divacancy (labeled by subMo and subMo2, respectively). The results of forces and conductance are presented in Fig.5.7 for both graphene and Cu tips as previously done. In these two cases the minimum forces fall at the same distance for both tips, furthermore using graphene tip, the force curves are almost the same with minima around -0.25 nN. This is not the case of the Cu tip showing a larger interaction in the substitution of two Mo atoms on a S divacancy (-1.71 nN *vs* -1.46 nN). For both tips we found that comparing the forces curves they are larger than in the pristine layer, confirming the reactivity enhancement of the defective MoS₂, however lower than in the S and Mo vacancies.

Regarding the conductance curves, we can notice that the values are again much larger for the Cu tip (Fig.5.7c and Fig.5.7d for the graphene and Cu tips respectively). The typical behaviour associated with the vdW interaction is observed in conductance curve for graphene tip, characterized by tunneling regime with a saturation at short distances and

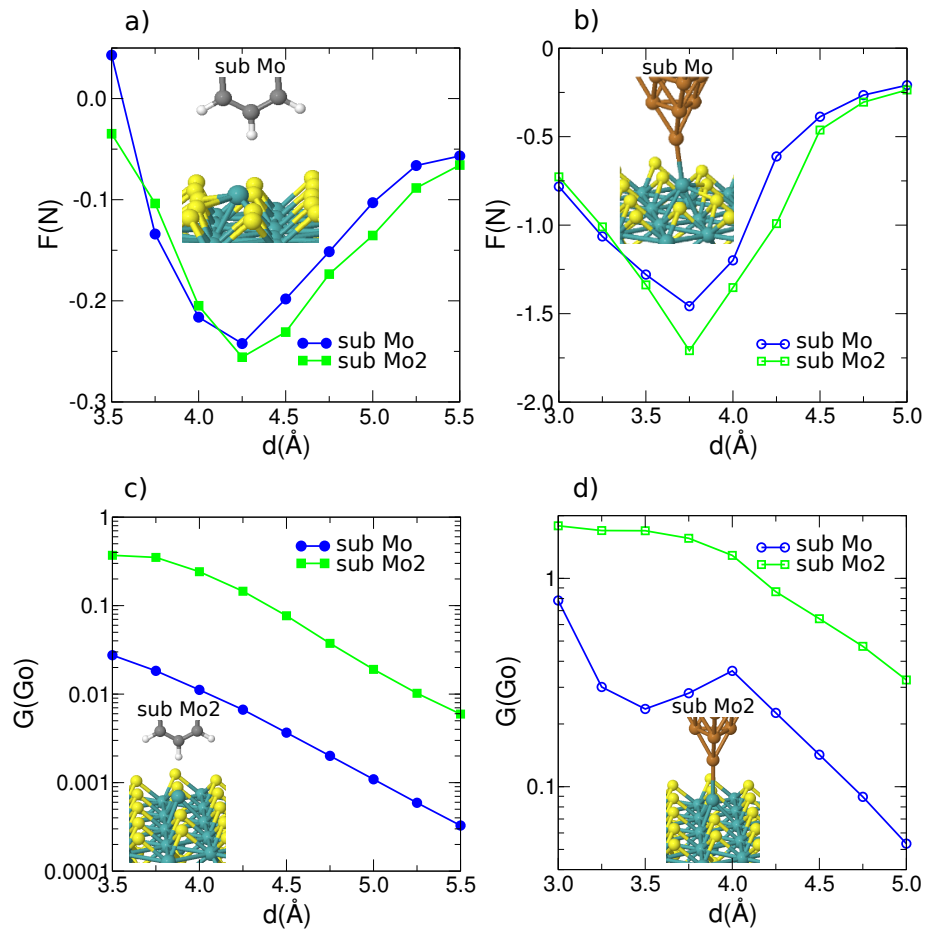


Figure 5.7: a) Force and c) conductance curves on one (two) substitutional Mo atom(s) in a S vacancy (divacancy) calculated with a graphene tip; b) and d) the same for a Cu tip. The conductance-axis is in logarithmic scale. In the insets the corresponding atomic structure of the minimum force on the four cases. The yellow/blue/brown/grey/white spheres represent the S/Mo/Cu/C/H atoms.

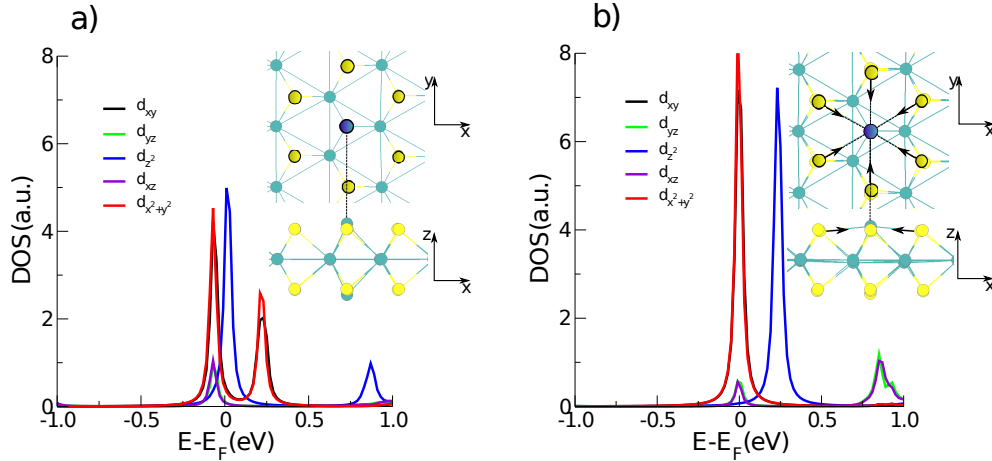


Figure 5.8: The electronic DOS for a) one upmost substitutional Mo atom in the S divacancy and b) the substitutional Mo atom in the single S vacancy. The atomic configuration of each defect is included in the insets.

no conductance plateau. However, the conductance associated with the two substitutional Mo atoms is much larger than in the case of a single substitution, suggesting a better coupling of the half-occupied p_y orbitals of the C2 atoms with the states associated to the substitutional atom.

In the case of the Cu tip, this effect is even stronger: the hybridization of the substitutional Mo atoms can explain the larger conductance. In the double substitution case, the Mo atoms present an important contribution of the d_{z^2} orbital at the Fermi level, as shown in Fig.5.8a, yielding, therefore, an important contribution in the conductance. In the single substitution case, the same contribution lies at 0.25 eV away from the Fermi level (see Fig.5.8b) and it is responsible for the significant reduction of the conductance. In the conductance related to the Cu tip, we find also two different behaviours related to the two substitutional configurations : in the double substitutional case we can recognize the standard tunneling regime and the jump to the contact followed by the conductance plateau, whereas in the substitutional case, there is a significant decrease in the conductance when the contact is formed. Then, the conductance increases again as the tip approaches more the sample. This peculiar conductance drop is associated to the specific configuration of the Mo substitutional atom : when the contact with the Cu tip is established, the extra Mo atoms which are rather weakly bounded to the neighboring atoms is attracted by the Cu tip and move out of the surface in order to form the bond with the Cu atom, as it can be seen from Fig.5.9a. The hybridization of this Mo atom with the Cu tip leads to a level splitting which diminishes the contribution at the Fermi level. The evolution of the Mo atom DOS and atomic structure for different distances is shown in Fig.5.9b. This peculiar behaviour results in a strong reduction of the conductance from 4.00 to 3.50 \AA . In fact, when the Cu tip approaches more to the layer, the Mo atom comes back to its original position in the MoS_2 : this causes the change of Mo hybridization and the relocation of the peak at the Fermi level, leading to an increase of the conductance. This specific substitu-

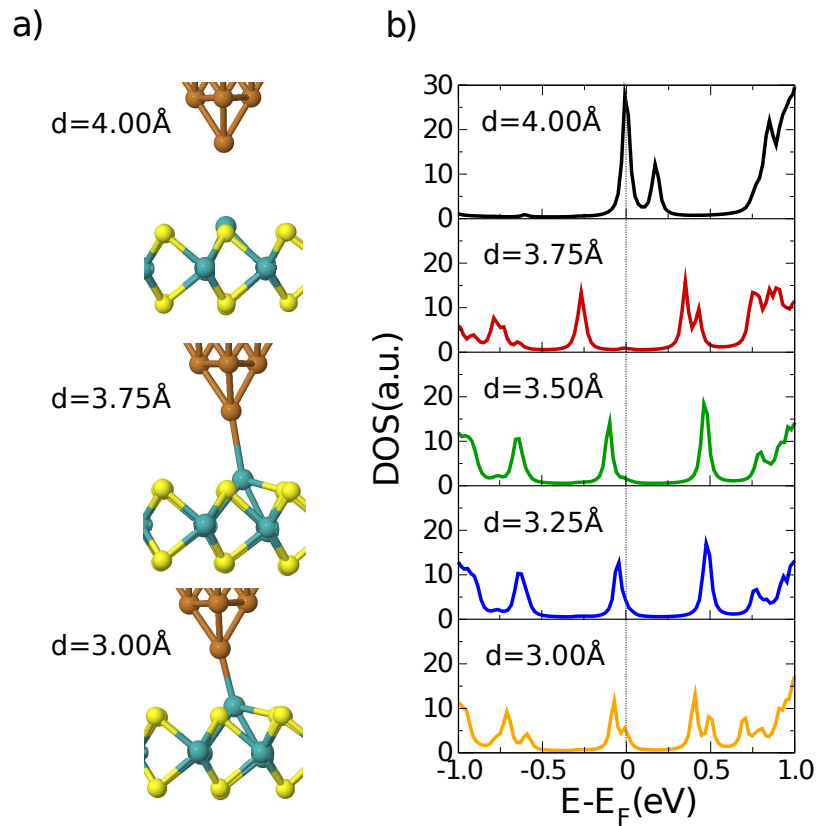


Figure 5.9: a) Atomic configuration for three distances, namely 4.00, 3.75 and 3.00 Å, b) evolution of the DOS of the upmost Mo substitutional atom in a S divacancy from 4.00 Å to 3.00 Å. The peak originally at the Fermi level for 4.00 Å is splitted at 3.75 Å before moving back to the Fermi level as the tip is approached at 3.25 Å and 3.00 Å.

tional case, due to this peculiar behaviour related to the sudden increase in the electronic injection can be interesting from the point of view of electronic devices.

As stressed earlier, both tips present a larger conductance over the defect including two extra Mo atoms, showing that a more efficient electronic injection can be established in the larger number of new accessible peaks around the Fermi level. On the contrary, in the substitutional cases, both tips present a lower attraction than with the neighboring S atoms of the Mo vacancy.

5.4 Summary

In this chapter, we have reported the characterization of MoS₂ defects (S or Mo vacancy, Mo mono- or di-substitutional in S vacancies) by using two tips, namely the standard Cu tip and graphene tip. First of all, it was demonstrated that the atomic resolution is obtained for graphene tip in STM simulations. The calculated STM images represent a useful guide

in the measurements, as an efficient theoretical technique to assist the experimental groups in the determination of defects in the sample.

Then, by comparing the conductance and force curves for different sites on pristine and defected MoS_2 , it is possible to explore the reactivity of the different defects: it results that Mo vacancy presents a higher attraction while the two Mo substitutionals on a S divacancy give a larger conductance for both tips. The main differences in conductance curves between the two tips is the presence of characteristic plateau linked to the bond formation between Cu tip and the sample, completely missed with graphene tip, where the conductance increases monotonically as consequence of the absence of bonds. The vdW interaction between the graphene tip and the sample is at the basis of conductance and force behaviour. Because of the vdW interaction, graphene tip is much less reactive than a standard metallic one, even for very reactive defects in MoS_2 . A fully non invasive characterization of defects is possible since there is no bond and no atomic transfer between tip and sample. On the other hand, the Cu tip leads to strong bonding with the defects, following a metal-semiconductor junction behaviour, which might even lead to atomic exchange, altering the correct characterization of the defects. From this point of view, the use of graphene tip for nc-AFM is of high interest for material spectroscopy. For future experiments, an instrument as a conductive AFM that can measure simultaneously the conductance and the short-range force is highly desirable. A graphene-like ribbon can be included in order to obtain atomic resolution. This kind of microscope can be used to measure a standard STM or nc-AFM image where the defects are found and then, by placing the tip over the selected points, a tip-approach can be done to obtain a conductance curve for each site. The conductance or electronic current can be directly compared to the theoretical curves presented in the previous figures.

We can conclude by stressing that, in this chapter, another interesting application of a system characterized by vdW forces, as the tip-sample system, was explored. Furthermore, the detailed study of specific defects in MoS_2 and the deep understanding of their characteristics, is extremely useful for further transport investigation at the graphene/ MoS_2 interface, where the defects are exploited instead of avoided.

Acknowledgements

Firstly, I would like to express my gratitude to my advisor Prof. Yannick Dappe for the continuous support of my Ph.D study, for his patience, motivation and knowledge. Besides my advisor, I would like to thank the rest of my thesis group, in particular Cyrille Barreteau, Alexander Smogunov, Genevieve Fleury and Sylvain Latil. Thanks also to Mathieu Cesar for coffee and discussions!

I would like to thank my committee members, Dr. Andrew Mayne, Prof. Philippe Sonnet, Dr. Evelyne Martin, Dr. Céline Fiorini and Dr. Pascal Pochet, for the time spent to read my Ph.D work, for letting my defense be an enjoyable moment, and for the brilliant comments and suggestions.

A very special thanks to César González Pascual for his help and support, the best *compagno di ufficio* ever, even at long distance!

Thanks to all the Lab, and to the very good friends I could find here.

Thanks to CEA phare program for funding my research.

Bibliography

- [1] K. S. Novoselov *et al.*, “Electric Field Effect in Atomically Thin Carbon Films”, *Science*, 306, 666, 2004.
- [2] P. R. Wallace *et al.*, “The Band Theory of Graphite”, *Phys. Rev.*, 71, 622, 1947.
- [3] J. W. McClure *et al.*, “Band Structure of Graphite and de Haas-van Alphen Effect”, *Phys. Rev.*, 108, 612, 1957.
- [4] G. W. Semenoff *et al.*, “Condensed-Matter Simulation of a Three-Dimensional Anomaly”, *Phys. Rev. Lett.*, 53, 2449, 1984.
- [5] K. I. Bolotin *et al.*, “Ultrahigh electron mobility in suspended graphene”, *Solid State Comm.* 146, 9-10, 351-434, (2008).
- [6] T. Uchihashi, “Two-dimensional superconductors with atomic-scale thickness,” *Superconductor Science and Technology*, 30, 1, 013002, 2017.
- [7] K. F. Mak *et al.*, “Atomically Thin MoS₂: A New Direct-Gap Semiconductor,” *Phys. Rev. Lett.* 105, 136805, 2010.
- [8] A. K. Geim and I. V. Grigorieva, “Van der Waals heterostructures”, *Nature*, 499, 419, 2013.
- [9] G. Wang *et al.*, “Direct Growth of Graphene Film on Germanium Substrate”, *Sci. Rep.*, 3, 2465. 2013.
- [10] L. H. Zeng *et al.*, “Monolayer Graphene/Germanium Schottky Junction As High-Performance Self-Driven Infrared Light Photodetector”, *ACS Appl. Mater. Interfaces*, 5, 9362-9366, 2013.
- [11] F. Cavallo *et al.*, “Exceptional Charge Transport Properties of Graphene on Germanium”, *ACS Nano*, 8 (10), 10237-10245, 2014.
- [12] C. R. Dean *et al.*, “Boron nitride substrates for high-quality graphene electronics”, *Nature Nanotech.*, 5, 722-726, 2010.
- [13] J. Xue *et al.*, “Scanning tunnelling microscopy and spectroscopy of ultra-flat graphene on hexagonal boron nitride”, *Nature Mater.*, 10, 282-285, 2011.

-
- [14] L. Britnell *et al.*, “Strong light-matter interactions in heterostructures of atomically thin films”, *Science*, 340, 6138, 1311-1314, 2013.
- [15] D. Di Felice *et al.*, “”, *Angle dependence of the local electronic properties of the graphene/MoS₂ interface determined by ab initio calculations J. Phys. D: Appl. Phys.* 50 17LT02, 2017.
- [16] Y. Ma *et al.*, “Graphene adhesion on MoS₂ monolayer: An ab initio study”, *Nanoscale*, 3, 3883-3887, 2011.
- [17] A. Ebnonnasir *et al.*, “Tunable MoS₂ bandgap in MoS₂-graphene heterostructures”, *Appl. Phys. Lett.*, 105, 031603, 2014.
- [18] Schwierz F. *et al.*, “Two-dimensional materials and their prospects in transistor electronics”, *Nanoscale*, 7, 8261, 2015
- [19] Moore G. E., “Cramming more components onto integrated circuits”, *Electronics*, 38, 114-177, 1965.
- [20] Dennard R. H. *et al.*, “Design of ion-implanted MOSFET’s with very small physical dimensions”, *IEEE J. Solid-State Circ.*, 9, 256-268, 1974.
- [21] K. Mistry *et al.*, “A 45nm Logic Technology with High-k+Metal Gate Transistors, Strained Silicon, 9 Cu Interconnect Layers, 193nm Dry Patterning, and 100% Pb-free Packaging”, *IEEE Int. Electron Devices Meet.* 247-250, 2007.
- [22] J. Cartwright, “Two-dimensional semiconductors for transistors”, *Nature*, 38, 114-177, 2011.
- [23] Ferrain I. *et al.*, “Multigate transistors as the future of classical metal-oxide-semiconductor field-effect transistors”, *Nature*, 479, 310-316, 2011.
- [24] Colinge J. P., “Multiple-gate SOI MOSFETs”, *Solid State Electron*, 48, 6, 897-905, 2004.
- [25] Radisavljevic B. *et al.*, “Single-layer MoS₂ transistors”, *Nature Nanotech.*, 6, 147, 2011.
- [26] Youngki Yoon *et al.*, “How Good Can Monolayer MoS₂ Transistors Be?”, *Nano Lett.*, 11(9), 3768-3773, 2011.
- [27] N. Myoung *et al.*, “Large Current Modulation and Spin-Dependent Tunneling of Vertical Graphene/MoS₂ Heterostructures”, *ACS Nano*, 7(8), 7021-7027, 2013.
- [28] L. Britnell *et al.*, “Field-effect tunneling transistor based on vertical graphene heterostructures.”, *Science*, 335, 947, 2012.

- [29] W. Yu *et al.*, “Vertically Stacked Multi-Heterostructures of Layered Materials for Logic Transistors and Complementary Inverters”, *Nature Mater.*, 12, 246-252, 2013.
- [30] A. K. Singh *et al.*, “Low-Voltage and High-Performance Multilayer MoS₂ Field-Effect Transistors with Graphene Electrodes”, *ACS Appl. Mater. Interfaces*, 8, 34699-34705, 2016.
- [31] T. Roy *et al.*, “Field-Effect Transistors Built from All Two-Dimensional Material Components”, *ACS Nano*, 8, 6, 6259-6264, 2014.
- [32] S. Bertolazzi *et al.*, “Nonvolatile Memory Cells Based on MoS₂/Graphene Heterostructures”, *ACS Nano*, 7, 3246-3252, 2013.
- [33] Britnell, L. *et al.*, “Strong Light-Matter Interactions in Heterostructures of Atomically Thin Films”, *Science*, 340, 1311-1314, 2013.
- [34] Georgiou, T. *et al.*, “Vertical Field-Effect Transistor Based on Graphene-WS₂ Heterostructures for Flexible and Transparent Electronics”, *Nature Nanotech.*, 8, 100-103, 2013.
- [35] G. Lee *et al.*, “Heterostructures Based on Inorganic and Organic van der Waals Systems”, *APL Mater.*, 2, 092511, 2014.
- [36] X. Wang, F. N. Xia, “Stacked 2D Materials Shed Light”, *Nature Mater.*, 14, 264-265, 2015.
- [37] F. Withers *et al.*, “Light-Emitting Diodes by Band-Structure Engineering in van der Waals Heterostructures”, *Nature Mater.*, 14, 301-306, 2015.
- [38] M. S. Choi *et al.*, “Controlled Charge Trapping by Molybdenum Disulphide and Graphene in Ultrathin Heterostructured Memory Devices”, *Nature Commun.*, 4, 1624, 2013.
- [39] K. Zhou *et al.*, “Raman Modes of MoS₂ used as fingerprint of vander Waals interactions”, *ACS*, 8, 9914-9924, 2014.
- [40] H. Fang *et al.*, “Strong Interlayer Coupling in van der Waals Heterostructures Built from Single-Layer Chalcogenides”, *Proc. Natl. Acad. Sci. U. S. A.*, 111, 6198-6202, 2014.
- [41] K. H Liu *et al.*, “Evolution of Interlayer Coupling in Twisted Molybdenum Disulfide Bilayers”, *Nature Commun.*, 5, 4966, 2014.
- [42] C. H. Lee *et al.*, “Atomically Thin p-n Junctions with van der Waals Heterointerfaces”, *Nature Nanotech.* 9, 676-681, 2014.
- [43] P. Rivera *et al.*, “Observation of Long-Lived Interlayer Excitons in Monolayer MoSe₂-WSe₂ Heterostructures”, *Nature Commun.*, 6, 6242, 2015.

-
- [44] P. Hohenberg and W. Kohn, “Inhomogeneous electron gas”, *Phys. Rev.*, 136, B864–B871, 1964.
- [45] R. M. Martin, “Electronic structure: basic theory and practical methods”, *Cambridge University Press*, 2004.
- [46] W. Kohn and L. J. Sham, “Self-consistent equations including exchange and correlation effects” *Phys. Rev.*, 140, A1133–A1138, 1965.
- [47] J. P. Perdew and A. Zunger, “Self-interaction correction to density-functional approximations for many-electron systems,” *Phys. Rev. B*, 23, 5048–5079, 1981.
- [48] J. P. Perdew *et al.*, “Generalized gradient approximation made simple”, *Phys. Rev. Lett.*, 77, 3865–3868, 1996.
- [49] N. Troullier and J. L. Martins, “Efficient pseudopotentials for plane-wave calculations”, *Phys. Rev. B* 43, 1993, 1991.
- [50] D. R. Hamann, “Generalized norm-conserving pseudopotentials”, *Phys. Rev. B* 40, 2980, 1989.
- [51] G. B. Bachelet *et al.*, “Pseudopotentials that work: From H to Pu”, *Phys. Rev. B* 26, 4199, 1982.
- [52] G. P. Kerker, “Non-singular atomic pseudopotentials for solid state applications”, *J. Phys. C*, 13, L189, 1980.
- [53] A. Zunger and M. L. Cohen, “First-principles nonlocal-pseudopotential approach in the density-functional formalism: Development and application to atoms”, *Phys. Rev. B*, 5449, 1978.
- [54] D. R. Hamann *et al.*, “Norm-Conserving Pseudopotentials”, *Phys. Rev. Lett.*, 43, 1494, 1979.
- [55] L. Kleinman and D. M. Bylander, “Efficacious Form for Model Pseudopotentials”, *Phys. Rev. Lett.* 48, 1425, 1982.
- [56] J. P. Lewis *et al.*, “Advances and applications in the Fireball ab initio tight-binding molecular-dynamics formalism”, *Phys. Status Solidi B*, vol 248, 9, 2011.
- [57] J. Harris, “Simplified method for calculating the energy of weakly interacting fragments”, *Phys. Rev. B*, 31, 1770-1779, 1985.
- [58] W. Matthew *et al.*, “Tight-binding models and density-functional theory”, *Phys. Rev. B* 39, 12520-12536, 1989.
- [59] A. A. Demkov *et al.*, “Electronic structure approach for complex silicas”, *Phys. Rev. B*, 52(3), 1618–1630, 1995.

- [60] P. Löwdin, “On the Non-Orthogonality Problem Connected with the Use of Atomic Wave Functions in the Theory of Molecules and Crystals”, *J. Chem. Phys.*, 18, 365, 1950.
- [61] O. F. Sankey *et al.*, “*Ab initio* multicenter tight-binding model for molecular-dynamics simulations and other applications in covalent systems”, *Phys. Rev. B*, 40, p. 3979, 1989.
- [62] E. Abad *et al.*, “Barrier formation and charging energy for a variable nanogap organic molecular junction: a tip/C₆₀/Au(111) configuration”, *J. Phys.: Condens. Matt.*, 22, 304007, 2010.
- [63] E. Abad *et al.*, “Energy Level Alignment and Electron Transport Through Metal/Organic Contacts”, *Heidelberg: Springer-Verlag*, 2013.
- [64] Y. J. Dappe *et al.*, “Weak chemical interaction and van der Waals forces between graphene layers: A combined density functional and intermolecular perturbation theory approach”, *Phys. Rev. B*, 74, p. 205434, 2006.
- [65] E. C. Goldberg *et al.*, “Molecular orbital theory for chemisorption and physisorption: The case of He on metals” *Phys. Rev. B*, 39, 5684, 1989.
- [66] F. J. García-Vidal *et al.*, “Molecular-orbital theory for chemisorption: The case of H on normal metals” *Phys. Rev. B*, 44, 11412, 1991.
- [67] J. Ortega *et al.*, “Simplified electronic-structure model for hydrogen-bonded systems: Water” *Phys. Rev. B*, 50, 10516, 1994; *J. Chem. Phys.*, 106, p. 3696, 1997.
- [68] L. V. Keldysh, “Diagram technique for nonequilibrium process”, *Eskp, Teor. Phys.*, 47, 1515, 1964 [*Sov. Phys. JEPT.*, 1018, 1965.]
- [69] C. Caroli, *et al.*, “Direct calculation of the tunneling current”, *J. Phys. C: Solid State Phys.*, 4, 916, 1971.
- [70] N. D. Lang, “Resistance of a one-atom contact in the scanning tunneling microscope”, *Phys. Rev. B*, 36, 8173, 1987, J. Ferrer, A.Martin-Rodero and F. Flores “Contact resistance in the scanning tunneling microscope at very small distances”, *ibid.* 38, 10113, 1998.
- [71] E. N. Economou., “Green’s Functions in Quantum Physics”, *Springer-Verlag*, 1990.
- [72] G. Binnig *et al.*, “Tunneling through a controllable vacuum gap”, *Appl. Phys. Lett.*, 40, 178–180, 1982.
- [73] G. Binnig *et al.*, “7×7 reconstruction on Si(111) resolved in real space”, *Phys. Rev. Lett.*, 50, 120–123, 1983.

- [74] W. A. Harrison, “Electronic Structure and the Properties of Solids: The Physics of the Chemical Bond”. *Dover Publications*, 1989.
- [75] <https://www.quora.com/What-is-the-formula-for-carbon-graphite>
- [76] A. K. Geim and K. S. Novoselov, “The rise of graphene”, *Nature Mater.*, 6, 183–191, 2007.
- [77] A. H. Castro Neto *et al.*, “The electronic properties of graphene”, *Rev. Mod. Phys.*, 81, 109–162, 2009.
- [78] A. K. Geim, “Graphene: Status and prospects”, *Science*, 324, 5934, 1530–1534, 2009.
- [79] D. Reddy *et al.*, “Graphene field-effect transistors”, *J. Phys. D: Appl. Phys.*, 45, 019501, 2012.
- [80] Gwan-Hyoung Lee *et al.*, “Flexible and Transparent MoS₂ Field-Effect Transistors on Hexagonal Boron Nitride-Graphene Heterostructures”, *ACS Nano*, 7 (9), pp 7931–7936, 2013
- [81] X. Li and H. Zhu , “Two-dimensional MoS₂: Properties, preparation, and applications”, *Journal of Materiomics*, 1, 33-44, 2015.
- [82] <https://graphene-supermarket.com/Extra-Large-MOS2-Crystal.html>
- [83] A. Molina-Sánchez and L. Wirtz, “Phonons in single and few-layer MoS₂ and WS₂”, *Phys. Rev. B* 84, 155413, 2011.
- [84] M. Tsai *et al.*, “Monolayer MoS₂ Heterojunction Solar Cells” *ACS Nano*, 8 (8), 8317-8322, 2014.
- [85] Akhilesh Kumar Mishra *et al.*, “Graphene and Beyond Graphene MoS₂: A New Window in Surface-Plasmon-Resonance-Based Fiber Optic Sensing”, *J. Phys. Chem. C*, 120 (5), 2893-2900, 2016.
- [86] Z. B. Aziza *et al.*, “Bandgap inhomogeneity of MoS₂ monolayer on epitaxial graphene bilayer in van der Waals p-n junction”, *Carbon*, 110, 396-403, 2016
- [87] H. C. Diaz *et al.*, “Direct Observation of Interlayer Hybridization and Dirac Relativistic Carriers in Graphene/MoS₂ van der Waals Heterostructures”, *Nano Lett.* 15, 1135-1140, 2015.
- [88] W. Jin *et al.*, “Tuning the electronic structure of monolayer graphene/MoS₂ van der Waals heterostructures via interlayer twist”, *Phys. Rev. B*, 92, 201409(R), 2015.
- [89] Z. Wang *et al.*, “Electronic Structure of Twisted Bilayers of Graphene/MoS₂ and MoS₂/MoS₂”, *J. Phys. Chem. C*, 119, 9, 4752-4758, 2015.

- [90] J. M. B. Lopes dos Santos *et al.*, “Graphene Bilayer with a Twist: Electronic Structure”, *Phys. Rev. Lett.*, 99, 256802, 2007.
- [91] D. Pierucci *et al.*, “Band Alignment and Minigaps in Monolayer MoS₂-Graphene van der Waals Heterostructures”, *Nano Lett.*, 16, 4054, 2016.
- [92] C. Zhang *et al.*, “Direct Imaging of Band Profile in Single Layer MoS₂ on Graphite: Quasiparticle Energy Gap, Metallic Edge States, and Edge Band Bending”, *Nano Lett.*, 14, p. 2443, 2014.
- [93] Z. Liu *et al.*, “Strain and structure heterogeneity in MoS₂ atomic layers grown by chemical vapour deposition”, *Nature Commun.*, 5, 5246, 2014.
- [94] L. Yang *et al.*, “Lattice strain effects on the optical properties of MoS₂ nanosheets”, *Sci. Rep.*, 4, 5649, 2014.
- [95] M. T. Dau *et al.*, “Beyond van der Waals Interaction: The Case of MoSe₂ Epitaxially Grown on Few-Layer Graphene”, *ACS Nano*, 12, 2319-2331, 2018.
- [96] M. T. Dau *et al.*, “Millimeter-Scale Layered MoSe₂ Grown on Sapphire and Evidence for Negative Magnetoresistance”, *Appl. Phys. Lett.*, vol 110, 011909, 2017.
- [97] B. Hunt *et al.*, “Massive Dirac Fermions and Hofstadter Butterfly in a van der Waals Heterostructure” *Science*, 340, 1427-1430, 2013.
- [98] Yankowitz M. *et al.*, “Emergence of Superlattice Dirac Points in Graphene on Hexagonal Boron Nitride”, *Nature Phys.*, 8, 382, 2012.
- [99] T. Ohta *et al.*, “Controlling the Electronic Structure of Bilayer Graphene”, *Science*, 313, 951-954, 2006.
- [100] D. Pierucci D. *et al.*, “Self-Organized Metal-Semiconductor Epitaxial Graphene Layer on Off-Axis 4H-SiC(0001)”, *Nano Res.*, 8, 1026-1037, 2015.
- [101] M. Sprinkle *et al.*, “First Direct Observation of a Nearly Ideal Graphene Band Structure”, *Phys. Rev. Lett.*, 103, 226803, 2009.
- [102] S. Y. Zhou *et al.*, “Substrate-Induced Bandgap Opening in Epitaxial Graphene”, *Nature Mater.*, 6, 770, 2007.
- [103] J. Bardeen and W. H. Brattain, “The Transistor, A Semi-Conductor Triode”, *Phys. Rev.* 74, 230, 1948.
- [104] <https://www.extremetech.com/extreme/175004-the-genesis-of-the-transistor-the-single-greatest-discovery-in-the-last-100-years>
- [105] M. C. Lemme *et al.*, “A graphene field-effect device”, *IEEE Electron Device Lett.*, 28, 4, 282-284, 2007.

- [106] X. Li *et al.*, “Chemically derived, ultrasmooth graphene nanoribbon semiconductors”, *Science*, 319, 1229-1232, 2008.
- [107] M. Y. Han *et al.*, “Energy band-gap engineering of graphene nanoribbons”, *Phys. Rev. Lett.*, 98, 206805, 2007.
- [108] P. Kim *et al.*, “Graphene nanoribbon devices and quantum heterojunction devices”, *Tech. Dig. Int. Electron Devices Meeting*, 241-244, 2009.
- [109] E. V. Castro *et al.*, “Biased bilayer graphene: Semiconductor with a gap tunable by the electric field effect”, *Phys. Rev. Lett.*, 99, 216802, 2007.
- [110] P. Gava *et al.*, “*Ab initio* study of gap opening and screening effects in gated bilayer graphene”, *Phys. Rev. B*, 79, 165431, 2009.
- [111] T. Roy *et al.*, “Dual-gate $\text{MoS}_2/\text{WSe}_2$ van der Waals Tunnel Diodes and Transistors”, *ACS Nano*, 9, 2071-2079, 2015.
- [112] A. Nourbakhsh *et al.*, “Transport properties of a $\text{MoS}_2/\text{WSe}_2$ heterojunction transistor and its potential for application”, *Nano Lett.*, 16, 1359-1366, 2016.
- [113] D. Sarkar *et al.*, “A subtermionic tunnel field-effect transistor with an atomically thin channel”, *Nature*, 526, 91-95, 2015.
- [114] D. Di Felice and Y. J. Dappe, “2D vertical field effect transistor”, *Nanotechnology*, accepted Manuscript online 25 September 2018, DOI: <https://doi.org/10.1088/1361-6528/aae406>.
- [115] S. Luryi, “Quantum capacitance devices”, *Appl. Phys. Lett.*, 52, 201, 1988.
- [116] M. Heiblum *et al.*, “Ballistic hot-electron transistors”, *IBM J. Res. Develop.*, 34, 530, 1990.
- [117] J. A. Simmons *et al.*, “Planar quantum transistor based on 2D–2D tunneling in double quantum well heterostructures”, *J. Appl. Phys.*, 84, 5626, 1998.
- [118] A. Zaslavsky *et al.*, “Ultrathin silicon-on-insulator vertical tunneling transistor”, *Appl. Phys. Lett.*, 83, 1653, 2003.
- [119] A. Sciambi *et al.*, “Vertical field-effect transistor based on wave-function extension”, *Phys. Rev. B*, 84, 085301, 2011.
- [120] L. Liu *et al.*, “Defects in Graphene: Generation, Healing, and Their Effects on the Properties of Graphene: A Review”, *Journal of Materials Science & Technology*, 31, 599-606, 2015.
- [121] Z. Lin *et al.*, “Defect engineering of two-dimensional transition metal dichalcogenides”, *2D Mater.*, 3, 022002, 2016.

- [122] KC S *et al*, “Controlled exfoliation of molybdenum disulfide for developing thin film humidity sensor”, *Nanotechnology*, 25, 375703, 2014.
- [123] Liu X *et al*, “Point Defects and Grain Boundaries in Rotationally Commensurate MoS₂ on Epitaxial Graphene”, *J. Phys. Chem. C*, 120, 20798, 2016.
- [124] N. Kodama *et al*, “Electronic States of Sulfur Vacancies Formed on a MoS₂ Surface”, *Jpn. J. Appl. Phys.*, 49, 8S3, 2010
- [125] S. G. Sørensen *et al*, “Structure and Electronic Properties of *In Situ* Synthesized Single-Layer MoS₂ on a Gold Surface”, *ACS Nano*, 8, 6788, 2014.
- [126] C-P Lu *et al*, “Bandgap, Mid-Gap States, and Gating Effects in MoS₂”, *Nano Lett.*, 14, 4628, 2014.
- [127] R. Addou *et al*, “Surface Defects on Natural MoS₂”, *Appl. Mat. Interf.*, 7, 11921, 2005.
- [128] P. Vancsó *et al*, “The intrinsic defect structure of exfoliated MoS₂ single layers revealed by Scanning Tunneling Microscopy”, *Sci. Rep.*, 6, 29726, 2016.
- [129] P. Bampoulis *et al.*, “Defect Dominated Charge Transport and Fermi Level Pinning in MoS₂/Metal Contacts”, *ACS Appl. Mater. Interfaces*, 9, 19278-19286, 2017.
- [130] D. Di Felice *et. al*, “Forces and electronic transport in a contact formed by a graphene tip and a defective MoS₂ monolayer: a theoretical study”, *Nanotechnology*, 29, 225704, 2018.
- [131] J-Y Noh *et al*, “Stability and electronic structures of native defects in single-layer MoS₂”, *Phys. Rev. B*, 89, 205417, 2014.
- [132] Zhou W *et al*, “Intrinsic Structural Defects in Monolayer Molybdenum Disulfide”, *Nano Lett.*, 13, 2615, 2013.
- [133] Hong J *et al* “Exploring atomic defects in molybdenum disulphide monolayers”, *Nature Commun.*, 6, 6293, 2015.
- [134] González C. *et al*, “Theoretical characterisation of point defects on a MoS₂ monolayer by scanning tunnelling microscopy”, *Nanotechnology*, 27, 105702, 2016.
- [135] González C. *et al*, “Reactivity Enhancement and Fingerprints of Point Defects on a MoS₂ Monolayer Assessed by *ab initio* Atomic Force Microscopy”, *J. Phys. Chem. C*, 120, 17115-17126, 2016.
- [136] Li H. *et al*, “Activating and optimizing MoS₂ basal planes for hydrogen evolution through the formation of strained sulphur vacancies”, *Nature Mater.*, 15, 48, 2016.

- [137] Makarova M. *et al*, “Selective Adsorption of Thiol Molecules at Sulfur Vacancies on MoS₂(0001), Followed by Vacancy Repair via S-C Dissociation”, *J. Phys. Chem. C*, 116, 22411, 2012.
- [138] Qi L. *et al*, “Chemisorption-induced *n*-doping of MoS₂ by oxygen”, *App. Phys. Lett.*, 108, 063103, 2016.
- [139] Akdim B. *et al*, “Theoretical analysis of the combined effects of sulfur vacancies and analyte adsorption on the electronic properties of singlelayer MoS₂”, *Nanotechnology*, 27, 185701, 2016.
- [140] Li H. *et al*, “Markedly different adsorption behaviors of gas molecules on defective monolayer MoS₂: a first-principles study”, *Phys. Chem. Chem. Phys.*, 18, 15110-15117, 2016.
- [141] M. P. K. Sahoo *et al*, “Modulation of Gas Adsorption and Magnetic Properties of Monolayer-MoS₂ by Antisite Defect and Strain”, *J. Phys. Chem. C*, 120, 14113-14121, 2016.
- [142] S-Y Cho *et al*, “Highly Enhanced Gas Adsorption Properties in Vertically Aligned MoS₂ Layers”, *ACS Nano*, 9, 9314-9321, 2015.
- [143] C. González *et al*, “Adsorption of small inorganic molecules on a defective MoS₂ monolayer”, *Phys. Chem. Chem. Phys*, 19, 9485-9499, 2017.
- [144] C. González and Y. J. Dappe , “Molecular Detection on a defective MoS₂ monolayer by simultaneous conductance/force simulations”, *Phys. Rev. B*, 95, 214105, 2017.
- [145] A. Castellanos-Gomez *et al*, “Carbon tips as electrodes for single-molecule junctions”, *Appl. Phys. Lett.*, 99, 123105, 2011.
- [146] A. Castellanos-Gomez *et al*, “Carbon fibre tips for scanning probe microscopy based on quartz tuning fork force sensors”, *Nanotechnology*, 21, 145702, 2010.
- [147] Y. J. Dappe *et al*, “Carbon tips for all-carbon single-molecule electronics”, *Nanoscale*, 6, 6953, 2014.
- [148] C. González *et al*, “Theoretical study of carbon-based tips for Scanning Tunnelling Microscopy”, *Nanotechnology*, 27, 105702, 2016.
- [149] J. Quereda *et al*, “Single-layer MoS₂ roughness and sliding friction quenching by interaction with atomically flat substrates”, *Appl. Phys. Lett.*, 105, 053111, 2014.
- [150] B. Liu *et al*, “High-Performance Chemical Sensing Using Schottky Contacted Chemical Vapor Deposition Grown Monolayer MoS₂ Transistors”, *ACS Nano*, 8, 5304, 2014.
- [151] X. Lu *et al*, “Layer-by-Layer Thinning of MoS₂ by Thermal Annealing”, *Nanoscale*, 5, 8904, 2013.

-
- [152] V. Kaushik *et al*, “Nanoscale Mapping of Layer-Dependent Surface Potential and Junction Properties of CVD-Grown MoS₂ Domains”, *Phys. Chem. C*, 119, 20136, 2015.
- [153] S. Barja *et al*, “Charge density wave order in 1D mirror twin boundaries of single-layer MoSe₂”, *Nature Phys.*, 12, 751-756, 2016.
- [154] S. H. Song *et al*, “Probing defect dynamics in monolayer MoS₂ via noise nanospectroscopy”, *Nature Commun.*, 8, 2121, 2017.
- [155] G. Kresse and J. Hafner, “Ab initio molecular dynamics for liquid metals”, *Phys. Rev. B*, 47, R558, 1993.
- [156] G. Kresse and J. J. Furthmüller, “Efficient iterative schemes for ab initio total-energy calculations using a plane-wave basis set”, *Phys. Rev. B*, 54, 11169, 1996.
- [157] G. Kresse and D. Joubert, “From ultrasoft pseudopotentials to the projector augmented-wave method”, *Phys. Rev. B*, 59, 1758, 1999.
- [158] J. P. Perdew *et al*, “Generalized Gradient Approximation Made Simple”, *Phys. Rev. Lett.*, 77, p. 3865, 1996.
- [159] P. E. Blöchl, “Projector augmented-wave method”, *Phys. Rev. B*, 50, 17953, 1994.
- [160] S. Grimme, “Semiempirical GGA-type density functional constructed with a long-range dispersion correction”, *J. Comput. Chem.*, 27, 1787-1799, 2006.
- [161] I. Horcas *et al*, *Rev. Sci. Instrum.*, 78, 013705, 2007; WSxM solutions website www.wsxmsolutions.com
- [162] A. Altibelli *et al*, “Interpretation of STM images: the MoS₂ surface”, *Surf. Sci.*, 367, 2, 209-220, 1996.

Titre : Structure électronique et transport dans l'hétérostructure graphène/MoS₂ pour la conception d'un transistor à effet de champ.

Mots clés : DFT, matériaux 2D, structure électronique, hétérostructure de Van der Waals, transistor, transport électronique.

Résumé : L'isolement du graphène, une monocouche de graphite composée d'un plan d'atomes de carbone, a démontré qu'il est possible de séparer un seul plan d'épaisseur atomique, que l'on appelle matériau bidimensionnel (2D), à partir des solides de Van der Waals (vdW). Grâce à leur stabilité, différents matériaux 2D peuvent être empilés pour former les hétérostructures de vdW. L'interaction vdW à l'interface étant suffisamment faible, les propriétés spécifiques de chaque matériau demeurent globalement inchangées dans l'empilement. En utilisant une démarche théorique et computationnelle basée sur la théorie de la fonctionnelle de la densité (DFT) et le formalisme de Keldysh-Green, nous avons étudié l'hétérostructure graphène/MoS₂. Le principal intérêt des propriétés spécifiques du graphène et du MoS₂ pour la conception d'un transistor à effet de champ réside dans la mobilité du graphène, à la base d'un transistor haute performance et dans le gap électronique du MoS₂, à la base de la commutation du dispositif. Tout d'abord, nous avons étudié les effets de la rotation entre les deux couches sur les propriétés électroniques à l'interface, en démontrant que les propriétés électroniques globales ne sont pas affectées par l'orientation. En revanche, les images STM (microscope à effet tunnel) sont différentes pour chaque orientation, en raison d'un changement de densité de charge locale. Dans un deuxième temps, nous avons utilisé l'interface graphène/MoS₂ en tant que modèle très simple de Transistor à Effet de Champ.

Nous avons analysé le rôle des hétérostructures de vdW sur la performance du transistor, en ajoutant des couches alternées de graphène et MoS₂ sur l'interface graphène/MoS₂. Il a ainsi été démontré que la forme de la DOS au bord du gap est le paramètre le plus important pour la vitesse de commutation du transistor, alors que si l'on ajoute des couches, il n'y aura pas d'amélioration du comportement du transistor, en raison de l'indépendance des interfaces dans les hétérostructures de vdW. Cependant, cela démontre que, dans le cadre de la DFT, on peut étudier les propriétés de transport des hétérostructures de vdW plus complexes en séparant chaque interface et en réduisant le temps de calcul. Les matériaux 2D sont également étudiés ici en tant que pointe pour STM et AFM (microscope à force atomique) : une pointe de graphène testée sur MoS₂ avec défauts a été comparée aux résultats correspondants pour une pointe en cuivre. La résolution atomique a été obtenue et grâce à l'interaction de vdW entre la pointe et l'échantillon, il est possible d'éviter les effets de contact responsables du transfert d'atomes entre la pointe et l'échantillon. En outre, l'analyse des défauts est très utile du fait de la présence de nouveaux pics dans le gap du MoS₂ : ils peuvent ainsi être utilisés pour récupérer un pic de courant et donner des perspectives pour améliorer la performance des transistors.

Title : Electronic structure and transport in the graphene/MoS₂ heterostructure for the conception of a field effect transistor.

Keywords : DFT, 2D materials, electronic structure, Van der Waals heterostructure, transistor, electronic transport.

Abstract : The isolation of graphene, a single stable layer of graphite, composed by a plane of carbon atoms, demonstrated the possibility to separate a single layer of atomic thickness, called bidimensional (2D) material, from the van der Waals (vdW) solids. Thanks to their stability, 2D materials can be used to form vdW heterostructures, a vertical stack of different 2D crystals maintained together by the vdW forces. In principle, due to the weakness of the vdW interaction, each layer keeps its own global electronic properties. Using a theoretical and computational approach based on the Density Functional Theory (DFT) and Keldish-Green formalism, we have studied graphene/MoS₂ heterostructure. In this work, we are interested in the specific electronic properties of graphene and MoS₂ for the conception of field effect transistor: the high mobility of graphene as a basis for high performance transistor and the gap of MoS₂ able to switch the device. First, the graphene/MoS₂ interface is electronically characterized by analyzing the effects of different orientations between the layers on the electronic properties. We demonstrated that the global electronic properties as bandstructure and Density of State (DOS) are not affected by the orientation, whereas, by mean of Scanning Tunneling Microscope (STM) images, we found that different orientations leads to different local DOS.

In the second part, graphene/MoS₂ is used as a very simple and efficient model for Field Effect Transistor. The role of the vdW heterostructure in the transistor operation is analyzed by stacking additional and alternate graphene and MoS₂ layers on the simple graphene/MoS₂ interface. We demonstrated that the shape of the DOS at the gap band edge is the fundamental parameter in the switch velocity of the transistor, whereas the additional layers do not improve the transistor behavior, because of the independence of the interfaces in the vdW heterostructures. However, this demonstrates the possibility to study, in the framework of DFT, the transport properties of more complex vdW heterostructures, separating the single interfaces and reducing drastically the calculation time. The 2D materials are also studied in the role of a tip for STM and Atomic Force Microscopy (AFM). A graphene-like tip, tested on defected MoS₂, is compared with a standard copper tip, and it is found to provide atomic resolution in STM images. In addition, due to vdW interaction with the sample, this tip avoids the contact effect responsible for the transfer of atoms between the tip and the sample. Furthermore, the analysis of defects can be very useful since they induce new peaks in the gap of MoS₂: hence, they can be used to get a peak of current representing an interesting perspective to improve the transistor operation.

